Evaluation of corrosion process and monitoring techniques of mooring chain steel in the marine environment

By

Jiawen Zhang

Thesis report

Student number: 5020557
Thesis committee: Prof.dr.ir. Arjan Mol
    Dr. Pooria Pahlavan
    Dr. Peyman Taheri
    Ir. Sarjoon Alkhateeb

TUDelft

Abstract

Currently, as the utilization of offshore wind energy continues to increase, floating wind turbines are expected to be widely used. As the fixed system of the turbine, the safety of the mooring chain has gradually attracted the attention of researchers. Mooring chains immersed in seawater are mainly subjected to various mechanical loads and corrosion. Therefore, premature failure and frequent replacement are the main problems of mooring chain systems. In order to avoid huge losses of safety caused by structural failure, it is urgent to establish mooring integrity management, accurately identify hazards, and evaluate the service life of the mooring system. Considering the requirements of sufficient mechanical properties and economic benefits, high-strength low-alloy steel has gradually replaced low-carbon steel as the main material for mooring chains. However, there are few studies on the detailed corrosion process of mooring chain steel.

This research aims to explore the corrosion process of mooring chain steel and the influence of marine environmental factors on the corrosion process. Traditional electrochemical techniques, morphology observation and new in-situ non-destructive technique acoustic emission are used to investigate the corrosion process. The experiment includes the exploration of the corrosion process of steel under natural and accelerated conditions. Experiments on the influence of flow velocity and temperature are also included. The corrosion process of mooring chain steel is successfully explored during the monitoring process. Acoustic emission signals related to corrosion are separated. Their sources are reasonably identified. The effects of water flow velocity and temperature of the corrosion process are summarized.

Contents

List of Figures

List of Tables

Abbreviations

MCS	Mooring chain steel
OCP	Open circuit potential
LPR	Linear polarization resistance
DOM	Digital optical microscope
AE	Acoustic emission
HSLA	High-strength low-alloy
AP	Anaerobic conditions point
DO	Dissolved oxygen
IGC	Intergranular corrosion
DC	Direct current
AC	Alternating current
PDP	Potentiodynamic polarization
EIS	Electrochemical impedance spectroscopy
HER	Hydrogen evolution reaction

1. Introduction

In recent decades, renewable energy has become more and more important to reduce greenhouse gas emissions while ensuring energy security. Among the various clean and renewable energy sources, wind energy has proven to be particularly attractive [1]. As two alternatives to wind energy, onshore and offshore production have rapidly developed in recent years. Compared with onshore wind, offshore wind has several characteristics that make it promising, such as stable resources, large area, convenient transportation, visual interference and low noise [2].

In many countries, offshore wind energy resources are located in places where sea depth exceeds 50 m [2]. Therefore, the cost attractiveness of bottom fixed wind turbines is reduced, and floating wind turbines are considered a better choice. Figure 1 shows three floating structures that have been used in floating wind turbines, namely semi-submersible, spar and tension leg platform (TLP) [1]. In these structures, the turbines are all connected to the seabed through a mooring chain system.
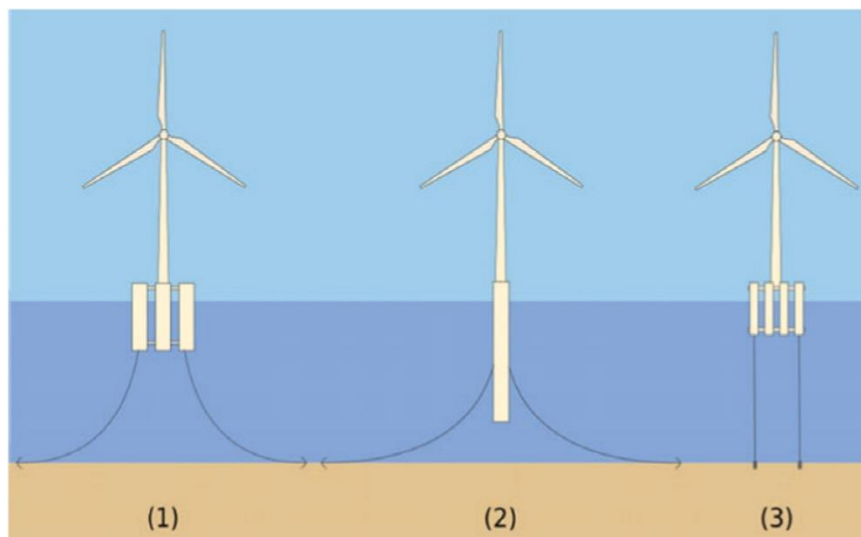
Figure 1 Floating wind turbine structures: (1) semi-submersible platform; (2) spar; and (3) tension leg platform (TLP) freely rendered from [1]

The application of the mooring system is to avoid the low-frequency movement of the floating structure caused by environmental force [3]. It consists of one or more wires anchored to the seabed, and these wires are connected to the floating platform at the fairlead. The load it receives will change in size and direction, mainly related to factors such as wind, waves, and ocean growth [4]. At the same time, because it is immersed in seawater, its structure will be severely affected by corrosion degradation [5]. Unlike the mooring rope failure of oil and gas platforms will lead to severe casualties or pollution, the failure of floating wind turbines can also cause substantial economic losses [2]. Considering both safety and the necessity of extending the service lifetime of mooring systems, research and developments have grown rapidly.

To avoid the premature occurrence of failures and excessive replacement of mooring lines [6], it is necessary to focus on mooring integrity management, including hazard identification, inspection and technology. Understanding the degradation process, using state of the art technologies to determine the safety factors, and developing new monitoring technologies are also significant to better ensure the safety status of the mooring system. Radiography, guided wave ultrasonic and other non-destructive detection techniques are used for existing regular inspections. However, these techniques are inconvenient for the application of continuous monitoring [7]. Acoustic emission technology is a potential structural health monitoring tool for continuous monitoring. It can be used in the offshore industry as a failure monitoring system. Many studies have proved that AE has application prospects in detecting the initiation and propagation of cracks and judging the corrosion process [8-10]. However, there is no systematic analysis method.

1.1 Aim of the thesis

The current work aims to identify key AE signal characteristics to monitor the corrosion process of mooring chain (MC) steel. In order to better achieve this goal, traditional electrochemical techniques have been introduced to characterize the corrosion process of MC steel. The corrosion process of samples is simulated in 3.5 wt.% solution in a laboratory environment. It is characterized by open circuit potential (OCP), linear polarization resistance (LPR), digital optical microscope (DOM) and AE. In addition, factors that may affect the corrosion process in the offshore environment have also been studied. Therefore, the current research issues are as follows:

- *What is the corrosion process of MC steel in the marine environment?*
- *Is there any key AE signal that can monitor the corrosion process of MC steel? What are the characteristics of these signals?*
- *What is the main environmental influence factor in the corrosion process of MC steel?*

1.2 Thesis outline

The thesis consists of seven chapters. In the first chapter, the background of the current work is briefly introduced. Chapter 2 reviews the basic concepts and previous research results related to the current research work. Chapter 3 describes the analytical methods used in the experiments. Chapter 4 presents the experimental setup and operation. Chapter 5 includes the results and discussion in the current work. Chapter 6 summarizes the content of the whole thesis. Finally, in Chapter 7, recommendations based on current work are provided.

1. Background and literature review

This chapter provides a detailed overview of the basic concepts and results in the literature related to the current work. It is divided into three parts. The first part introduces the material properties of MC steel. The second part explains the basic principles of the iron corrosion process in the marine environment, including uniform corrosion, pitting corrosion, as well as environmental factors that may affect the corrosion process. The third part describes the monitoring methods that can be used to detect the corrosion process, divided into two parts: electrochemical techniques and acoustic emission technique.

2.1 Mooring chain (MC) steel

The range and types of chains and fittings used in mooring applications are extensive. Based on the financial and application requirements, the steels used in these structures are divided into different strength levels. Different steel grades mainly depend on the changes in carbon content, element composition and heat treatment process [5]. Consequently, it has different mechanical properties, making them more suitable for applications in the marine environment.

Typically, there are standards covering chains and most related fittings used in mooring systems [11]. Five grades are defined according to the minimum ultimate tensile strength: R3, R3S, R4, R4S and R5. Among them, R3 is the lowest grade steel used in the chain [12]. It is widely used and is typically the focus of experimental research. The mechanical properties and alloy components for R3 grade are comparable to high strength low alloy steels (HSLA).

HSLA steel is a particular category of mild steel which contains microalloying elements [such as vanadium (V), niobium (Nb) or titanium (Ti)]. It also has excellent mechanical properties, such as high yield strength and ultimate tensile strength. In addition to good ductility, it also has great formability and weldability. The high strength of this type of steel stems from its microstructure factors, such as grain refinement, inclusion shape control and precipitation hardening [13]. In addition, due to the low concentration of alloying elements, the price of HSLA steel is not much different from that of mild steel [14].

Due to limitations in getting R3 steel, S420MC HSLA steel is chosen to represent this grade. Their mechanical performance parameters are listed in Table 1. In these representative performance parameters, it is roughly consistent with R3.

S420MC HSLA steel is typically based on a titanium micro alloyed C-Mn-Nb composition system. Figure 2 shows its metallographic microstructure. The white areas are the ferrite grains. The black areas are mainly grain boundaries. The average diameter of the grains is small, about 5 μm. The entire microstructure exhibits finer grains and larger areas of grain boundaries. Table 2 shows its chemical composition. This system achieves significant precipitation strengthening by making full use of the fine and dispersed TiC (Titanium carbide) particles [15]. With a small amount of niobium, the austenite recrystallization temperature of this kind of steel will be increased. Meanwhile, the austenite non-

recrystallization zone will become larger [16]. Therefore, it can be completely deformed with a fine microstructure in high-temperature processing. It is also conducive to the production of thin-gauge products. The function of adding vanadium is to affect the precipitation behavior of TiC. Therefore, the strength of steel can be further modified. Performance fluctuations will also become less as well [17].

Table 1 Minimum mechanical properties for chain cable materials and S420MC steel [12, 17]

Steel Grade	Yield Stress [MPa]	Tensile Strength [MPa]	Elongation [%]
R3	410	690	17
S420MC	420	480-620	16

Table 2 Chemical Composition of S420MC steel [17]

Element	Fe	C (max%)	Mn (max%)	P (max %)	S (max %)
content	balance	0.12	1.5	0.025	0.02
Element	Al tot (min %)	Nb (max %)	V (max %)	Si (max%)	Ti (max %)
content	0.015	0.09	0.20	0.5	0.15
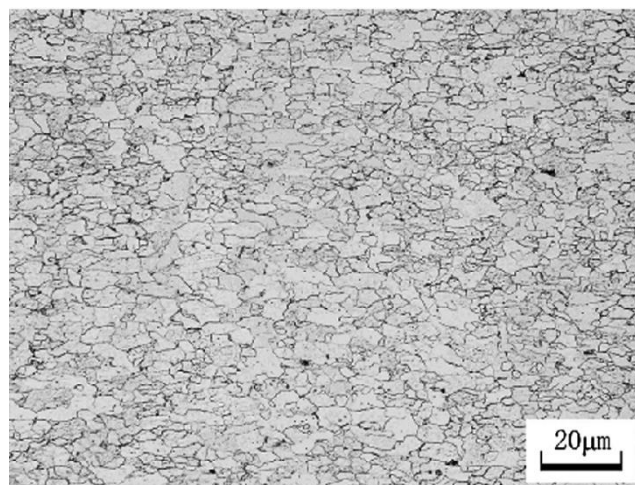
Figure 2 Metallographic microstructure of S420MC [17]

Due to the excellent mechanical properties, manufacturability and low cost, S420MC HSLA steel is often used as a structural steel in industrial products [17, 18]. However, the literature rarely focuses on the corrosion properties of this steel. Considering the existence of corrosive ions in the marine environment, the research on the corrosion process of S420MC HSLA steel is indispensable. Therefore, it becomes the research center of this subject.

2.2 Corrosion process of MC steel in the marine environment

2.2.1 Corrosion process of iron

Corrosion is a destructive attack caused by the reaction of metals with the environment. It is an electrochemical process, which usually occurs through the reaction of coupled electrochemical half-cell reactions. Among them, the half-cell reaction is divided into two parts. One is the anodic reaction, which is usually the loss of metal. The other is the cathodic reaction, determined by the environment [19].

Corrosion of iron in an aqueous solution generally requires four prerequisites: an anode that corrodes, a cathode that reduces oxygen or emits hydrogen, a conductive aqueous electrolyte composed of anions and cations, and a metal path through which electrons pass, as Figure 3 shows.
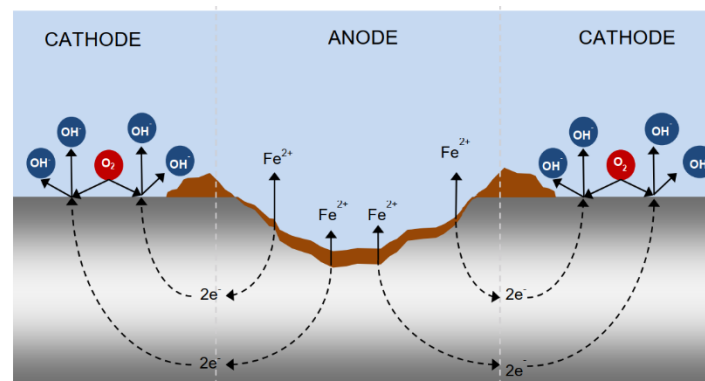
Figure 3 Schematic of the corrosion process and the presence of water is implied freely rendered from [20]

The reaction formula of steel dissolution is as follows

$$Fe \rightarrow Fe^{2+} + 2e^-$$
Equation 1

In order to keep the corrosion system in balance, the cathodic reaction will occur simultaneously to consume the electrons released by the anode reaction. Considering the seawater is usually neutral or weakly alkaline and has a certain amount of oxygen dissolved, the specific reaction of the cathode will be as follows [19]

$$O_2\ (g) + 2H_2O\ (l) + 4e^- \rightarrow 4OH^-$$
Equation 2
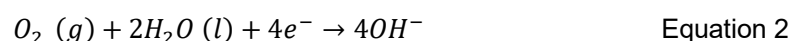
Combining Equation 1 with Equation 2 can complete the corrosion reaction equation in seawater environments

$$2Fe + O_2\ (g) + 2H_2O\ (l) \rightarrow 2Fe^{2+} + 4OH^-$$
Equation 3
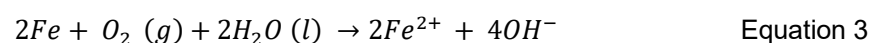
In most cases, the distance between the anodic and cathodic reactions can be negligible, and iron ions will combine with hydroxide ions to precipitate out of the solution. Through a series of reactions presented below, "rust" (such as Fe(OH)$_3$, Fe$_3$O$_4$) is formed [20]

$$Fe^{2+} + 2OH^- \rightarrow Fe(OH)_2 \qquad\qquad \text{Equation 4}$$

$$4Fe(OH)_2 + O_2 + H_2O \rightarrow 4Fe(OH)_3 \qquad\qquad \text{Equation 5}$$

$$4Fe(OH)_3 \rightarrow Fe_2O_3 \cdot H_2O + 2H_2O \qquad\qquad \text{Equation 6}$$
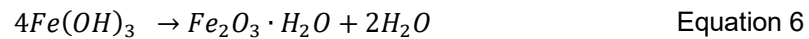
2.2.2 Corrosion process in the marine environment

Typically, there are two main types of corrosion: uniform corrosion and localized corrosion [21]. In the marine environment (the salinity of water ranges typically between 3.3 wt.% and 3.8 wt.% and temperatures vary per location between 5 °C and 25 °C), the localized corrosion mainly occurs in the form of pitting corrosion [22]. So, the most critical types of corrosion of MC steel are uniform corrosion and pitting corrosion, which will be introduced in detail in the following sections.

2.2.2.1 uniform corrosion

Uniform corrosion means the metal is more or less corroded over its entire surface. No part of the surface will be corroded more preferred than others. It will dissolve and become thinner until the sample finally fails [19].
Generally, the near-surface immersion corrosion model in seawater proposed by Melchers is used to describe the uniform corrosion of low-carbon steel and low-alloy steel under fully aerated marine immersion conditions, as shown in Figure 4 [3]. The curve consists of four phases, each controlled by a different corrosion mechanism. These are (i) kinetic control, (ii) oxygen diffusion control, (iii) control through the development of the anaerobic bacteria process, and (iv) control through the steady-state anaerobic bacteria process [22].
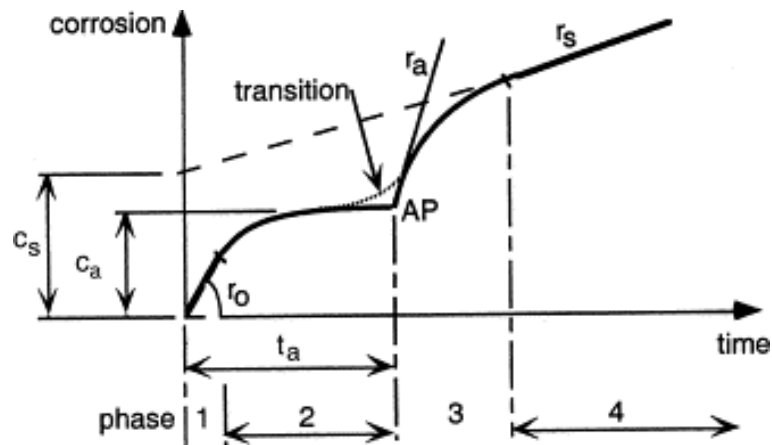
Figure 4 Mean-value corrosion loss as a function of exposure time for uniform corrosion freely rendered from [22]

Phase 1 is a linear relationship, which is controlled by the polarization of the cathode and anode. After a very short period, the local oxygen concentration at or near the corroded surface will decrease or even be depleted, so that the transmission of oxygen through the water to the surface of corrosive materials becomes the limiting standard [22]. During this period, the rust layer and marine growth will accumulate on the corroded surface, then the anaerobic conditions point (AP) is reached, which is the beginning of Phase 3. In Phase 3 and Phase 4, sulfate-reducing bacteria will grow rapidly first, then reach a steady state which is also an approximately linear stage.

In this model, temperature is the most important factor [22]. Temperature can affect the corrosion process by directly controlling the corrosion activity or affecting the dissolved oxygen content in the marine environment [23]. In Phase 1, an increase in temperature will lead to an increase in the energy of the system. Theoretically, each reaction has its corresponding activation energy under specific conditions, which is defined as an energy barrier that needs to be overcome for a chemical reaction to occur [24]. Higher system energy will cause it easier to cross the activation energy to initiate the reaction [22, 25]. Therefore, higher temperature will increase the corrosion rate. In the diffusion control stage, the increased temperature will accelerate the diffusion of oxygen in seawater. However, it will also reduce the solubility of oxygen. The combination of the two parts will still increase the corrosion rate, but the increase is not as obvious as in the first stage [26-28].

In addition to temperature, factors that may affect the corrosion behavior include oxygen supply, salinity, pH, water speed, wave action, marine growth and bacteria, surface conditions, and steel type [22, 29]. The specific influence of each factor is discussed below. Dissolved oxygen (DO) in seawater is the basis of reduction reactions (Equation 2). Generally, dissolved oxygen is linearly related to corrosion rate [22]. However, the rate of oxygen transport to the corroded surface is limited by the water circulation in static water. If the water circulation is low enough, the corrosion rate may be reduced. However, the actual marine environment is an open system, usually considered to be fully aerated waters. The DO in seawater can be replenished in time. It is generally considered to be constant. Therefore, DO is unlikely to be the main influencing factor in the off-shore marine environment [22, 29].

The influence of salinity has the same tendency with temperature. The salinity accelerates the corrosion process by increasing the conductivity of the seawater just in lower salt content (less than 3% wt). When the salinity exceeds the threshold (3% wt), the corrosion rate will decrease caused by the reduction of the oxygen concentration in seawater [30]. The salinity of the world's oceans varies almost between 3.3-3.8% wt, and the average value is about 3.5 wt.% [29]. Therefore, in an open ocean environment, the corrosion rate is inversely proportional to the salinity. In an offshore environment, the influence of human industry is not considered, thus the composition of seawater does not fluctuate much. Many studies reveal that salinity has less practical significance for marine corrosion [22].

The pH value of seawater acts as an essential part in the corrosion process, including the formation and dissolution of rusts, the evolution of the charge transfer process, and the initiation and growth of corrosion defects [29]. However, due to the large number of buffering factor pairs in seawater, its excellent buffering capacity will maintain the pH between 8.1 and 8.3 [31]. CO_2 and CO_3^{2-} are one of the most common buffer pairs in seawater. When the environment becomes acidic, CO_3^{2-} in seawater will react with H^+ to form CO_2, thereby reducing H^+ in the environment and increasing pH value. In contrast, when the OH^- ions increase, seawater will absorb CO_2, which can react with OH^- ions to produce CO_3^{2-}, thereby reducing the alkalinity of the environment. Although the daily pH value varies slightly between this range, it has little direct effect on the deposition and corrosion of calcium scale [22].

Water speed and waves are also important factors for ocean corrosion. For carbon steel, an increase in water velocity results in a higher corrosion rate until a certain critical velocity is reached [32]. Flowing water can contribute to more oxygen reaching the metal surface, and can also damage rusts to speed up the corrosion process [29].

The long-term effects of biological and marine growth on corrosion are complex. Factors such as species of organisms, nutrients (through pollutants), DO, and pH values can all contribute to the observed gaps in marine growth and therefore differences in corrosion [29].

The influence of the type of steel on the corrosion process is more complex. Composition, microstructure, structure, and stress distribution may all lead to different corrosion processes [29]. Therefore, there is still a lot of uncertainty in the estimation of the results of the immersion corrosion experiment of a specific steel under certain conditions.

2.2.2.2 Pitting corrosion

Pitting corrosion is a form of localized corrosion where corrosion is limited to smaller degraded areas [21]. Many studies show that pitting corrosion is one of the most critical forms of corrosion that exist in the marine and offshore structures [33, 34].

The structures in the marine environment are usually made of mild steel and alloy steel. These types of steels are more likely to be affected by pitting corrosion. The part on the surface that is more soluble and dissolves more quickly is more likely to be an inducing point for pitting corrosion. More specifically, the dissolution will result in the formation of cavities in the matrix. These cavities may penetrate through the wall thickness, resulting in insufficient sealing of material, or becoming the initiation point of stress corrosion cracking.

They may also lead to the brittleness of the component fracture [33]. This type of failure will be catastrophic and will lead to a damage of component sealing or its structural integrity. Pitting corrosion can be divided into four stages: passive film breakdown, pit initiation, metastable pitting, pit growth and pit stifling [25].

In passive film breakdown stage, the passivation film will rupture because of absorbing aggressive ions [34]. For the steel in its original state, the passive film will naturally form in the presence of oxygen.

Generally, the duration of the initial stage of pitting corrosion is very short, and the pit initiation mostly depends on the surface condition of the steel. Possible factors for pits occurrence are [33]

- Local integrity loss of the protective oxide layer (chemical or mechanical)
- Local environmental factors and variations that cause damage to the protective layer: acidity, high chlorine concentration
- Damaged or discontinuous protective coating
- Heterogeneous material microstructure (such as non-metallic inclusions, grain boundary).

For HSLA steel exposed to the marine environment, high chlorine concentration will be the main factor that causes pitting corrosion [34-40]. Chloride is an aggressive ion. It can form hydrochloric acid with the hydrogen ions in the solution, which is a strong acid. . Many metal cations have considerable solubility in its solutions. At the same time, the diffusion of chloride ions through the cracks and film is higher, which leads to the formation of pits through the autocatalytic mechanism. The detailed process will be explained in the pitting growth stage. Due to the significate influence of chloride ions on the pitting corrosion process, 3.5 wt.% NaCl solution is often used as a simple simulated seawater to study the corrosion process of steel [41-43]. It will also be used as the experimental solution for this project to explore the corrosion process of MC steel.

Metastable pits refer to those pits which emerge and grow within a limited time before passivation. It is the initial state of the pit, and usually lasts only a few seconds before the surface is passivated [44].

On the stage of pit growth, the autocatalytic process of pitting corrosion can be represented by Figure 5. At this stage, the top of the pit is covered with rust formed during the reaction. For iron, this film always has a loose structure. Substances (Cl^-, O_2, Fe^{2+}) in the solution can also be exchanged internally and externally through this cap. However, it also slows down the velocity of the exchange [45]. With the consumption of dissolved oxygen in the pit, most of the cathodic reaction is transferred to the outer surface of the pit point. This spatial change leads to the accumulation of positive ions (Fe^{2+}) in the anodic area, resulting in the attracting negative ions (Cl^-) to achieve neutralization. This process can be expressed by the following formula [46]

$$FeCl_2 + 2H_2O \rightarrow Fe(OH)_2 + 2HCl \qquad \text{Equation 7}$$

Through the hydrolysis process, the process produces free acid, which significantly reduces the pH value at the bottom of the pit. The existence of hydrogen ion and chlorine content increases the corrosion of the steel wall of the pit, prevents re-passivation, and

promotes the continuous diffusion of the pit. Meanwhile, since there are a large number of hydrogen ions in the pit, they can replace oxygen to participate in the cathode reaction. The reaction formula is [46]

$$2H^+ + 2e^- \rightarrow H_2(g)$$
<div align="right">Equation 8</div>

The participation of the hydrogen evolution reaction makes the corrosion rate less affected by the oxygen concentration, resulting in a higher rate can be maintained. This is an autocatalytic process that develops over time, causing more metal to dissolve until the metal perforates.

The generation of the autocatalytic process is related to the hindered ion diffusion and and local concentration increase inside pitting points. This process can occur in the structures like long and narrow crevice and pits covered with rust (Figure 5).
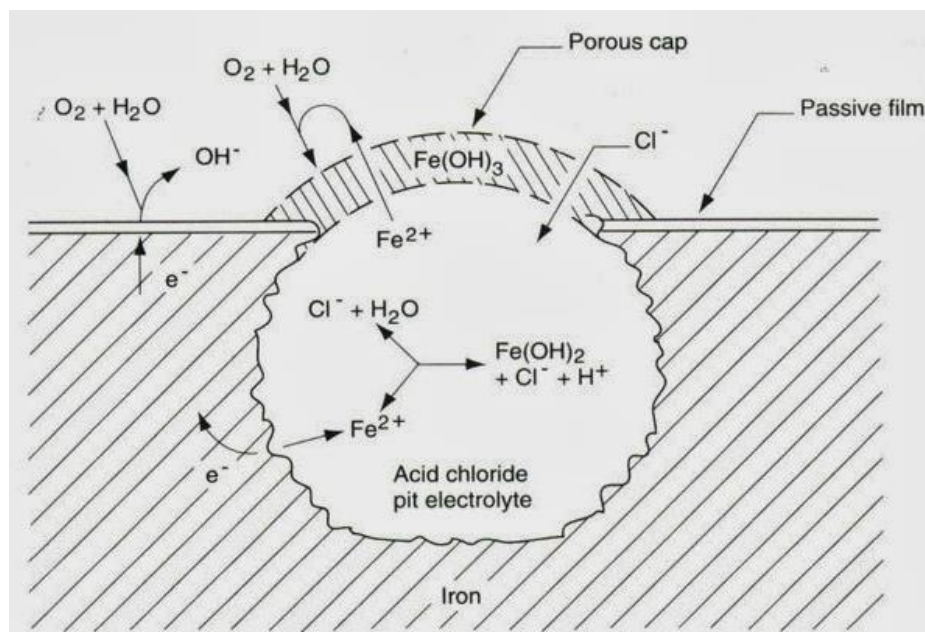
Figure 5 Autocatalytic process occurring in a pitting location freely rendered from [45]

The influence of grain boundaries on pitting corrosion is complex. Typically considered, grain boundaries will cause intergranular corrosion (IGC). It is very common in stainless steel and high temperature environments [47-49]. The sensitivity of stainless steel to the IGC is mainly due to the formation of chromium-depleted regions (chromium-rich carbides) along the grain boundaries [50]. This results in the higher density and energy at the grain boundary, which is the preferred location for oxidation reactions [51]. However, there are also some experiments indicate that pitting corrosion will occur preferentially on the grains rather than grain boundaries [51, 52]. Liu et al. study the in-situ electrochemical characterization of grains and grain boundaries of a HSLA steel in a near-neutral pH solution. For this kind of steel, the grain and grain boundaries of the steel are the anode and the cathode, respectively. After the electrochemical process starts, local corrosion will preferentially occur on the grains [52]. Undoubtedly, the existence of grain boundaries will

contribute to a large number of active dissolution sites.

A beneficial effect of the grain boundary is to effectively form a stable and dense passivation film. This is attributable to the fact that electrochemical reactions easily occur at the grain boundaries. Oxides and passivation films are easily nucleated at the grain boundaries [51]. The second function of the grain boundary is to accelerate the diffusion of alloying elements/impurity elements. This contributes to the formation of a protective passivation film and the release of internal stress [53, 54]. The higher grain boundary density promotes the adhesion of corrosion products to the matrix material, thereby improving the stability of the passivation film [55].

The influence of the grain boundary on the corrosion rate is also contradictory. Grain refinement is often used to improve the mechanical properties of steel. This also brings along a larger number of grains and a large area of grain boundaries. Many experiments have been introduced to explore its effect on corrosion rate. It is generally believed that grain refinement will accelerate the initial corrosion reaction, which is caused by larger areas of grain boundaries. When surface corrosion products are soluble, the corrosion resistance becomes poor. In contrast, grain refinement has a beneficial effect on the formation of dense films in passive systems, which is related to the effective of grain boundary to accelerate element diffusion discussed in the previous paragraph [51, 56].

Regarding the physical environmental factors that will affect the pitting corrosion process, the types and influence trends are roughly the same as those of uniform corrosion, and will not be repeated here.

2.3 Monitoring techniques in marine corrosion

In the process of corrosion monitoring, many techniques are used to characterize various parameters related to corrosion, such as corrosion rate and pitting potential. Generally, these technologies are divided into electrochemical techniques and non-destructive in-situ techniques [34, 57]. This section lists several commonly used techniques which have the ability to monitor corrosion processes in the marine environment, and introduces their latest research results.

2.3.1 Electrochemical techniques

Electrochemical techniques are essential for evaluating the corrosion characteristics of metal components used in industrial structures or in an aggressive environment. They can measure the corrosion rate, the properties of the sample surface, and evaluate the effectiveness of corrosion protection strategies. Depending on the applied current or potential, the electrochemical methods can be divided into two parts: direct current (DC) and alternating current (AC). DC electrochemical methods include open circuit potential (OCP) and potentiodynamic polarization (PDP). An important AC technology in corrosion research is electrochemical impedance spectroscopy (EIS), which can measure the frequency-dependent process in corrosion and a.o. estimate the change in polarization resistance [58]. These techniques will be discussed in turn.

Open circuit potential is the potential difference between the reference electrode and the sample (working electrode) by immersing them in the test environment. It is related to the dynamic equilibrium of the redox reactions taking place at the working electrode [59]. OCP is a technique that can roughly display the corrosion process of the sample surface under natural conditions, simply and intuitively. Wang et al. and Venkatesan et al. characterized the corrosion process of steel by monitoring the change of the OCP value of carbon steel for 50 h and 360 days, respectively [60, 61]. Therefore, it is possible to qualitatively evaluate the influence of various factors on the corrosion process by monitoring the changes in the OCP of the corroded metal over time [58].

Various factors that may affect the redox reaction of sample surface can be tested to obtain the corresponding relationship curve of OCP, such as pH value, temperature, etc. [59, 62]. A decrease in OCP typically represents increased anodic activity at the working electrode, indicating an increase in corrosion activity. By comparing the OCP between different samples, a qualitative assessment of the extent of corrosion can be quickly determined [62-64].

However, this technology cannot distinguish different types of corrosion. It is usually used as a primary monitoring characterization method to stabilize the surface state to better perform other electrochemical detections behind.

Potentiodynamic polarization (PDP) technique can realize rapid corrosion detection and quantitative analysis in a laboratory environment. It mainly applies a driving force to control the electrochemical reaction that occurs on the sample (working electrode) [65]. The magnitude of the driving force can determine the actual electrochemical process and its anodic and cathodic reaction rates, thereby accelerating or diminishing the rate of the corrosion process. During this process, the polarization behavior of the sample can be determined experimentally.

PDP can identify the corrosion characteristics of passivated metals and alloys. It can provide substantial information about electrode processes, such as corrosion rate, pitting sensitivity, passivation, and cathode behavior of electrochemical systems. Meanwhile, PDP is useful for predicting the behavior of materials when exposed to corrosive environments [58]. The reaction process that may occur due to the changes in the environment or on the electrode surface will all be reflected by the change in the total current [65].

In corrosion research, EIS is widely used to study the passivation of metals to determine corrosion rates [58]. Meanwhile, the performance of the inhibitor, the performance of the sacrificial and barrier coatings, and the debonding of the polymer coating can also be investigated [58, 66]. Due to the passivation of the metal as well as the corrosion rate can be done by PDP. The project does not include research related to anti-corrosion coatings. Therefore, EIS will not be used in the monitoring process.

2.3.2 Acoustic emission (AE) technique

In industry, considering the need of application, the corrosion monitoring techniques often need to generate real-time and reliable data under severe conditions. In addition, the detection techniques are expected to be able to detect the status of the components and

equipment in use, and provide corresponding reference data for subsequent maintenance. As a result, the non-destructive in-situ monitoring technologies began to develop rapidly. These techniques usually use the form of probing energy (such as ultrasonic pulses, infrared radiation) to determine the properties of the material or indicate the presence of discontinuities in the material [34].

Among these technologies, AE technology is one of the most popular in-situ methods for monitoring structural health of civil engineering infrastructure. Its advantages mainly come from two aspects. On one hand, they have high sensitivity in monitoring cracks and damage, so they can detect cracks in the early initiation stage of damage. On the other hand, AE detection does not require a signal generating device, which is simple to setup [67]. Therefore, compared with other technologies, it has great potential in in-situ monitoring.
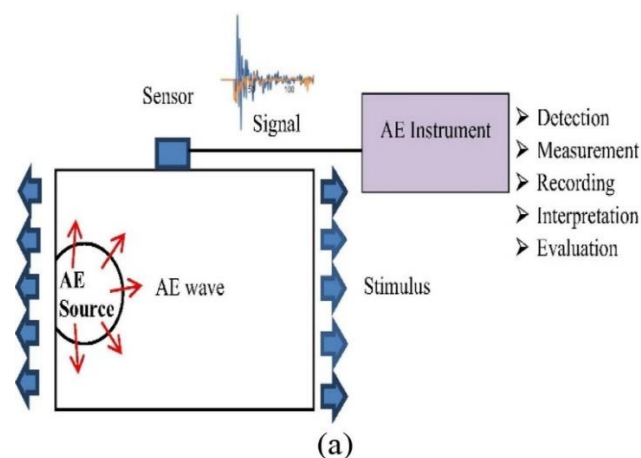
Figure 6 Schematic of AE monitoring freely rendered from [68]

The principle of AE technology is shown in Figure 6, which is mainly based on wave theory. Development or growth of defects in materials, such as yielding, crack propagation, and plastic deformation to form cracks, will produce rapid release of energy and elastic stress waves [67]. The stress wave will be captured by an ultrasound transducer which can convert them to electrical signals. These electrical signals will be recorded, stored, and analyzed by AE data acquisition and proper post-processing tools [68]. Generally, the degree of damage inside the solid can be evaluated based on AE activity and AE waveform parameters [69].

Due to the sensitivity of the AE method to the changes in structure and mechanical properties of the material during the corrosion process, the corresponding AE source has its specific properties [70]. Many studies have successfully attributed these signals to certain sources. In the pitting corrosion process, the damage processes including instantaneous stress changes on the metal surface, rupture of the passivation film, corrosion potential fluctuations and hydrogen bubble evolution have been suggested as possible mechanisms for AE sources [71, 72]. The transformation in corrosion type from pitting to uniform corrosion has also been indicated to be related to the reduction in the hit number of AE signals [73]. In addition, the amplitude, energy, duration, count, and frequency of the AE-signal have been used to classify corrosion stages or source

mechanisms [73-75].

The signal of the decomposition of the oxide film and metal dissolution have been proved to have a smaller amplitude [70]. Therefore, most of the current studies attribute the source of the AE signal to the hydrogen bubbles generated during the corrosion process. This process includes the formation of bubbles, the release of bubbles from the pit, the rupture of the bubbles or their physical interaction with the pit wall (impact or friction) [10, 72, 76]. The amplitude of these sources can be hundreds of microvolts [70]. Meanwhile, the frequency characteristics of the AE signal are related to the size of the bubbles. For example, when the size of the bubbles is about 0.03-0.05 mm, the corresponding signal frequency is 125-225 kHz [76]. Jaubert et al. found that under hydrogen release conditions, the frequency of the signal is centered at 170 kHz, while the bubble friction is centered at 240-250 kHz [77].

By controlling the experimental environment, some studies have successfully monitored the AE signal of a single corrosion process of stainless steel. In the uniform corrosion process, the total number of AE signals at the first 4 hours is related to the number of hydrogen bubbles. These bubbles are produced by the cathodic reaction in acidic environment (Equation 8). The acidic environment can be the overall environment, or it can be a local acidic environment caused by the obstruction of material exchange [70]. The generation of the AE signal is caused by the continuous failure of the passivation film on the surface of the material causes multiple bursts of bubbles. During this period, the fracture rate exceeds the formation rate of the passivation film. At the same time, the bursting amplitude of the bubbles in the narrow interval is relatively high. It is more conducive to signal propagation and collection. Subsequently, the hit of AE rapidly decreased, which was attributed to the fact that the fracture rate was equal to the rate of passivation film formation. The bubble burst is no longer obvious [78]. For pitting corrosion, AE exhibits high activity during the initiation and expansion stage of pitting. During the growth stage, it became more intense. Therefore, the signal predominates in the pits with clogged cells. This phenomenon is especially obvious during the transition period to uniform corrosion [79]. In conclusion, for stainless steel during electrochemical reaction, the AE sources are always from the fracture of the passive film and pitting corrosion [70, 76, 80].

Tang et al. proved that the pitting signal of carbon steel has a high similarity to that of stainless steel through the application of AE technology to monitor the corrosion process of carbon steel in $NaHCO_3$ and NaCl solution [81]. When there are pitting occluded cells on the surface of carbon steel, the autocatalytic reaction will establish severe acid conditions inside the pits. Therefore, the evolution of hydrogen in the pit, more precisely, the friction of the hydrogen bubbles along the pit wall or cell cap can produce a large number of AE signals. It is consistent with the generation principle of the AE signal of stainless steel [73, 81]. However, the occluded unit of carbon steel pitting is unstable and easily ruptured, resulting in a decrease in the strength of the signal during the growth stage [81]. In addition, Jaubert et al. proved that the AE sources during uniform corrosion of carbon steel and stainless steel are both hydrogen release, friction of hydrogen bubbles, and the evolution of corrosion deposits [77].

However, it is obvious that the AE parameters can only be regarded as reference values.

This is due to the uncertainty of the adjustment of AE equipment, the amplitude-frequency characteristics of piezoelectric transducers, the lack of information on wave attenuation and reflection processes, and the lack of unified measurement requirements for signal analysis [70]. Under these conditions, identifying the corrosion process according to AE signal becomes more complicated. Therefore, AE technology is often used together with other in-situ monitoring methods, such as electrochemical detection, optical observation, etc. [72, 82, 83]. These methods allow real-time correlation between the corrosion process and the AE signal.

2. Methodology

This chapter outlines the methodologies for corrosion monitoring. Electrochemical characterization, AE technique, and weight loss experiments are presented in order.

3.1 Electrochemical characterization

According to the discussion in Background and literature review section, DC electrochemical techniques are essential and convenient for evaluating the corrosion characteristics of metal in an aggressive environment. This section mainly discusses the following DC electrochemical method: potentiodynamic polarization. Then there are two commonly used polarization methods: Tafel extrapolation which can identify the corrosion characteristics of metals and linear polarization measured polarization resistance.
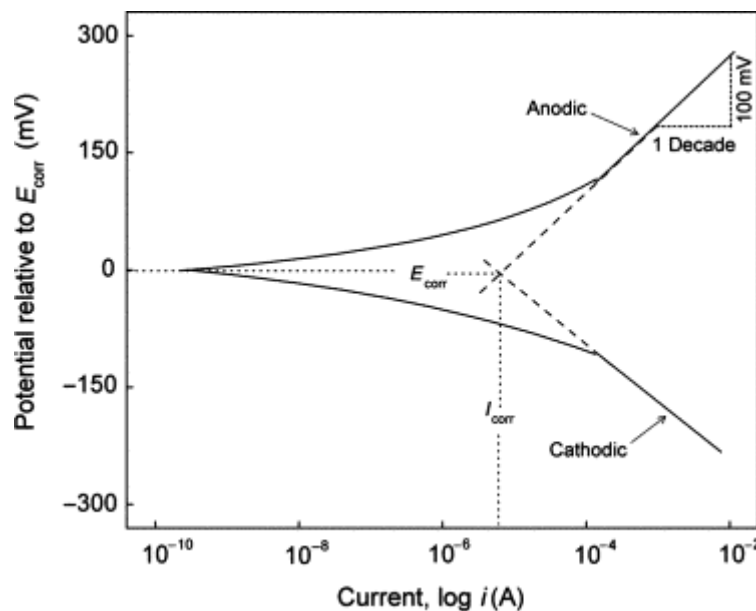
Figure 7 Schematic polarization curve with Tafel extrapolation [58]

Polarization is the process in which the current passing through the electrochemical cell causing a change in the potential of the working electrode (WE), which will result in a balance deviation. During this process, the deviation which leads to a potential difference between polarized and balanced (non-polarized) electrode, is defined as overpotential (η). The evaluation of corrosion behavior is usually done through a series of kinetic parameters. In the one-step reaction under steady-state conditions, the current density function according to the Butler-Volmer equation is [84]

$$i = i_{corr} \left\{ exp \left[\frac{\alpha z F \eta}{RT} \right]_f - exp \left[-\frac{(1-\alpha)zF\eta}{RT} \right]_r \right\}$$

Equation 9

where i = applied current density (A/cm^2)

     i_{corr} = corrosion current density (A/cm^2)

     α = symmetry coefficient (transfer coefficient)

     z = oxidation state or valence number

     F = Faraday constant

     η = E − E_{corr}

     R = universal gas constant

     T = absolute temperature (K)

     f = forward, charge transfer in the anodic direction

     r = reverse, charge transfer in the cathodic direction.

When the overpotential η > 0, the anode polarization is introduced. In this process, the metal surface is oxidized (corroded) by losing electrons; therefore, it is positively charged. On the other hand, cathodic polarization is driven by a negative overpotential because it provides electrons to the metal surface, which means E < E_{corr} [84].

The logarithmic graph |i| vs. E is called the polarization curve (Figure 7) [85]. It can be divided into two parts according to Equation 9. When E > E_{corr}, the curve represents the anodic polarization behavior of metal oxidation. On the contrary, when E < E_{corr}, the curve is the cathode polarization of the gas. Meanwhile, through this curve, the (i_{corr}, E_{corr}) point can be directly determined without obtaining the parameters in advance (the detailed principle will be discussed in 3.1.2.1).

3.1.1 Tafel extrapolation

The Tafel extrapolation method can directly measure the corrosion potential, which is also useful for predicting the corrosion characteristics of various corrosion systems. The polarization data of the sample are obtained by using a three-electrode electrochemical cell which includes a working electrode, a counter electrode and a reference electrode. A typical conventional three-electrode electrochemical corrosion cell is shown in Figure 8. Among them, the reference electrode provides a stable reference potential for the working electrode. The counter electrode is made of a material (platinum or graphite rod) that is inert in the solution. The working electrode is the metal whose corrosion characteristics are investigated. The potential between the working electrode and the reference electrode is gradually changed to measure the current between the working electrode and the counter electrode [58].
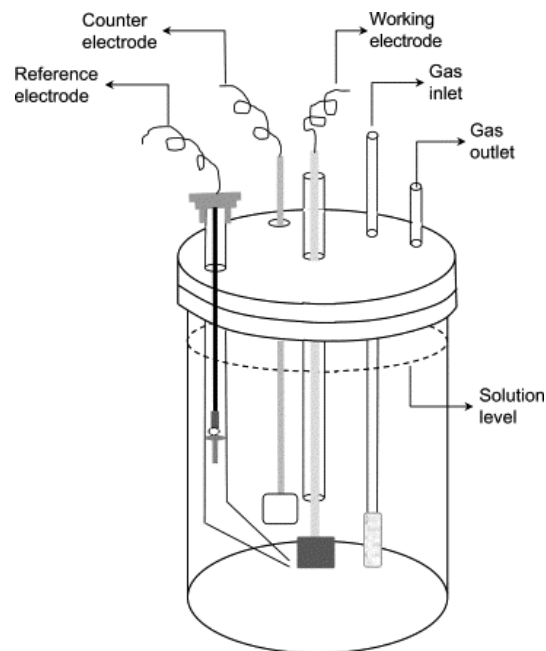
Figure 8 Three-electrode electrochemical cell for corrosion detection [58]

The polarization curve is obtained after the sample reaching a steady OCP state. The linear part of both anodic and cathodic polarization curve is called the Tafel plot [84]. If there is a clear Tafel area in each branch, as shown in Figure 7, they can be extrapolated back to zero overvoltage. The intersection of the Tafel slopes gives the corrosion potential (E_{corr}) and the corrosion current density (i_{corr}) [85]. At E_{corr}, the rate of cathodic reaction is equal to the rate of metal dissolution. The i_{corr} can indicate the corrosion rate of the system [58]. The principle of Tafel extrapolation comes from the Butler-Volmer equation (Equation 9). Under a sufficiently high overvoltage, the rate of the reverse reaction becomes negligible, so Equation 9 can be written as [85]

$$i = i_{corr} exp\left[\frac{\alpha zF(E - E_{corr})}{RT}\right]$$
Equation 10

Taking logarithms in Equation 10

$$logi = logi_{corr} + \frac{\alpha zF}{2.303RT}(E - E_{corr})$$
Equation 11

The graph $log|i|$ gives a straight line with the electrode potential E. When $E = E_{corr}$, $i = i_{corr}$. Therefore, the Tafel area can be extrapolated back to $E = E_{corr}$ to obtain the corrosion current density i_{corr}, as shown in Figure 7.

3.1.2 Linear polarization

One of the problems with the Tafel extrapolation method is that the potential range required to complete the polarization of the sample is relatively large, which often causes significant

change to the surface after polarization. The metal surface may be etched and roughened, sometimes showing its grain structure [85]. It is a destructive technique. Therefore, new specimens must be used to complete the later corrosion evaluation study.

These problems are overcome by the linear polarization method from Stern and Geary. This method depends on the fact that in the vicinity of the corrosion potential (deviations from 10-20 mV), the current density is linearly related to the applied potential, as shown in Figure 9 [58, 85].
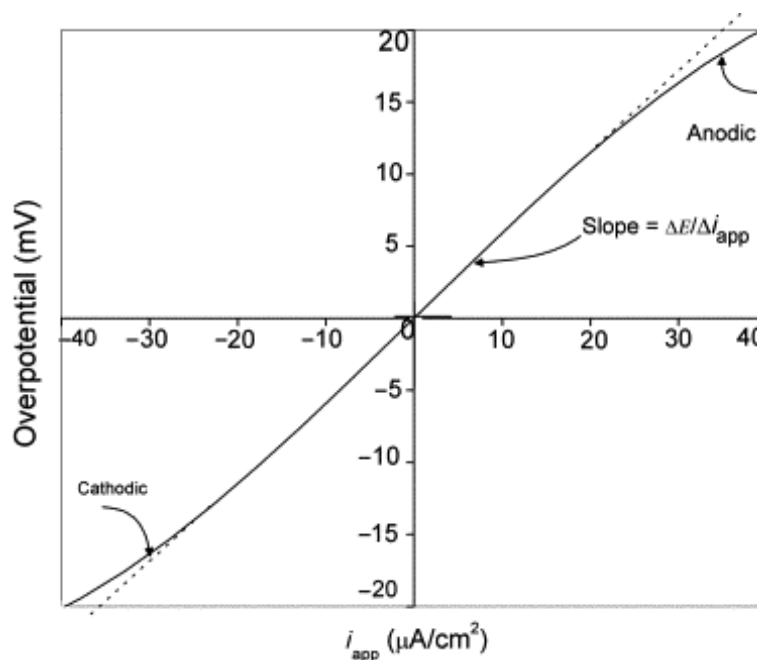
Figure 9 Current-potential relationships for a three-electrode system that shifts slightly (10-20 mV) from its equilibrium state [58]

The linear polarization method is based on the following derivation. When the overpotential in the Butler-Volmer equation (Equation 9) is low enough, which is satisfied by

$$\eta \leq \frac{RT}{zF}$$

Equation 12

The exponential term in Equation 9 can be expanded using $[(e^x - e^{-x})/2 = \sin x]$ and $[\sin x = x, \text{ when } x \to 0]$, which results in

$$exp\left(\frac{\alpha z F \eta}{RT}\right) = 1 - \frac{\alpha z F \eta}{RT}$$

Equation 13

and

$$exp\left(-\frac{(1-\alpha)zF\eta}{RT}\right) = 1 + \left[\frac{(1-\alpha)zF\eta}{RT}\right]$$

Equation 14

Therefore, when $\eta \rightarrow 0$, the current density is

$$i = -i_{corr}\frac{zF}{RT}\eta$$

Equation 15

The ratio of the derivative of the overpotential to the current $\partial\eta/di$ (the slope in Figure 9) represents the resistance in Ohm's law, usually called the polarization resistance (Rp)

$$R_p = \frac{RT}{zFi_{corr}}$$

Equation 16

Equation 16 introduces a better physical explanation for the corrosion current density. Corrosion current density can be used to estimate the resistance of any corrosion or electrochemical reaction. A higher value of corrosion current density means that the reaction rate is increased, while a lower value of corrosion current density means the corrosion kinetics is slow. Meanwhile, Green et al. and Simmons proved that the slope of the linear polarization curve is inversely proportional to the corrosion rate [86, 87]. According to the inference of Stern and Geary, the derivative of overvoltage and current density is linear only in a small range above and below the equilibrium electrode potential. Therefore, the polarization resistance is defined as the slope of the polarization curve at the equilibrium potential (the origin of the polarization curve) [58]. Furthermore, polarization resistance is often used to estimate the corrosion rate.

One advantage of the linear polarization method is that linearly polarized sample can be reused. This is because the degree of polarization is at most about 50 mV with respect to E_{corr}, the electrode surface changes caused are minimal (if any) [85]. Therefore, the linear polarization method can be used to continuously monitor the polarization resistance and the corrosion rate of the sample over time.

3.2 Acoustic emission (AE) technique

Parameter-based analysis is useful to better characterize the AE signals. Analyzing parameters such as hit rate, impact, signal strength, or energy can more easily identify corrosion source and location. A simplified representation of the transmitted signal and common parameters is shown in Figure 10. Table 3 lists the contribution of these parameters in providing information about the source.
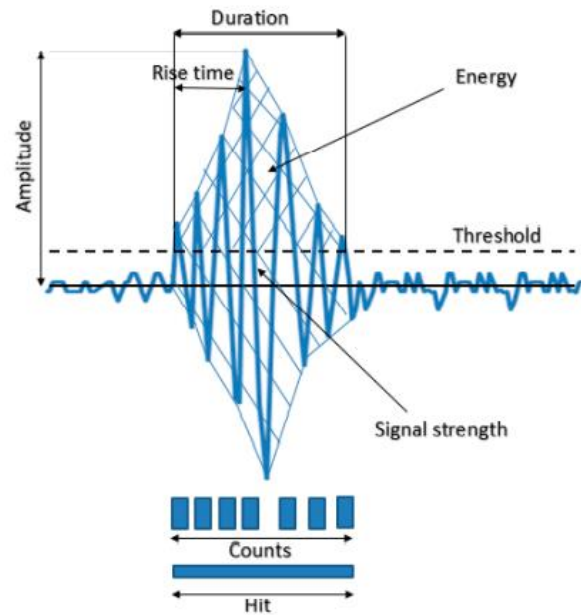
Figure 10 Parameters reflecting of an AE waveform

Table 3 AE parameters and the descriptions to reflect source information

Parameters	Description
Hit	Detection of a signal
Counts	Number of times that signal crosses the threshold
Amplitude	Largest potential peak in the waveforms
Rise time	Time elapsed from signal start to peak amplitude
Duration	Time between signal start and end
Threshold	Electronic compactor to record signals with amplitude greater than this level
Signal strength	Area under the positive and negative envelope of linear potential signal

3.3 Weight loss

The sample needs to be weighed twice in the weight loss experiment. The first time is after the treatment of grinding and cleaning. The second time is to weigh the corroded sample after corrosion products on the surface are completely removed. The corrosion rate is determined by using the following equation [88]

$$C_R = \frac{W_a - W_b}{At}$$

Equation 17

In the equation, W_a and W_b are the weight of the sample before and after the corrosion, A is the total exposed area of the sample (cm^2) and t is the immersion time (day).

3.4 Standard deviation

Standard deviation is most commonly used in probability and statistics to express the degree of dispersion of a set of values. It has two properties: i) a non-negative value; ii) the same unit as the measurement data. It can be calculated by the following formula [89]

$$SD = \sqrt{\frac{1}{n-1}\sum_{i=1}^{n}(x_i - \bar{x})^2}$$

Equation 18

In the equation, $\bar{x}$ is the mean value of the measurement data.

3. Experiments

This chapter presents the setups for corrosion monitoring. Electrochemical characterization, AE technique, and morphology experiments are introduced in partial order.

4.1 Corrosion experimental setup

Before the electrochemical detection, the sample's surface is prepared by grinding with SiC sandpaper, from P180 to P1200 in turn. After this step, the surface is cleaned with isopropanol and dried with airflow. The prepared samples that are not to be used immediately will be stored in an environmentally controlled room (the temperature is 22 °C, the humidity is 60%) to keep the surface fresh.

The BioLogic VSP-300 potentiostat is used during the electrochemical experiments of all samples. It is controlled by the EC-Lab software. In order to keep the test area constant, the tape is wrapped on the sample surface, exposing only a circular area with a diameter of 2 cm. The sample is fixed on a customized supporter and placed in a beaker (as shown in Figure 11). The sample works as the working electrode which contacts with the red detector. The platinum mesh is the counter electrode which contact with the blue sensor. The Ag/AgCl (3MKCl) electrode is used as the reference electrode (0.192 V vs. standard hydrogen electrode) which is placed in front of the exposed side of the sample. The experiment is carried out in 3.5 wt.% NaCl solution. The device is placed in a monitoring box to avoid interference from external electromagnetic fields.

Figure 11 Electrochemical detection experimental device and original sample morphology
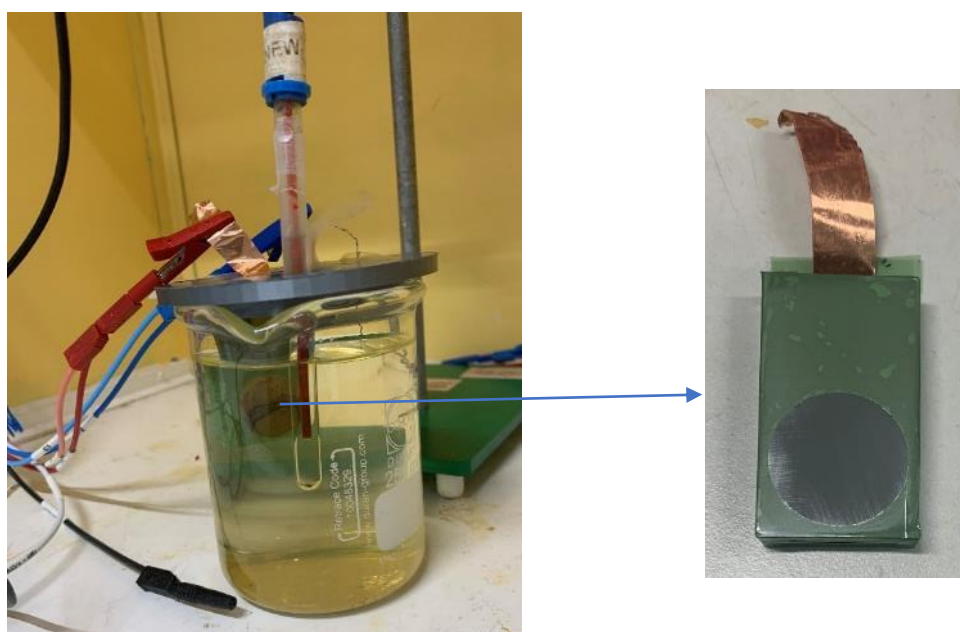
In the experiment to explore the effect of flow velocity on the corrosion process, an additional magneton is placed at the bottom of the beaker to generate flowing water. The beaker is placed on the Labinco L-366 control-visc [Figure A. 1 (a)]. The sample placement is shown in Figure A. 1 (c). The magneton rotates in the center of the beaker, causing a circular eddy current. The sample is placed parallel to the diameter of the beaker, with the exposed area facing the center of rotation. This kind of placement aims to ensure that the exposed area is subjected to the same flow velocity as possible. In the temperature-related experiments, the entire experimental beaker is placed in a double-layer beaker for heat preservation in a water bath [Figure A. 1 (b)]. The Huber MPC-K6 thermostat controls the temperature of the whole system.

Before starting the potentiodynamic polarization measurement, an OCP detection will be performed for one hour to obtain a stable E_{OCP}. Then the measure is applied in the potential range of -250 mV to +250 mV relative to E_{OCP}. The scan rate is 0.167 mV/s.

The detection work can be divided into two parts for the samples used in the experiments related to long-term immersion and environmental influence factors. The first part is OCP detection lasting for a certain period. The second part is linear polarization resistant (LPR) detection. The detection potential range is from -30 mV to +30 mV relative to E_{OCP}. The scan rate is 0.167 mV/s. In the long-term immersion experiments, samples are tested at a fixed time every day, and the duration of OCP detection is 1 hour.

In the experiments related to flow velocity, the experiment time is set to last for 1 day. Therefore, these two parts of the monitoring are repeated multiple times. According to the time when the sample reaches the stable state, the numbers of cycles at different velocities are different, as shown in Table 4. In the temperature control experiment, the detection scheme is the same as that at 0 rad.

Table 4 Electrochemical detection strategies at different flow velocities

Velocity	OCP (min)	LPR (min)	Cycles (times)	OCP	LPR (min)	Cycles (times)
50 rad	54	6	10	2h 40min	6	5
100 rad	54	6	8	3h 5min	6	5
0, 200-500 rad	54	6	6	3h 30min	6	5

4.2 Experimental setup with AE monitoring technique

The electrochemical acceleration process in the AE monitoring experiment is also provided by the BioLogic VSP-300 potentiostat. The surface treatment of the sample and the installation of the three-electrode system are consistent with the long-term immersion experiments. Similarly, the entire device (Figure A. 2) is placed in the monitoring box. Except for Case 1 (black control experiment), the other samples are all applied with specific potential (as shown in Table 5). At the same time, the current between the sample and the counter electrode is recorded to reflect the corrosion process.

Table 5 Acceleration potential application strategies in AE monitoring experiments

Experiments	Case 1	Case 2	Case 3	Case 4
Applied potential	-	+0.04 V vs E_{OCP}	+0.04 V vs E_{OCP}	E_{OCP}

The AE signal emitted from the sample during monitoring is acquired using a data acquisition system (Vallen AMSY-6) via a watertight resonance type pre-amplified transducer (VS150-RIC). The sensor is fixed on the bottom of the beaker below the sample to ensure that the collected signal mainly comes from the corrosion process on the sample surface. The AE signal is amplified by the embedded preamplifier and passed through to the DAQ. The amplification rate is set to 35 dB, and the threshold is 40 dB to eliminate background noise in the experiment.

4.3 Morphology detection

The Keyence VHX-5000 digital optical microscope (DOM) is used to observe the morphology of the rust layer on the top of the surface and the corroded surface of the matrix. The samples with the rust layers are cleaned with gentle distilled water before observation. The method to remove the rust layer is to place the sample in an ultrasonic bath and clean it with distilled water until the surface is free of rust. After cleaning, the samples are all dried by airflow.

The 3D image of DOM is used to measure the thickness of rust layer and the depth of pitting points in different samples. It is obtained through the "Fine Depth Combination" mode. This mode can capture multiple images in focus at different heights, then compose them to display a 3D image with high quality in containing height information.

5. Results and discussion

This chapter introduces experimental results and discussion. It starts from the Tafel plot detected by potentiodynamic polarization detection. Then is the results of long-term immersion and the accelerated corrosion process monitored by AE and electrochemical techniques. Finally, the influence of two environmental factors, flow velocity and temperature, on the corrosion process are discussed. Each section is divided into two parts: monitoring technique results and morphology. In order to make the analysis clearer, most of the microstructure morphology of the samples are equipped with height difference figures in color. They are shown in the appendix.

5.1 Potentiodynamic polarization measurements

The potentiodynamic polarization results are analyzed by the Tafel extrapolation. The Tafel plot of MC steel is used to identify the electrochemical response of the sample under dynamic potential changing, as shown in Figure 12. It comes from the most representative of the three repeated experiments. Table 6 lists the critical electrochemical parameters obtained from the polarization curve, i) the corrosion potential and ii) corrosion current density of this mooring chain steel are -0.751 V [Ag/AgCl (3M KCl)] and 0.002 mA/cm^2, respectively. The data are based on the average of three experiments.

There is no obvious inflection point in the anodic polarization branch. It proves that iron dissolution (Equation 1) is the main electrochemical process within the range of applied potential. There is no passivation film with corrosion resistance formed during the detection. As the potential of the anodic branch increases, the overpotential increases. The current which flows in the loop increase, causing more electrons to be involved in the reaction. More electrons accelerate the reaction rate, resulting in a quicker iron dissolution rate.
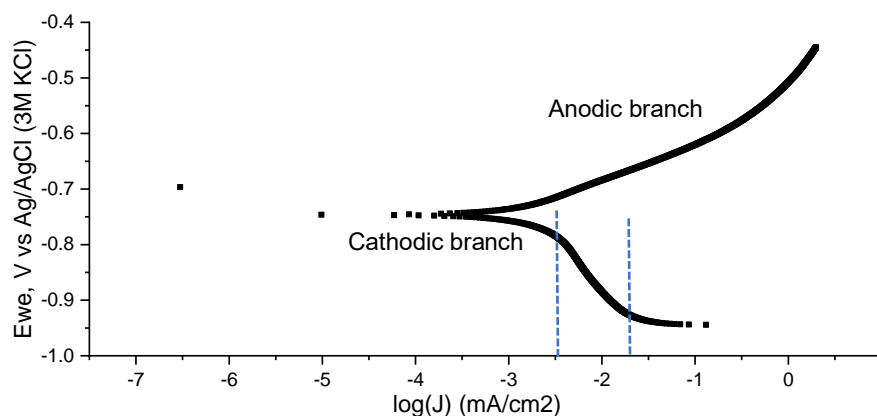

Figure 12 Potentiodynamic polarization curve obtained for the MC steel in 3.5 wt.% NaCl solution

Table 6 Electrochemical parameters of the MC steel in 3.5 wt.% NaCl solution

Sample	E corr [mV vs Ag/AgCl (3M KCl)]	i corr ($\mu A/cm^2$)	β Anodic (mV/dec)	β Cathodic (mV/dec)
S420MC	-751 ± 16	2	75 ± 1	163 ± 2

The cathodic polarization branch appears as three parts with different slopes (a dotted line separates these three stages in Figure 12). As the overpotential becomes more and more negative, the current density increases and the corrosion process gradually deviate from the equilibrium position. Considering the reaction process of iron in a neutral solution (Equation 3), oxygen plays a vital role. According to the theory of polarization dynamics, the first stage with the smaller absolute slope value can be attributed to the activation polarization of oxygen [90]. Due to applying a negative overpotential, oxygen begins to undergo a reduction reaction on the counter electrode. However, due to the small current in the circuit, the number of electrons that can participate in the reduction reaction is negligible. Therefore, the reaction rate is affected by the speed of electron flow in the circuit [84]. The cathodic reaction of the second stage is controlled by oxygen diffusion. The corrosion rate is limited by the oxygen diffusion rate [90]. Since the cathodic reaction of iron corrosion is an oxygen reduction reaction, the diagonal line used to extrapolate the corrosion equilibrium point can be obtained by linear fitting the data at this stage. The slope value of the cathodic branch in Table 6 is also obtained from this stage. When the over-potential continues to decrease, it enters the third stage. As the electrochemical reaction progresses, dissolved oxygen is continuously consumed. However, the electrons in the counter electrode continue to increase. Oxygen can no longer meet the needs of the cathodic reaction. In the literature, the third stage is usually attributed to the hydrogen evolution reaction (HER) [90]. Calculating the Nernst potential equation required by HER, in a solution with a pH of 7, the hydrogen evolution potential of iron is -0.701 V [Ag/AgCl (3M KCl)] [91]. The potential value corresponding to the second inflection point in the cathodic branch is about -0.95 V [Ag/AgCl (3M KCl)]. The deviation is 26%. Due to the lack of observation of the counter electrode during the experiments, it is still uncertain whether this deviation is an experimental error or a principal mistake. Therefore, more electrode observations and a more extensive polarization range need to be introduced to explore the dominant mechanism of the third stage.

In conclusion, the surface does not produce a passivation film with corrosion resistance during the immersion process. MC steel continues to dissolve in the NaCl solution. At the same time, there is a possibility that the cathodic reaction changes from oxygen dissolution to hydrogen evolution in this environment.

5.2 Long-term immersion corrosion process

Long-term immersion experiments are introduced to explore the natural corrosion process of MC steel in seven days. The corrosion process is fully characterized through the

combination of electrochemical detection (OCP and LPR) and morphology observation (DOM). OCP and LPR are used to react to the changes in the electrochemical state of the surface. DOM is used to observe the morphology of the rust layer and the underlying matrix under different immersion days. In order to ensure the accuracy of the morphology observation, seven parallel samples are used for different immersion time experiments. However, this may introduce some errors in the experimental results. The experiments under each condition are repeated three times. The results of the electrochemical part are the average of these three experiments. The DOM results select the figures with the most common properties under each experimental condition.

5.2.1 Electrochemical analysis
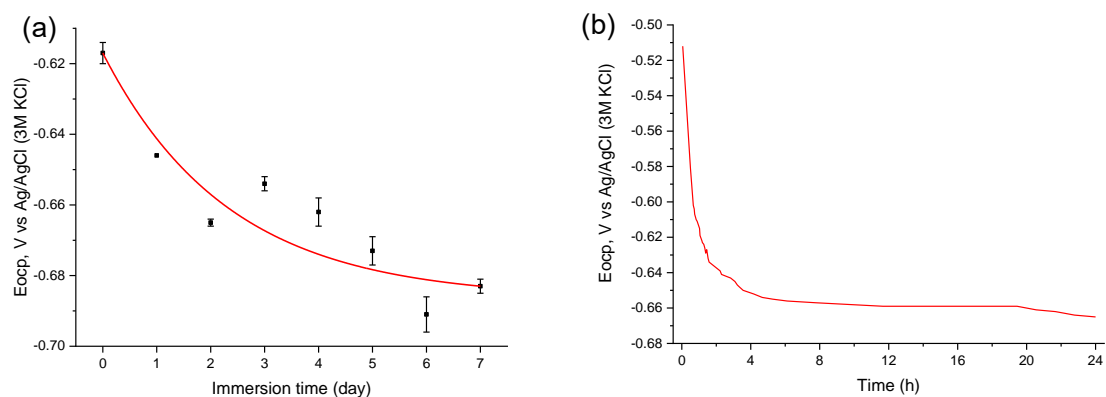
Figure 13 Evolution of E_{OCP} with the time of MC steel in 3.5 wt.% NaCl solution: (a) in the first day; (b) in one week

The electrochemical analysis starts with OCP, which is also necessary before linear polarization resistance detection. The evolutions of E_{OCP} over time of MC steel immersed in NaCl solution for 24 hours and one week are shown in Figure 13. Figure 13 (a) comes from the most representative of the three repeated experiments. Data recording starts after the potential change rate is less than 0.1 V/h. The previous part is considered the unstable state of the sample at the initial stage of contact with the solution. The data in Figure 13 (b) select the potential in the region where the rate of change is less than 0.015 V/h. In this situation, the potential can be recognized as a stable value, which can represent the E_{OCP} of the sample surface. The average of the potential data of three repetitive experiments is used for plotting. The error bars represent the standard deviation of each average value.

Figure 13(a) shows that the E_{OCP} approaches relatively stable after 4 hours of immersion. In the initial stage, the E_{OCP} dropped rapidly from -0.51 V to -0.65 V [Ag/AgCl (3M KCl)]. The performance of the initial stage of the corrosion process mainly depends on the electrochemical reactivity of the matrix [92]. If there are many sites that can induce the initiation of an electrochemical reaction on the original surface, the reactivity of the reaction sample will be higher, and the initiation will be faster. For MC steel, the difference in grain size is the main factor affecting the surface activity of the matrix discussed in section 2.2.2.2. MC steel has a smaller grain size in the microstructure. When exposed to a corrosive environment, the grain boundary is preferred to induce electrochemical reactions

with grains [93]. It leads to the rapid corrosion response in the initial stage.

According to the changing trend of Figure 13 (a), the data in Figure 13 (b) are fitted nonlinearly. The R-square value of the fitted curve is 0.820, which proves that the fitted curve has a good correlation with the data. During one-week long-term immersion, E_{OCP} fluctuates between -0.65 V and -0.69 V [Ag/AgCl (3M KCl)]. As the immersion time increases, the OCP value shows a downward trend. After rapid initiation, the corrosion enters the development stage. At this stage, the intensity of the corrosion process does not change much. The matrix is continuing to be corroded to produce a large number of rusts. The rusts accumulate on the surface to form a rust layer. The construction process will be discussed in detail in morphology analysis.

Another parameter that can provide information about the corrosion process is the polarization resistance (Rp). It indicates steel's ability to prevent the passage of electric current in a given solution [94]. Figure 14 shows the relationship of Rp of MC steel in NaCl solution with time. These data are from the average of three repeated experiments. The error bars represent the standard deviation of each average.

Typically considered, systems with higher Rp are less susceptible to corrosion and have better corrosion resistance [95, 96]. Therefore, steel has the highest corrosion resistance at the initial immersion stage with Rp equal to 2027 Ohm.cm^2. As the immersion days increases, the value of Rp decreases to 1028 Ohm.cm^2, which means the corrosion resistance decreases. At the same time, a decrease in Rp means an increase in corrosion current (Equation 16). A larger corrosion current will cause more electrons to circulate between the anodic and cathodic electrodes. More electrochemical reactions will occur, resulting in a higher corrosion rate. Therefore, the polarization resistance is inversely proportional to the corrosion rate. According to this conclusion, as the immersion days increase, the corrosion rate increases.
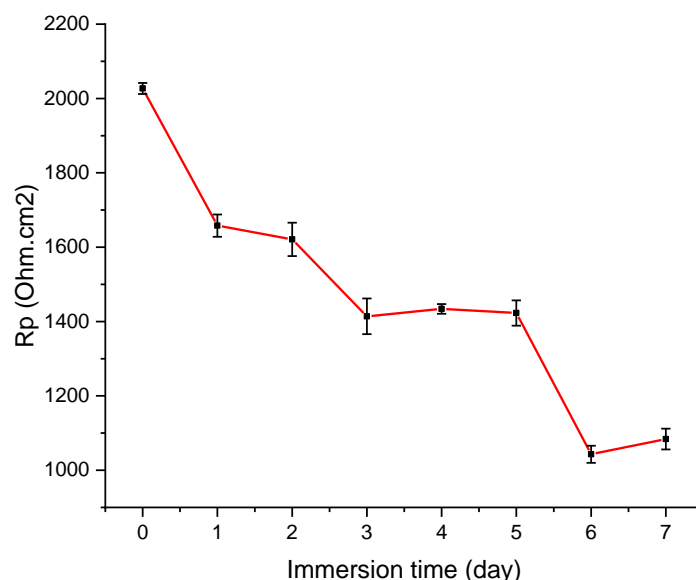

Figure 14 Time dependence of Rp for MC steel in 3.5 wt.% NaCl solution

The daily corrosion rate of MC steel in NaCl solution is calculated according to the weight

loss test. In Figure 15, the black dots are the average corrosion rate of MC steel under different immersion days. These data are from three repeated experiments. The error bars represent the standard deviation of each average. The red line is the average of these seven corrosion rates, which is 0.50 ± 0.04 mg/(cm^2*day). During this one-week immersion, the corrosion rate fluctuated irregularly around the average value. However, the difference (8%) between each point and the average is within an acceptable range. Therefore, this gap is considered to be the fluctuation of the sample and the reaction environment.
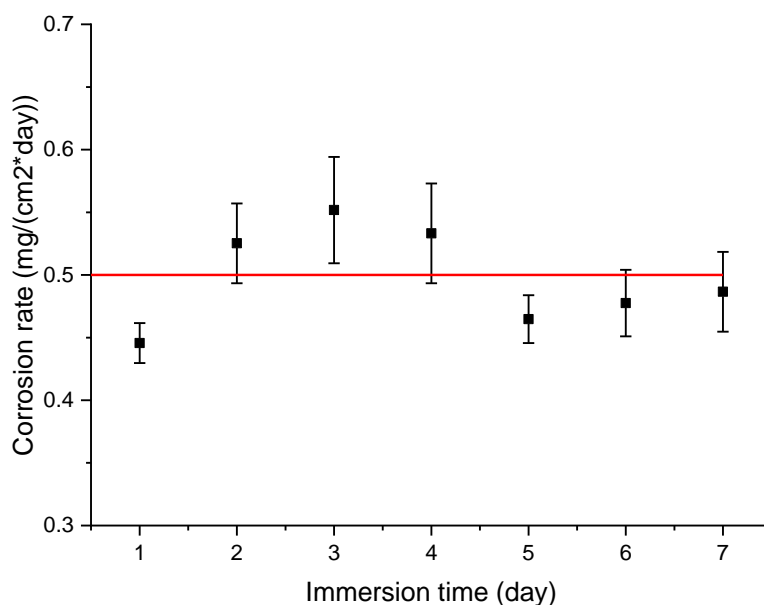
Figure 15 The corrosion rate of MC steel in 3.5 wt.% NaCl solution

From the above analysis, the electrochemical parameters (E_{OCP}, Rp) decrease rapidly in the initial stage of the reaction. It may be related to the high proportion of grain boundaries in the microstructure of MC steel, which leads to a higher initiate velocity of corrosion. After that, when the reaction progressed to the later stage, the decline trend of electrochemical parameters is significantly slowed down. It may be related to the rust layer on the surface, which have enough thickness to provide a certain degree of protection from the attack of corrosive ions. The rationale for this speculation will be discussed in the next section.

5.2.2 Morphology analysis

The evolution of the macro morphology of MC steel with corrosion products in NaCl solution is shown in Figure 16. The morphology figures come from seven samples with different immersion times. Due to Cl⁻ ions in the solution, MC steel has been corroded from the first day of immersion to produce a rust layer. The rust layers of different samples are irregularly distributed in area and shape. The irregular shape can be attributed to the initial corrosion point's randomness. However, for the area, from the analysis of electrochemical data that corrosion will exist over time. Rust will continue to be produced. Thus, the area covered by it should become larger. However, the corrosion area fluctuates between different samples. It may be related to the difference in microstructure between samples. Existing

experiments cannot prove the correctness of this guess. Some advanced technologies can be introduced in subsequent experiments to study this phenomenon. For example, scanning electron microscope with greater magnification can characterize the corrosion area, or electron backscatter diffraction can be used to study the property of the grain boundaries [51].

However, despite their different sizes and shapes, they are all concentrated in the bottom part, which is related to how the samples are immersed. The sample is immersed vertically in the solution. At the beginning of the corrosion, the loose products sink under the action of gravity and accumulate in the bottom part of the sample, causing the rust layer to grow from the lower part.

The sample surface can be roughly divided into three parts: i) unreacted part, ii) low-corrosion part, and iii) rust layer covered area [as shown in Figure 16 (c)]. The unreacted area showed an original smooth surface. The low-corrosion zone shows a large number of corrosion initial points without being covered by rusts. The rust layer covered area has produced orange corrosion rusts. As the immersion time increases, the unreacted area gradually disappears, and the area of the low-corrosion area expands.
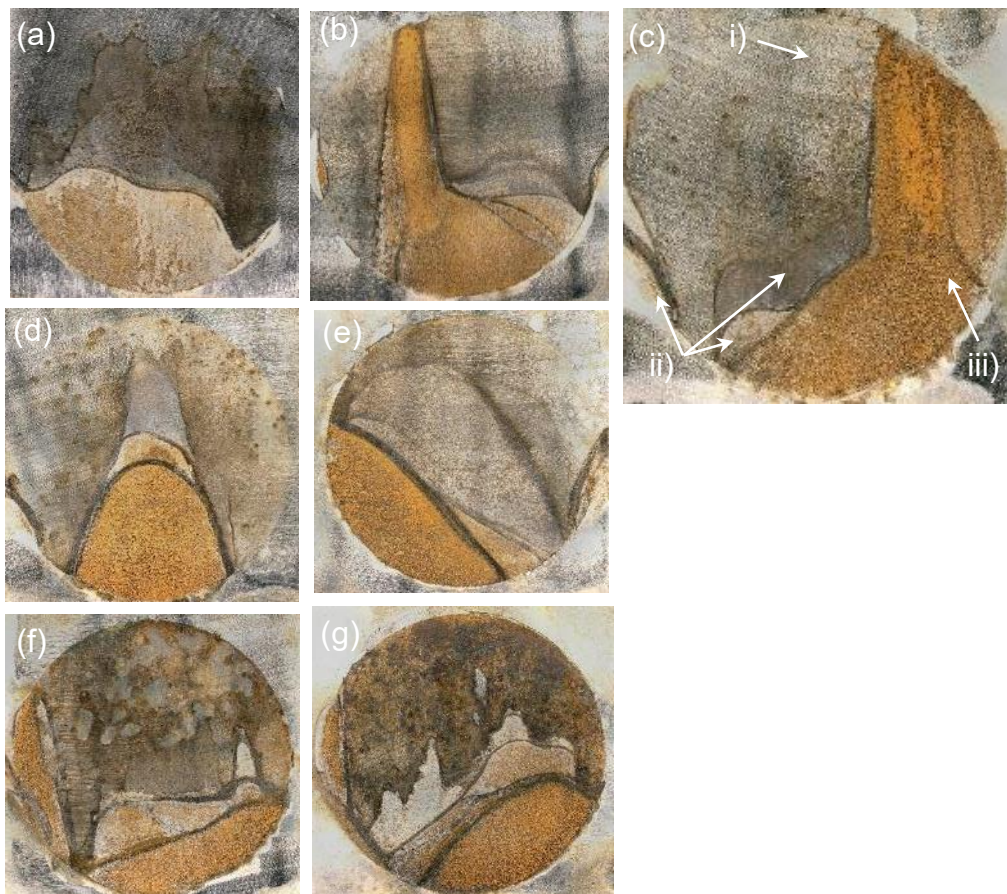
Figure 16 The evolution of the macro morphology of MC steel in NaCl solution with different immersion days: (a) 1 day; (b) 2 days; (c) 3 days; (d) 4 days; (e) 5 days; (f) 6 days; (g) 7days
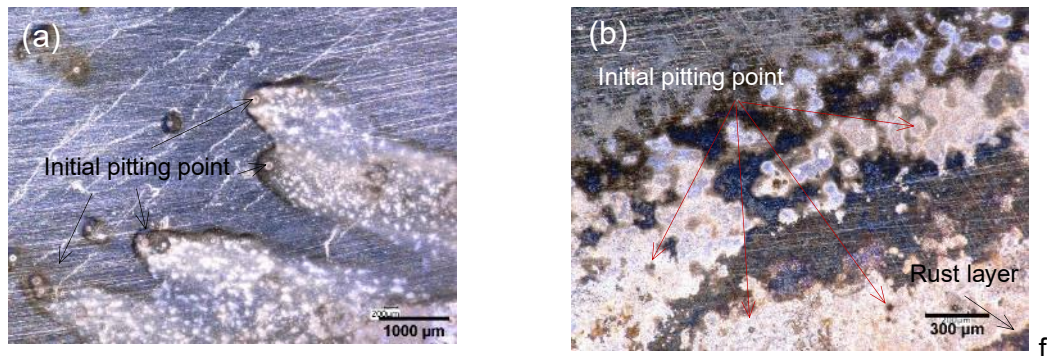
Figure 17 Observation by digital optical microscopy of a low-corrosion area of a sample immersed for 4 days in 3.5 wt.% solution under (a)×50; (b)×150 magnification

Figure 17 shows two different morphologies in the low-corrosion zone. Since the morphologies of the low-corrosion areas of the samples under the seven conditions are more similar, the samples after immersion for four days are selected as representatives for discussion here. In part close to the unreacted area, the surface is dominated by meteor-shaped pitting initial points [Figure 17(a)]. The blue area is the original surface. Silver dots and black edges represent the starting points. These initial points have large diameter (around 100 µm). Their thickness cannot be detected by DOM. Similarly, under the influence of gravity, the corrosion area caused by pitting corrosion is located below the initial point with white color. In part close to the corrosion layer area [Figure 17 (b)], the density of initiation points increases and appears in pieces. At this time, the color of the original surface is dark blue. It may be a passivation layer formed on the surface at the beginning stage of corrosion. It is mainly caused by the small amount of nickel contained in the sample. However, this passivation layer is thin and lacks sufficient corrosion resistance. As a result, it is quickly destroyed to produce areas of pitting corrosion.
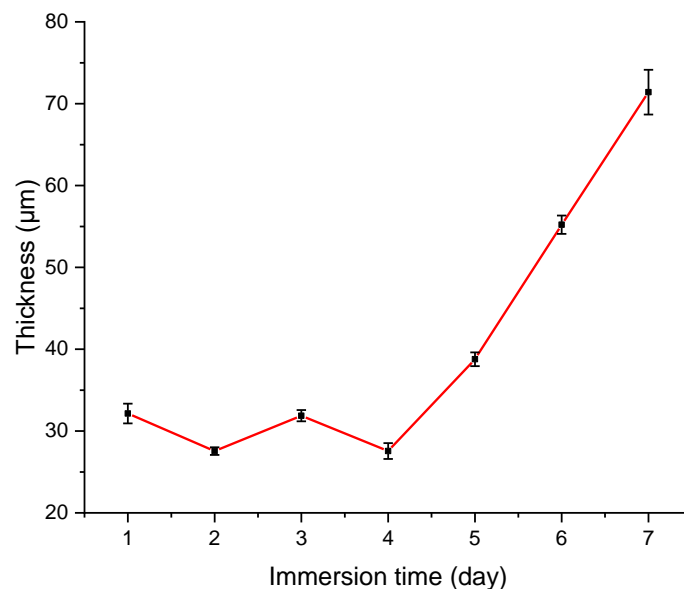
Figure 18 Time dependence of the thickness of rust layer for MC steel in 3.5 wt.% NaCl solution

Figure 18 represents the correlation between the thickness of the rust layer and the number of immersing days. The thickness is detected by many measurements (7 times) on the rust layer under the "fine depth test" mode of DOM. In this mode, the instrument can use different colors to demarcate areas with different heights, as shown in A. 3. Dark blue is used to demarcate the area where the lowest point is located. Red indicates the area with the greatest height difference from the lowest point. The most widely distributed color in the corrosion layer is considered to represent the height in this area. Subtracting this height from the height of the matrix can obtain the thickness of the rust layer. The average value is calculated for each condition based on these values. The error bars represent the error of each average.

In the first four days, the thickness of the rust layer fluctuates around 30 μm. In the following three days, it rapidly goes to 71 μm, increasing about 140 %. It is speculated that in the first four days of the corrosion process, the rusts on the surface mainly focus on establishing a stable layer. After that, the newly generated rusts are mainly used to increase the film thickness.
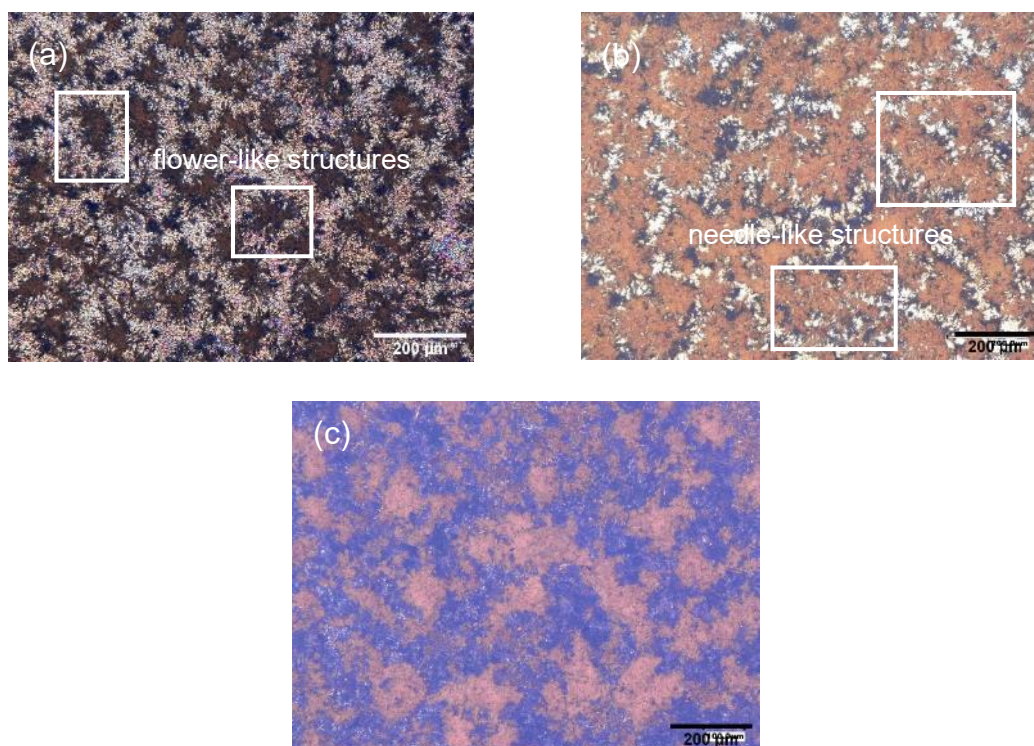
Figure 19 The morphology of rust layer of the sample immersed for (a) 1 day; (b) 4 days; (c) 7 days under ×300 magnification

Figure 19 contains the microstructure of the rust layer after immersion for 1 day, 4 days, and 7 days. For better observation, the height difference figures of these three are shown in Figure A. 3. The color difference of the three figures in Figure 19 is caused by the different brightness used during the observation process. Different brightness is used to obtain a micro-topography with more details. For example, the surface of the sample after immersion for 1 day has fewer rusts, exposing a large amount of matrix. The surface of the

matrix is smooth and easy to reflect light, so the brightness used for observation is low. On the contrary, the rusts increase on the surface of the sample immersed after 7 days. The reflective area decreased. Therefore, the required detect brightness increases.

These three microstructures of the rust layer in Figure 19 all show apparent delamination: orange-brown outer layer and dark gray inner layer. A previous study pointed out that this layered structure has no relation to steel composition [97]. Whether it is carbon steel or weathering steel, rust delamination always exists. The inner layer is dense and has strong adhesion to the substrate. It accounts for the most significant portion of steel's anti-corrosion behavior providing specific protection for the substrate [97-99]. The outer layer is porous, more permeable, and has lower substrate adhesion. It is generally considered to be less protective [97, 99].

The composition detection of corrosion products is not included in the experiment. However, by comparing with the literature, some guesses will be given. During the long-term immersion of carbon steel in the marine environment, Refait et al. prove the presence of Fe(III) oxyhydroxide in the outer orange rust, including goethite (α-FeOOH) and lepidocrocite (γ-FeOOH) . The inner black layer is composed of magnetite (Fe_3O_4) and Fe(III) oxyhydroxide [100]. Wang et al. also find maghemite (γ-Fe_2O_3) in both the inner and outer layers of the HSLA steel used in pipelines [101]. In conclusion, the composition of the rust substances will be affected by the experimental environment and sample composition. Therefore, to determine the composition of the rust in this experiment, more techniques need to be introduced for characterization.

After one day of immersion, the corrosion products formed on the surface are mainly flower-like structures [the white frame area in Figure 19 (a) and Figure A. 3 (a)] with a diameter of about 100 μm. It usually exhibits a thicker and flat central area. The edge is needle-shaped with a lower thickness. These minor gathering points are independent of each other, with few joints. This microscopic morphology is often attributed to the existence of lepidocrocite (γ-FeOOH) [99]. When prolonged immersion time, the flower-like structure on the surface becomes denser with a larger size. They connect to each other.

The rusts have levelled out by the fourth day [Figure 19 (b)]. Some needle-like structure rusts begin to show a greater thickness than the flat area, as shown in the white box in Figure 19 (b) and Figure A. 3 (b). It may indicate that the rusts initially grow as a needle-like structure. This growth is manifested in the expansion of the edge of the gathering points and the thickness growth. Meanwhile, compared with the first day, the delamination of the rust layer is more apparent at this time instance. The color difference between the inner and outer layers can also be clearly seen. Afterwards, the black-grey corrosion products in the bottom layer gradually spread and covered the surface of the matrix.

On the seventh day [Figure 19 (c)], the smooth substrate is no longer visible. Black-gray corrosion rusts entirely cover the surface. The outer orange rust layer has poor continuity. It shows noticeable thickness differences [which is more intuitively in Figure A. 3 (c)]. The thickness of the corrosion layer is mainly contributed by the corrosion rusts of the outer layer.

By linking the morphology with the changing trend of E_{OCP} and Rp, the corrosion process of MC steel in seven days can be obtained. At the beginning of immersion, due to the high proportion of grain boundaries in the microstructure of MC steel, corrosion reaction is

quickly initiated. The reaction continues to generate rusts that have accumulated on the surface. The growth of the rust layer begins with the transform of the surface morphology from needle-like structure to flat. When the flat layer is established, the newly generated rusts increase the film thickness rapidly. The thicker corrosion layer has a specific effect of hindering the material exchange on the surface, protecting the surface against the erosion of Cl^- ions. It has brought a slowdown in the downward trend of electrochemical parameters. However, judging from the available data, this kind of resistance is limited. It may be because the outer layer, which mainly contributes to the thickness of the rust layer, is insufficient to provide defense capabilities. The inner layer that can provide defense is small in thickness, which leads to lower capability.

5.3 Monitoring the accelerated corrosion process with the combination of AE and electrochemical techniques

In this part of the experiments, AE and electrochemical techniques monitor the accelerated corrosion process. The addition of an electrochemical technique is expected to help distinguish the source of AE events to find characteristic signals. At the same time, the morphology of the matrix after accelerated corrosion is also helpful to explore the corrosion process. The data included in the discussion are from the most representative set of experiments. In order to show more precise results, the height difference figure in color of most of the micro-topography is applied in the appendix.

5.3.1 Identification of AE signals from MC steel corrosion process

The analysis of the AE signal starts with the removal of noise. After observing the background noise level, the signals in which the threshold crossing counts are greater than 5 and the amplitude are greater than 50 dB are selected for statistics. These data are plotted against time together with the current density, as shown in Figure 20. Signals below this strategy are considered to be noise during the experiment.
With this select strategy, the effective signal of Case 1 is almost zero. This phenomenon may be due to the relatively short experimental time for the experiment. The sample has not yet reached the stage where the corrosion rate is relatively high (such as the pitting growth stage). On the other hand, the signal intensity generated in the natural corrosion process is relatively small. It may be confused with the noise signal or directly covered by noise.
The division of corrosion stages is mainly based on the trend of current density, as shown in Figure 20. Take Case 2 [Figure 20 (a)] as an example, and it has four stages. In the first stage, the current rapidly rises and reaches a peak value, which corresponds to corrosion initiation. Then enter the second stage of stability. At this stage, the corrosion rate is mainly limited by the oxygen concentration [corresponding to the second stage in the Melchers model (Figure 4)]. The oxygen concentration around the sample remains constant, which leads to a stable corrosion rate. Meanwhile, there is sufficient oxygen in the solution to

supply the reaction surface at this stage continuously. Therefore, the stable corrosion rate has a higher value. In the third stage, the current density drops. This phenomenon may be related to the growth of the rust layer. Suppose the rust layer with a specific protective effect is established on the surface. In that case, it can prevent the surface from contacting Cl-, thereby reducing the rate of metal dissolution. As a result, the corrosion rate begins to be limited by the anodic reaction. Eventually, a new equilibrium state with a lower corrosion rate is reached (stage 4). The feasibility of this guess needs to be determined in conjunction with morphological analysis. For Case 3 and 4, there are three and two corrosion stages, respectively.
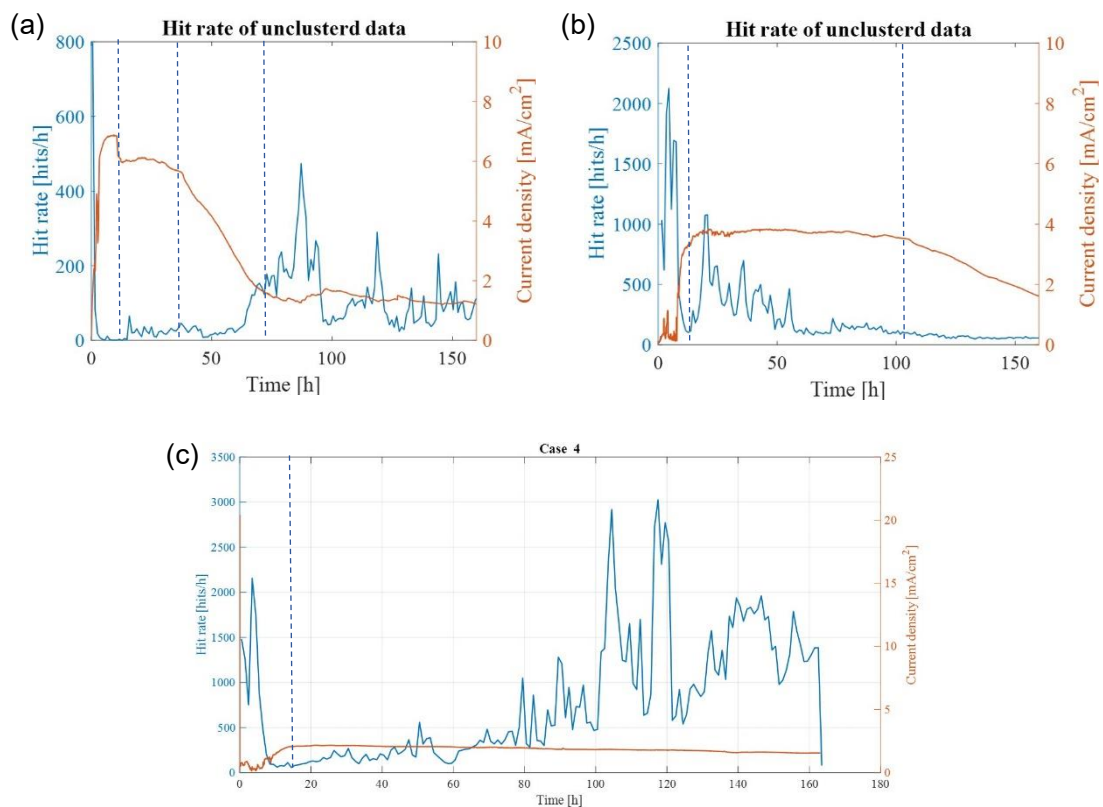
Figure 20 Schematic diagram of current density and hit rate of modified AE signals vs time for (a) Case 2; (b) Case 3; (c) Case 4

In order to analyze the source of the AE signal in more detail, a cluster analysis based on signal cross-correlation is introduced, shown in the appendix [102]. The similarity threshold is set as 0.3. Taking Case 2 as an example, all signals are divided into 50 clusters. Signals with similar waveforms and frequency distribution higher than 0.3 are grouped into the same cluster. Figure 21 shows the clustering results of Case 2 and the representative waveforms and frequency distributions of the three largest clusters. These three clusters are considered the most likely to contain corrosion information. The hit rate of each cluster is drawn separately to get Figure 22 (a). The same analysis steps are also applied to Cases 3 and 4 to obtain Figure 22 (b) and Figure 22 (c), respectively. In addition, daily observations are also introduced to trace better each cluster's signal source, which is listed in Table 7.
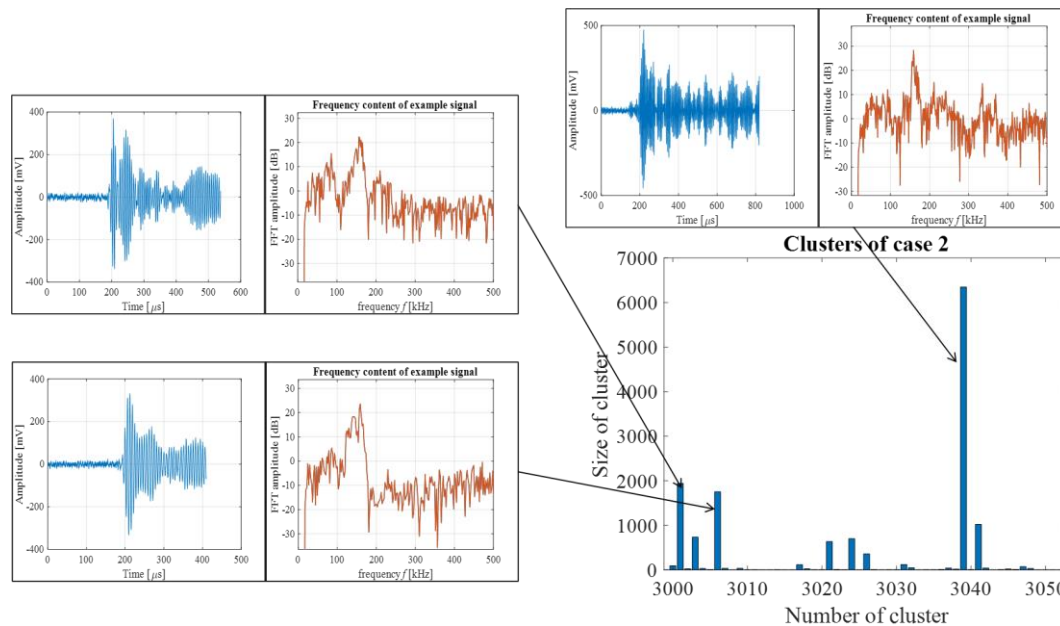
Figure 21 The clustering diagram of Case 2 and the representative signals of the three peaks with the largest number

For Case 2 [Figure 22 (a)], the hits are mainly concentrated in the stable corrosion stage. Cluster 3 starts from the 40th hour and maintains a very high hit rate. Combined with daily observations, this abnormal phenomenon is attributed to environmental noise. For about 40 hours, many corrosion rusts have accumulated at the bottom of the experimental beaker. The development and destruction of these rusts will also produce AE signals. As a result of the close location of the sensor, they are simpler to be collected. Therefore, many signals are generated during the middle and late stages of the corrosion process.

The signals of Cluster 1 and 2 continued the entire corrosion process. There are peaks within the first two hours. Afterwards, the signal disappeared until 20 hours. For 20-60 hours, the AE signals contain small fluctuations. This stage corresponds to the second and third stages of the corrosion process, which are the establishment and growth of the rust layer. After 60 hours, the AE signals are in more excellent activity, with several peaks appearing at the 79th, 85th, 120th, and 145th hour, respectively. According to the existing research in the literature, these signals (Cluster 1 and 2), which are almost active throughout the entire corrosion process, may be related to the evolution of hydrogen and the rupture of the rust layer [80]. However, daily observation finds that the overflow of bubbles occurred on the counter electrode instead of on the sample's surface. It is guessed that these processes occur inside the rust layer and cannot be observed from the outer side.

There are two reasons for making this assumption. First, among the sources that can generate AE signals during the corrosion process, signals related to bubble activity, such as bubble formation and collapse and release, are clearly distinguished from noise signals due to their higher frequency and amplitude [72, 76, 77]. It allows most of the signals to be preserved during noise filtering. Secondly, the long-term immersion experiments prove that a lot of pitting points occurred in the corrosion process of MC steel. The autocatalytic

process inside the pits can create a local acidic environment. Under acidic conditions, the cathodic reaction will change from oxygen decomposition to hydrogen evolution, resulting in hydrogen bubbles under the rust layer. These bubbles can collide with the pit walls or the rust layer on the top. They can also be released as the rust layer ruptures. All of these processes may produce AE signals with stronger frequencies. Therefore, it is more likely that the signals of Cluster 1 and 2 are related to the hydrogen bubble behavior.

In addition, there are some speculations about the composition of bubbles overflowing on the counter electrode. As the accelerated reaction progresses, a large amount of oxygen in the solution participates in the cathodic reaction on the counter electrode, thus being consumed. When the oxygen content is insufficient to meet the needs of the cathodic reaction, there may be hydrogen evolution to consume excess electrons on the counter electrode. In the three experiments, the appearance of bubbles on the counter electrode is a period after the beginning of the experiment. At the same time, the analysis of the potentiodynamic polarization results also gives the possibility of hydrogen precipitation in the cathodic reaction of MC steel in the NaCl solution. Therefore, this kind of speculation has a certain degree of feasibility.

If these possible signal sources and the results from long-term immersion experiments are used to explain the corrosion process, the peak at the 2nd hour will correspond to the beginning of the corrosion reaction. The passivation film rupture due to the attack of Cl$^-$ after its formation. The initial pitting points are generated on the surface. This process caused a large number of hits. In the subsequent stable corrosion stage, many rusts continued to be generated, and the number of hits is reduced. At 20-60 hours, the outer protective corrosion layer gradually builds up, and occluded pitting pits appear. However, the stability of the pit cover at this stage is poor, and it is more likely to rupture and open [73]. Therefore, the number of the AE signals related to hydrogen bubbles is lower. When entering the final stable corrosion stage (after 60 hours), the rust layer can restrict the exchange of internal and external substances. More occluded pitting pits are produced. The peak at this stage corresponds to the formation and evolution of many hydrogen bubbles occurring in the pits. The inactive phase may be related to the fact that the pits are entirely open. The acidic environment no longer exists. The formation of hydrogen bubbles is interrupted.

In Case 3 [Figure 22 (b)], since it has not entered a stable state with a lower corrosion rate, the hits on the initial corrosion stage dominate value. The main behaviors of the initial stage are the initiation of corrosion and the establishment of the rust layer on the sample surface, according to the result from long-term immersion experiments. Therefore, the signals may be related to these two processes. Comparing the signals of Clusters 1 and 2 in Case 2, all the signals of Case 3 showed a relatively longer duration and a higher hit rate in the initial phase. Therefore, new sources are included in addition to the signals related to bubble activity. Considering the dominant corrosion behavior at this stage, they are attributed to the continuous failure of the rust layer on the surface. The failure of the rust layer itself can lead to the generation of the AE signal [70]. Meanwhile, failure can cause hydrogen bubbles generated during pitting corrosion to burst within a narrow interval, thereby increasing the number of hydrogen bubble activity [78]. When entering the rust layer establishment stage, the formation velocity of the layer is equal to or greater than the

fracture speed. The bubble burst is no longer apparent. However, the available data are insufficient to distinguish the signal of rust layer failure itself from that of hydrogen bubbles. It is considered that the signal related to the cracking of the rust layer usually has a small amplitude [70]. In contrast, signals related to hydrogen bubble activity often exhibit higher frequencies (more than 125 kHz) and amplitudes (hundreds of microvolts) [70, 76, 77]. These two parameters, amplitude and frequency, can be introduced into the analysis in subsequent experiments to distinguish the detailed source of these signals.

Among the signals of Case 4 [Figure 22 (c)], Cluster 1, 2, and 4 showed extremely active signals between the 90th and 120th hours. Meanwhile, at the 120th hour, they showed the same bimodal structure. Combined with daily observation, after 90 hours, many rusts accumulated between the sensor and the sample. It introduces much environmental noise. The signals of these three clusters are more likely to be attributed to this type of noise. Cluster 5 has high activity in the first few hours of the initial stage of corrosion. This phenomenon is similar to the signal of Case 3. It should be related to the multiple bursts of bubbles caused by the continuous failure of the passivation film on the surface. For Cluster 3, it shows a large number of hits in the initial period and has an upward trend in the last dozens of hours (after the 130th). This signal may come from the evolution of hydrogen bubbles in the pits, similar to Cluster 1 and 2 in Case 2.

According to the existing data, the AE signals can be divided into two types during an accelerated corrosion process. In one type, the signals are mainly concentrated in the initiation stage and exhibit lower activity in the establishment stage. This type may be related to the bubble rupture caused by the continuous failure of the passivation film. The other type has strong signals in both the initiation and growth phase. It may be related to the evolution of hydrogen bubbles in the pits, including rupture, friction with the pit wall and pit cover. Jomdecha et al. classified the first type of signal as uniform corrosion and the second type as pitting corrosion [78]. Therefore, the corrosion process of MC steel is composed of uniform corrosion and pitting corrosion.
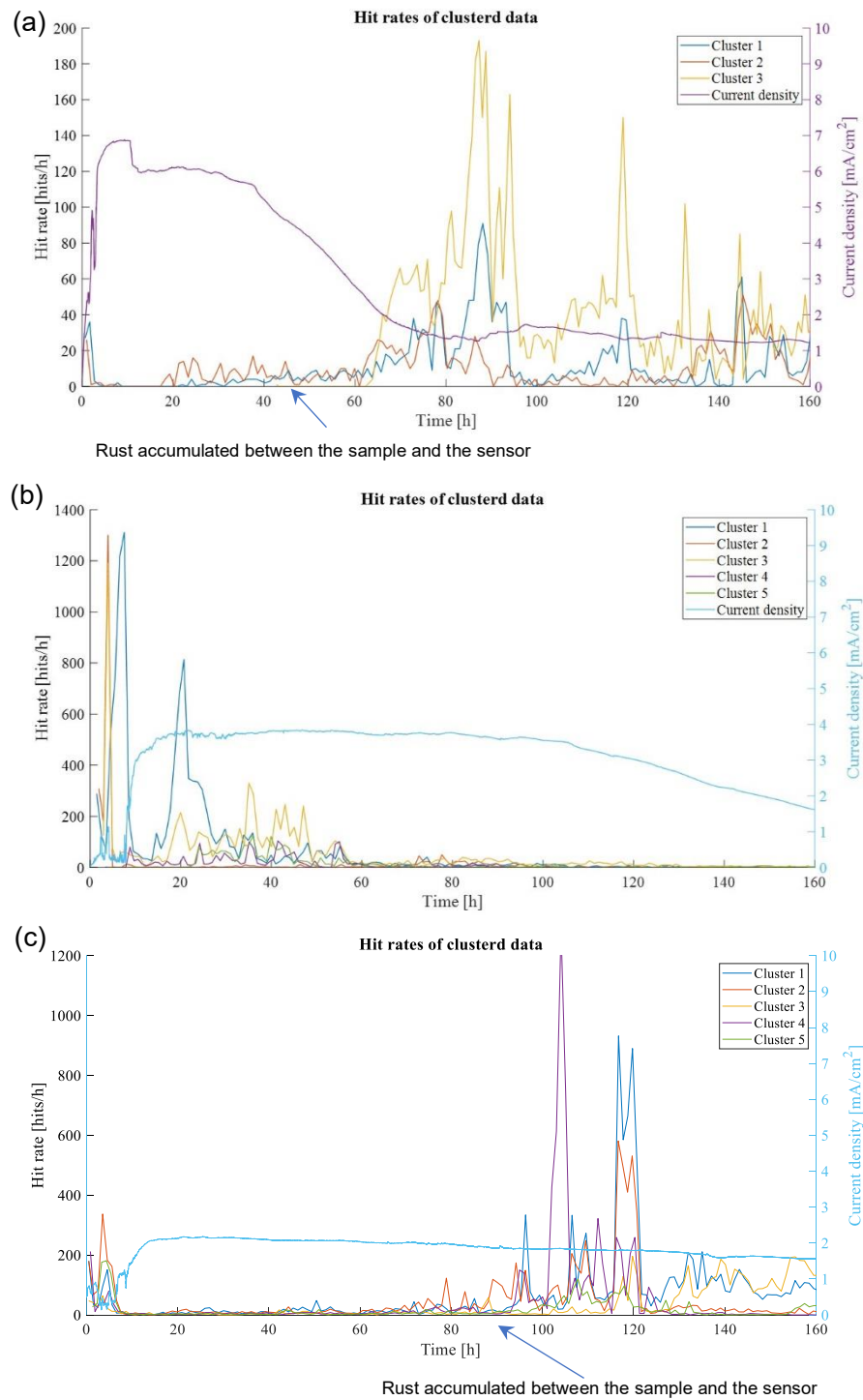
Figure 22 Schematic diagram of clustered hit rate of modified AE signals vs time for (a) Case 2; (b) Case 3; (c) Case 4

Table 7 Daily observation of Case 1-4 while accelerating the corrosion process

Time	Case 1	Case 2	Case 3	Case 4
0 h	Start monitoring			
19 h (Day 1)	The clear solution, orange rust accumulates on the surface of the sample	Brown solution, black rust accumulates on the surface of the sample, bubble generation on the counter electrode	Brown solution, black rust accumulates on the surface of the sample	Brown solution, black rust accumulates on the surface of the sample
43 h (Day 2)	The observation is the same as the previous day	The clear solution, rust deposited on the bottom of the beaker, rust column formed	Rust deposited on the bottom of the beaker, bubble generation on the counter electrode	Black solution Less bubble generation on the counter electrode
67 h (Day 3)	Rust begins to fall off the sample	The rate of bubble generation decreases, large bubbles accumulate on the surface	Rust column initial formed, clear solution, more bubbles generation	Rust column initial formed, clear solution, more bubbles generation
91 h (Day 4)	The observation is the same as the previous day	The observation is the same as the previous day	The observation is the same as the previous day	Rust accumulated between the sample and the sensor
160 h (Day 7)	The observation is the same as the previous day	The rust layer on the surface is hard, with a lot of pores and cavities	The rust layer on the surface is hard, with a lot of pores and cavities	The clear solution, rust accumulated at the bottom

5.3.2 Morphology analysis

The surface morphology of the sample in the natural corrosion state is shown in Figure 23. The two figures show the morphology of the rust layer on the same sample surface under different magnifications. The difference in their colors is caused by imaging under different objectives.

After 16 days of immersion, the rusts have covered the surface. The distribution of the rust

layer is uneven. It indicates that although the initial corrosion area will be different in size and shape (Figure 16), the corrosion area will gradually expand and cover the entire exposed area as the corrosion process progresses. However, the difference in initial time will cause a specific difference in the thickness of the rust layer. Figure 23 (b) shows the morphology of the rust layer at ×300 magnification. Consistent with long-term immersion, the rust layer also exhibits delamination. The outer orange rust layer can be divided into two parts according to thickness and morphology. The thicker part presents a loose outer layer structure, with a significant thickness difference between parts [as shown in Figure A. 4]. Such areas are randomly scattered on the surface. It is speculated that this may be the area where large pitting points are located. However, the experiments currently cannot remove the corroded layer at fixed points, so this phenomenon cannot be accurately explained. The morphology of most of the exposed area is similar to the thinner part in Figure 23 (b). They present a "cotton ball"-like structure, which is similar to the morphology at the later stage of long-term immersion. It represents that the introduction of the AE sensor will not affect the growth of the rust layer.
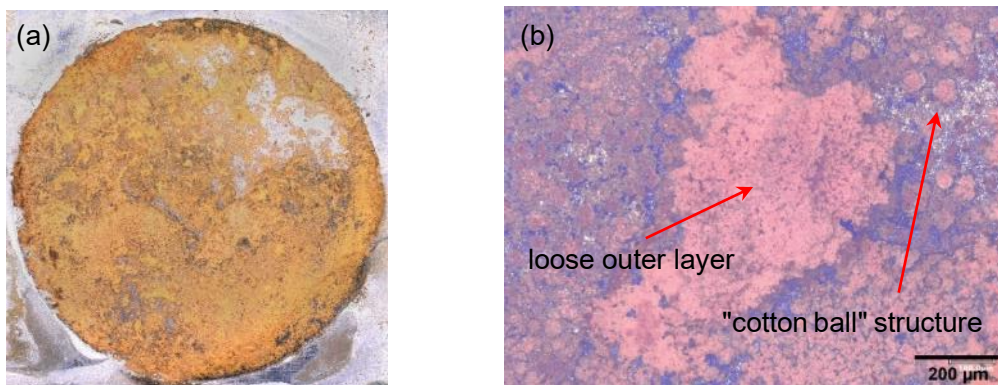

Figure 23 The morphology of MC steel in NaCl solution without accelerating potential (a) macrostructure; (b) microstructure at ×300 magnification

Under the two acceleration conditions, the morphology of the samples is relatively similar. Case 2 is used as a representation for analysis and discussion. Figure 24 (a) shows the morphology of the outermost rust layer of the sample. The rusts cover the whole exposed area. This layer bulges outwards, which is hard and brittle. Considering its hard texture, its composition may be a mixture of Fe (III) oxyhydroxide and oxide [100, 101]. Daily observations have revealed that large bubbles gather on the surface of the rust layer during the corrosion process. It indicates that the rust layer can prevent gas from entering. It is reasonable to speculate that it also has the effect of preventing internal corrosion products from spreading out by combining with the analysis of current density and AE signals. Therefore, after a long corrosion reaction, a protective corrosion layer can also be produced on the surface of MC steel.

When the outer layer is removed, the inner rust appears grey-black and quickly turns brown in the air. The rust layer in the natural corrosion process is denser and more closely linked in the matrix. It reflects in the increasing time of the ultrasonic water bath to remove all rusts on the surface. There are obvious cracks and small pits on the inner surface [Figure

24 (b)]. Similarly, the stage of crack generation cannot be determined. However, cracks always occur in areas where the rust layer has a loose morphology. Regarding the cause of the tiny pits, one speculation is that the rough rust layer morphology may be due to the more bottomless pitting pits on the matrix.

After the rust layer is thoroughly washed away, there are many pitting points on the matrix. Figure 24 (c) shows the microstructure of the pits with ×200 magnification. The color of the sample itself is silver, but at this magnification, the whole figure is bluish. After long-term acceleration, some corrosion pits no longer have regular round edges. Its shape is more like a combination of several circles [it is more evident in Figure A. 5 (a)]. Interestingly, some of the corrosion pits with larger diameters and depth also contain more minor pitting points [the area in the red box in both Figure 24 (c) and Figure A. 5(a)]. It represents that as the corrosion process progresses, some pits with a large diameter will be linked to each other and develop into a relatively flat area. In this new plane, there will be new pitting points occurred. It can be regarded as a process in which pitting corrosion and uniform corrosion coexist and develop mutually, which is consistent with the result that signals related to both uniform corrosion and pitting corrosion are present in the AE signal.
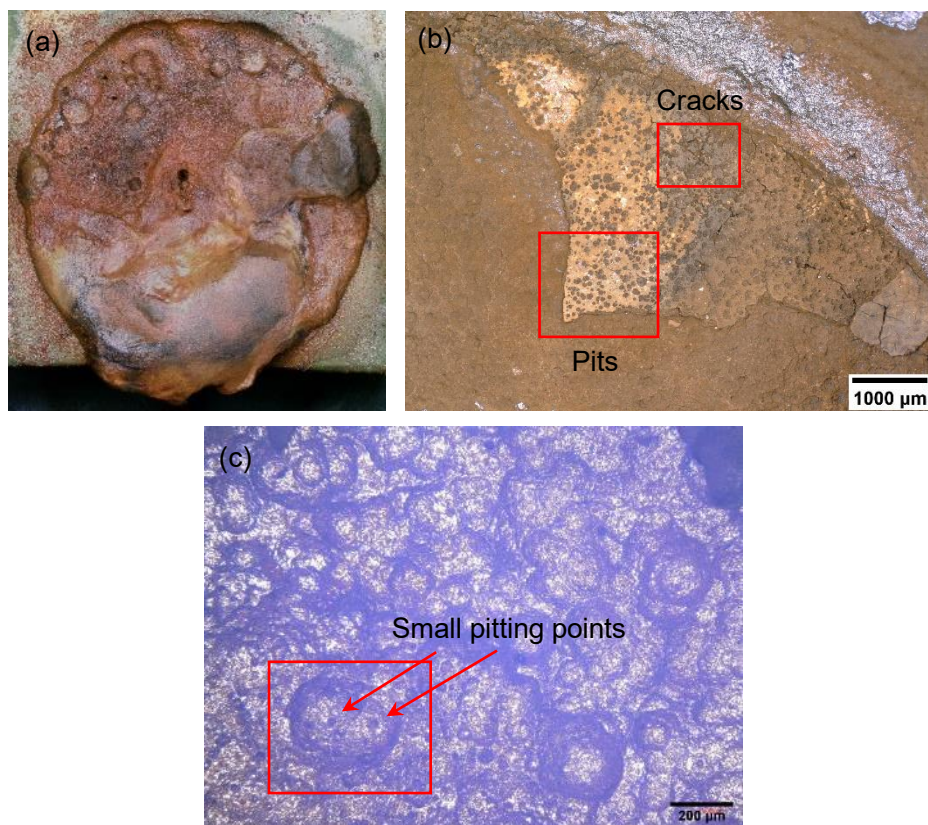
Figure 24 The morphology of MC steel in NaCl solution with accelerating potential (a) macrostructure of outer rust layer; (b) macrostructure of inner rust layer; (c) microstructure at ×200 magnification

For the sample of Case 4, although only the OCP is applied, the electrochemical results have indicated that the corrosion process is also accelerated to a certain extent. Similarly, the morphology of its rust layer [Figure 25 (a)] is different from that under natural conditions.

The rust completely covers the surface of the sample. The yellow outer corrosive material quickly cracks and fall off during the drying process, exposing the brown inner layer. Its morphology is similar to the inner corrosion layer of Case 2. The rust layer changes in morphology and has the same color change process as Case2. It is no longer accurate to estimate the composition of the rust layer by morphology and color. Therefore, it is not included in the discussion.

After the rust layer is removed, the pitting points on the matrix also show the same characteristics as in Figure 24 (c), with irregular shape [the area in the white box in both Figure 25 (b) and Figure A. 5 (b)] and some large pits containing small pits [the area in the red box in both Figure 25 (b) and Figure A. 5 (b)]. However, compared with Case 2, the size and number of these areas are relatively small. Therefore, this sample is in the initial stage of mutual development of pitting corrosion and uniform corrosion.
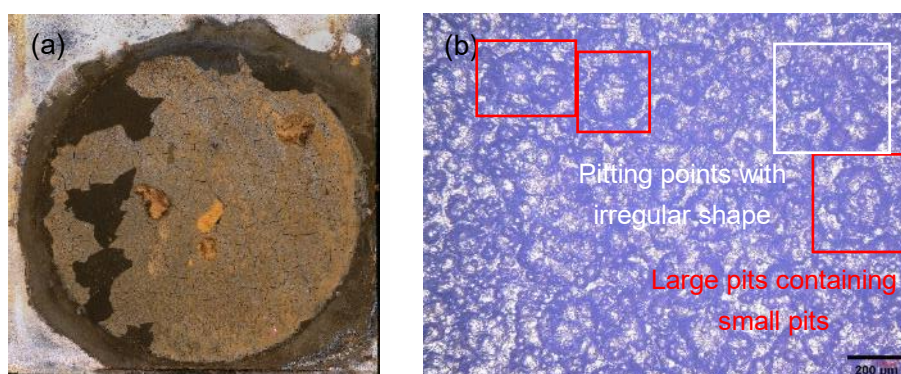

Figure 25 The morphology of MC steel in NaCl solution with OCP (a) macrostructure of rust layer; (b) microstructure at ×200 magnification without rust layer
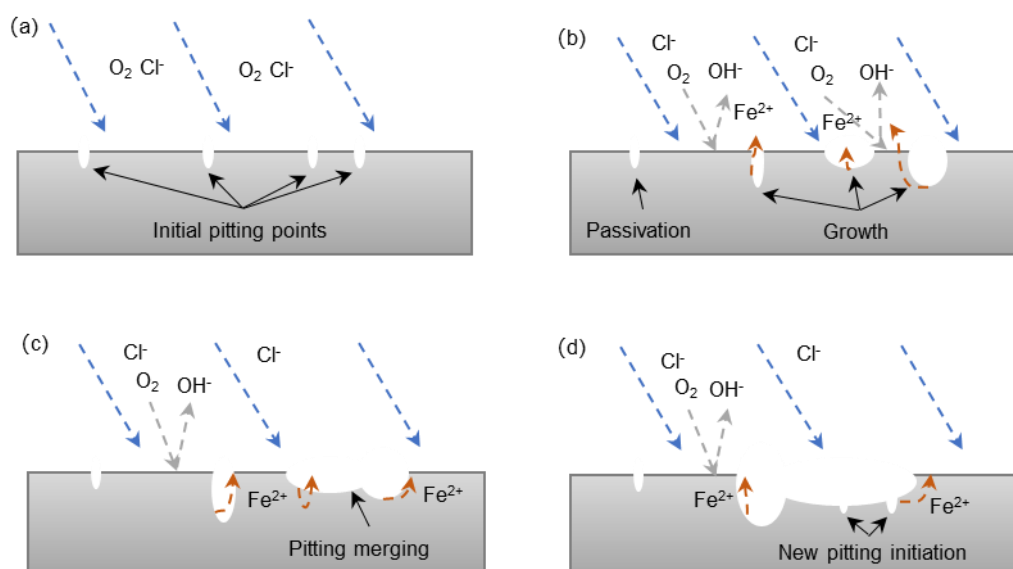

Figure 26 Schematic diagram of the corrosion process of the matrix of MC steel in NaCl solution from the cross-sectional view

Combined with the morphology and the height diagram of long-term immersion

experiments, the corrosion process of the matrix of MC steel in NaCl solution can be obtained. The silver rectangle represents the surface of the MC steel matrix from the cross-sectional view. Pitting corrosion is indicated by white pits. For better display, their size has been enlarged. The blue arrows represent the erosion of Cl-. The grey arrows represent the conversion reaction of O2. They are distributed on the entire surface. Here it only shows the trend. The orange arrow indicates that ferrous ions are generated in the corroded area. When the sample is in contact with the solution, an electrochemical reaction is likely to occur between the grain boundaries and grains. Because MC steel has a fine-grained microstructure, its surface has many grain boundaries. It will many pitting initial points after being attacked by Cl- in the solution, causing rapid initiation [Figure 26 (a)]. Some initial points become passivated and no longer participate in the reaction soon after initiation. Such metastable pits have almost no depth [Figure 17 (a)]. Other pitting points will grow to develop into stable pits [Figure 26 (b)]. The metal around the pores dissolves in the reaction to generate anodic ions, causing anions (Cl-, OH-) to transfer from the electrolyte to the anodic site. O_2 will participate in the cathodic reaction to generate OH-, which meets with ferrous ions to form rusts. These rusts will accumulate and gradually cover the surface (Figure 19). Some corrosion pits are subject to autocatalysis and grow mainly vertically. Others will be affected by the horizontal migration of surface anions (Cl-, OH-) and mainly expand horizontally. Pitting points dominated by horizontal growth will contact each other to form a new plane, which develops into uniform corrosion [Figure 25 (b), Figure 26 (c)]. On the new plane, there are also initiation, passivation, and growth of corrosion pits [Figure 24 (c), Figure 26 (d)]. Uniform corrosion and pitting corrosion are transformed into each other, which constitute the corrosion process of MC steel. This process is consistent with the experimental results of Yang et al. and Wang et al. [103, 104].

5.4 The influence of environmental factors on the corrosion process of MC steel

In the previous discussion, flow velocity and temperature proved to be two critical environmental factors that may affect the corrosion process in the offshore marine environment. Some experiments have been introduced to explore the influence of these two environmental factors on MC steel. Regarding the characterization of the corrosion process, the design is consistent with the long-term immersion experiments. Considering the continuity of the experimental data, the electrochemical data (E_{OCP}, Rp) shown in the discussion are the most representative results of the three repeated experiments. The corrosion rate results are taken from the average of three experiments.

5.4.1 Flow velocity

5.4.1.1 Electrochemical analysis

The evolution of the E_{OCP} of MC steel at different flow velocities in NaCl solution (Figure 27) will be discussed first. Similarly, data recording starts after the potential change rate is less than 0.1 V/h. In general, it remains negative potentials under all conditions. The potential drops rapidly but gradually stabilize at the beginning of immersing. The rapid initial corrosion process is caused by the combination of Cl^- ions and flowing water. Many ions will attack the active spots (grain boundaries) on the surface, leading to the initiation of corrosion. The impact of flowing water is multiple. On the one hand, flowing water can cause more oxygen to reach the sample surface. In this way, the corrosion process will not be limited by the oxygen concentration near the surface. The cathodic corrosion rate can stay at a high level for a longer time [105, 106]. On the other hand, it will remove the rusts produced during the corrosion process, re-exposing the metal matrix to the corrosive environment. Meanwhile, the impact of the flowing water on the surface will also cause mechanical damage to the matrix to accelerate its dissolution [107]. Combining the influence of these processes, flow velocity accelerates the corrosion of the metal [28]. As the corrosion progressed, the surface's corrosion process gradually stabilized, and the E_{OCP} value no longer changed significantly. However, with the presence of flow velocity, it takes about 6 hours for the E_{OCP} of the samples to stabilize. Under static conditions, it is about 4 hours. With the destruction of flowing water, a thicker rust layer is required to be formed to resist the damage [108]. Therefore, the time for the sample surface to stabilize is prolonged.
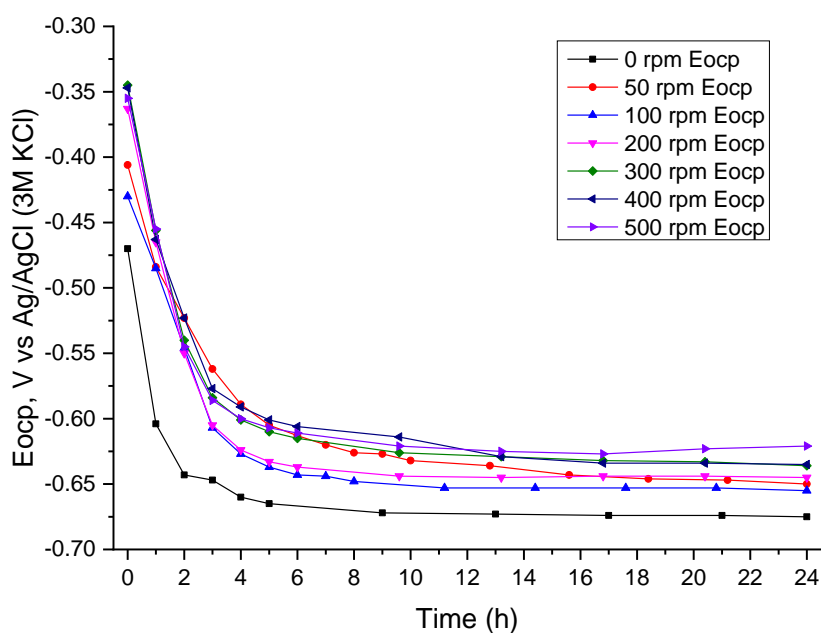

Figure 27 Evolutions of E_{OCP} of MC steel in 3.5 wt.% NaCl solution at different flow velocities

At the same time, in the entire detection process, as the flow velocity increases, a higher potential is obtained. It means that the surface becomes passive. The highest potential is observed at 500 rpm condition, which is -0.621 V [Ag/AgCl (3M KCl)]. The most active point is observed under static conditions shown -0.675 V [Ag/AgCl (3M KCl)] value. Previous studies have pointed out that most metals establish a layer on the surface in the form of a passivation film or corrosion product in a corrosive environment [108, 109]. In this experiment, the rust layer formed by the corrosion reaction has a specific protective ability, reflected in the previous paragraph. As the flow velocity increases, the rust layer's protective ability increases, which make the surface more inert, resulting in higher E_{OCP}.
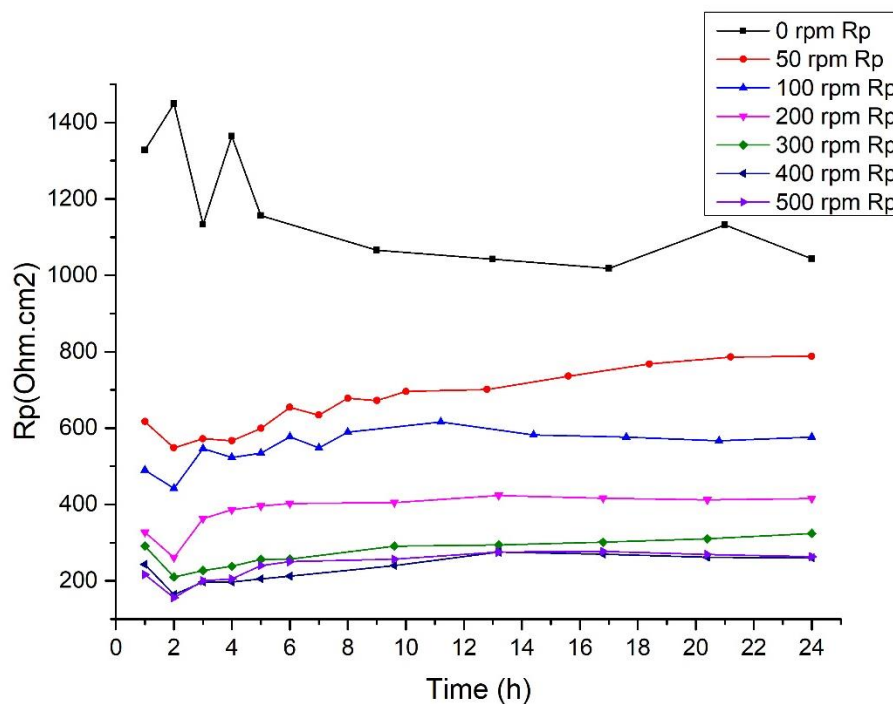

Figure 28 Time dependence of Rp for MC steel in 3.5 wt.% NaCl solution at different flow velocities

After obtaining a relatively stable E_{OCP} value, the Rp of the sample is measured. The evolution of the Rp of MC steel with time at different flow velocities is shown in Figure 28. The value of Rp fluctuates during the first few hours and then gradually stabilizes. Compared with static conditions, as the flow velocity increases, Rp decreases significantly, from 1043 Ohm.cm^2 (0 rpm) to 269 Ohm.cm^2 (500 rpm), with a decrease of about 75%. It indicates that the flow velocity accelerates the corrosion process on the sample surface, resulting in lower resistance to corrosion.

By selecting the Rp value at the 24th hour under each flow velocity condition, Figure 29 is obtained. The results are non-linearly fitted. The R-square value of the fitted curve is 0.997, which proves that it has an excellent correlation with the data. At the end of the experiments, all of the samples have reached an almost stable statement. At higher velocity conditions, the decreasing trend of Rp gradually decreases. The value of Rp at 400 rpm and 500 rpm are consistent. Since Rp is inversely proportional to the corrosion rate, it can also prove

that the corrosion rate increases with the flow velocity, but after a certain point, the corrosion rate will no longer be affected by the water flow. It is consistent with the changing trend of carbon steel corrosion rate with flow velocity in the literature [28]. However, due to the limitation of the experiments and time, the critical velocity cannot be accurately obtained in this project. To obtain accurate critical velocity and platform period, more experimental data at high-velocity are needed to modify the analysis.
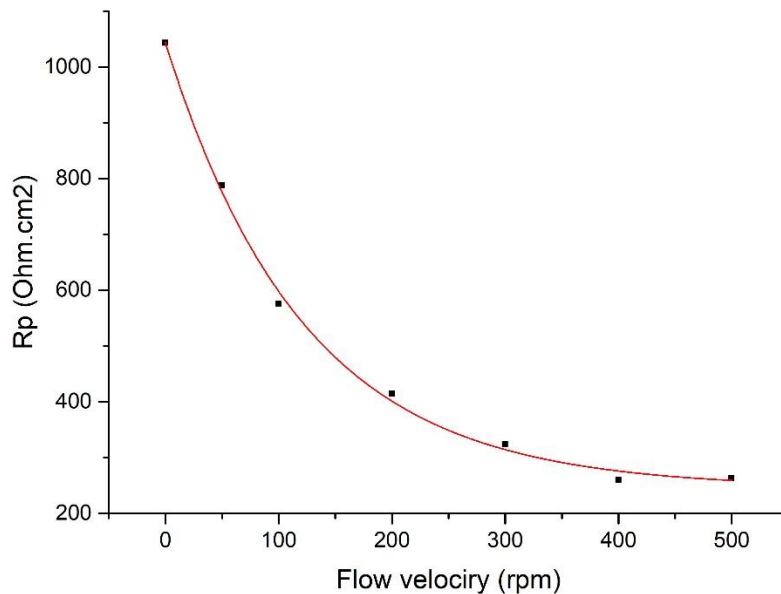

Figure 29 The evolution of finial Rp at different flow velocities

Existing experiments attribute the occurrence of this critical velocity to two reasons. One analysis is that the increase in flow velocity increases the oxygen transfer process at low flow velocity. Thus, the cathodic reaction controls the intensity of corrosion. At a high flow velocity, although higher flow velocity allows more oxygen to be transported to the electrode surface, it also makes the rust layer more protective. The rust layer can protect the matrix from contacting the Cl^- ions in the solution, causing the rate of metal dissolution to no longer change. The corrosion process is transformed from cathodic control to anodic control, leading to no longer changing the corrosion rate [110]. Another reason is that when the flow velocity exceeds the critical value, the denseness of the rust layer becomes poor [107]. Its structure is porous with thinner thickness [106, 111]. It is easier for high-speed fluid to penetrate it to reach the metal surface. Sufficient kinetic energy will interfere with the growth of metastable pitting corrosion, thereby hindering the rise of corrosion rate [111]. This phenomenon is especially noticeable in environments where tiny particles are present [107]. If the presence of the critical velocity is due to the second reason, the sample matrix will show a rougher surface [106]. It is not observed in the morphology. Therefore, a more reasonable guess should be the first one.

In addition, as the immersion time prolonged, Rp showed a downward trend under static conditions. In the flow velocity experiment, the final Rp stabilizes at a higher value than the initial resistance. It proves that the flowing water promotes the formation of a more protective rust layer on the surface. However, this effect is feeble, and it cannot offset the

substantial damage to the surface caused by the flowing water. Therefore, the corrosion resistance of the surface can only be increased in a small range.
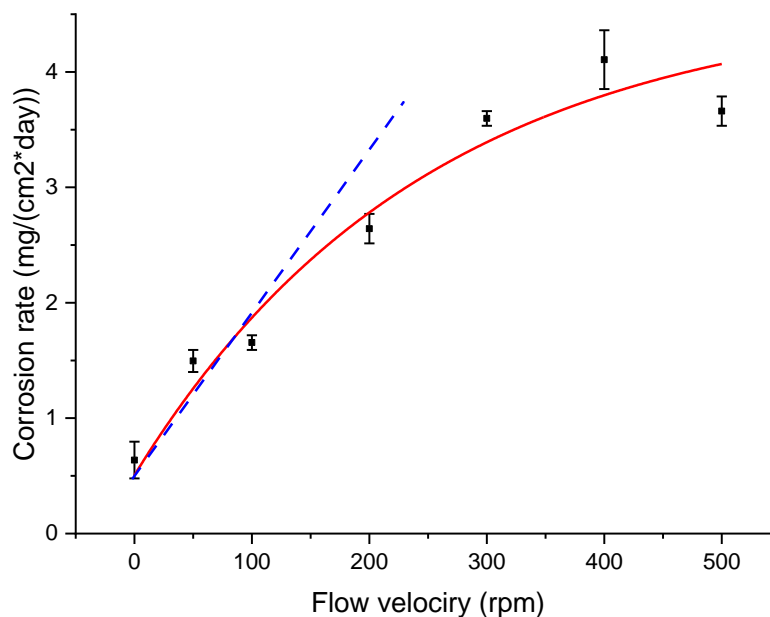

Figure 30 Corrosion rate of MC steel in 3.5 wt.% NaCl solution at different flow velocities

By analyzing the data on weight loss, a schematic diagram of the corrosion rate changing with the flow velocity (Figure 30) is obtained. The data in the figure come from the average of three experiments. Error bars show the standard deviation of three data. The results adopt non-linear fitting. The R-square value of the fitted curve is 0.926, which proves that it has a good correlation with the data.

As the flow velocity increases, the corrosion rate shows an upward trend. Meanwhile, the ascent rate gradually slows down. This is consistent with the changing trend of Rp (Figure 29). Under static conditions, the corrosion rate is 0.6 mg/(cm^2*day). At 500 rpm, the corrosion rate is 4 mg/(cm^2*day). It has increased by about five times, which indicates that the flow rate significantly increases the corrosion rate of the sample.

In the previous paragraph, the non-linear change is attributed to the transformation from cathodic control to anodic control. Some methods have been introduced to find the critical point of this transition. Melchers has pointed out that corrosion rate is linearly related to oxygen content [22]. Suppose the flowing water accelerates the corrosion rate by increasing the oxygen content on the reaction surface at low velocity. In that case, the corrosion rate in this area will be linearly related to the velocity. Therefore, a blue dashed line extends from the fitted curve at low flow velocity. The fitted curve in the velocity range of 0-100 rpm coincides with the dotted line. It begins to bend after the velocity is greater than 100 rpm. Therefore, the critical velocity for the start of the transition is 100 rpm. The corrosion rate will no longer change if the corrosion reaction is entirely controlled by the anodic reaction at high flow velocity. However, this area is not reflected in the fitted curve. Therefore, the critical point of anodic reaction control cannot be found in the existing data. Therefore, when the flow velocity is less than 100 rpm, the increase in the flow velocity

promotes the process of oxygen transmission to the reaction surface. More oxygen participates in the cathodic reaction, thereby increasing the corrosion rate. At this stage, the cathodic reaction controls the intensity of corrosion. When the flow velocity is greater than 100 rpm, the oxygen concentration on the reaction surface gradually exceeds the required corrosion process. The slower anodic reaction begins to limit the corrosion rate. Under the experimental conditions, no area is found where the corrosion rate is completely controlled by the anodic reaction to reach a plateau. A more comprehensive velocity range or longer experiment time needs to be introduced to judge this critical point better. Electrochemical results represent that higher flow velocity leads to a higher corrosion rate, but this effect will not increase after reaching a specific value. In addition, the presence of flowing water will make the rust layer more protective, enhancing the resistance of the sample to the corrosive environment.

5.4.1.2 Morphology analysis

The macroscopic appearances of the exposed area at different flow velocities are shown in Figure 31. In these figures, the water flows from the left to the right. Unlike long-term immersed surfaces with flowing water, the rust layer is distributed horizontally. This preliminary proves that flowing water significantly influences the expansion direction of the corrosion area. There is no uncorroded area. Although the area covered by the rust layer has different shapes, the area exceeds 50% of the surface.

The rust layer appears orange. The color deepens as the flow velocity increases, indicating that the thickness increases. At the same time, the direction of product accumulation is more precise. Interestingly, by observing the surface microstructure and film thickness, the thickness of the rust layer on the left side of the figure, which is the initial point of the water flow, is thicker than that on the right side. This difference appears for the first time under the condition of 100 rpm. As the velocity increases, the gap increases, from 19 μm (100 rpm) to 48 μm (500 rpm). In order to correspond to the division of corroded areas of the long-term immersion sample, the area containing the original surface and independent minor corrosion points is divided into i) the low-corrosion area. The area covered by a continuous large-area rust layer is ii) the rust layer covered area [as shown in Figure 31 (c)].

Considering the difference in the thickness of the rust layer, the exposed area is roughly divided into three parts with the left, middle, and right. Then three points are randomly selected from each part for detection. Finally, the average value of these data is taken to represent the thickness of the rust layer on the surface of the sample under this condition. This data selection leads to a larger margin of error, as shown by the error bars in Figure 32, which is the standard deviation of each average value. The range of the error bar increases with the increase of flow velocity. It also indicates that high-velocity flowing water will cause an apparent directional accumulation of rusts, resulting in uneven distribution.
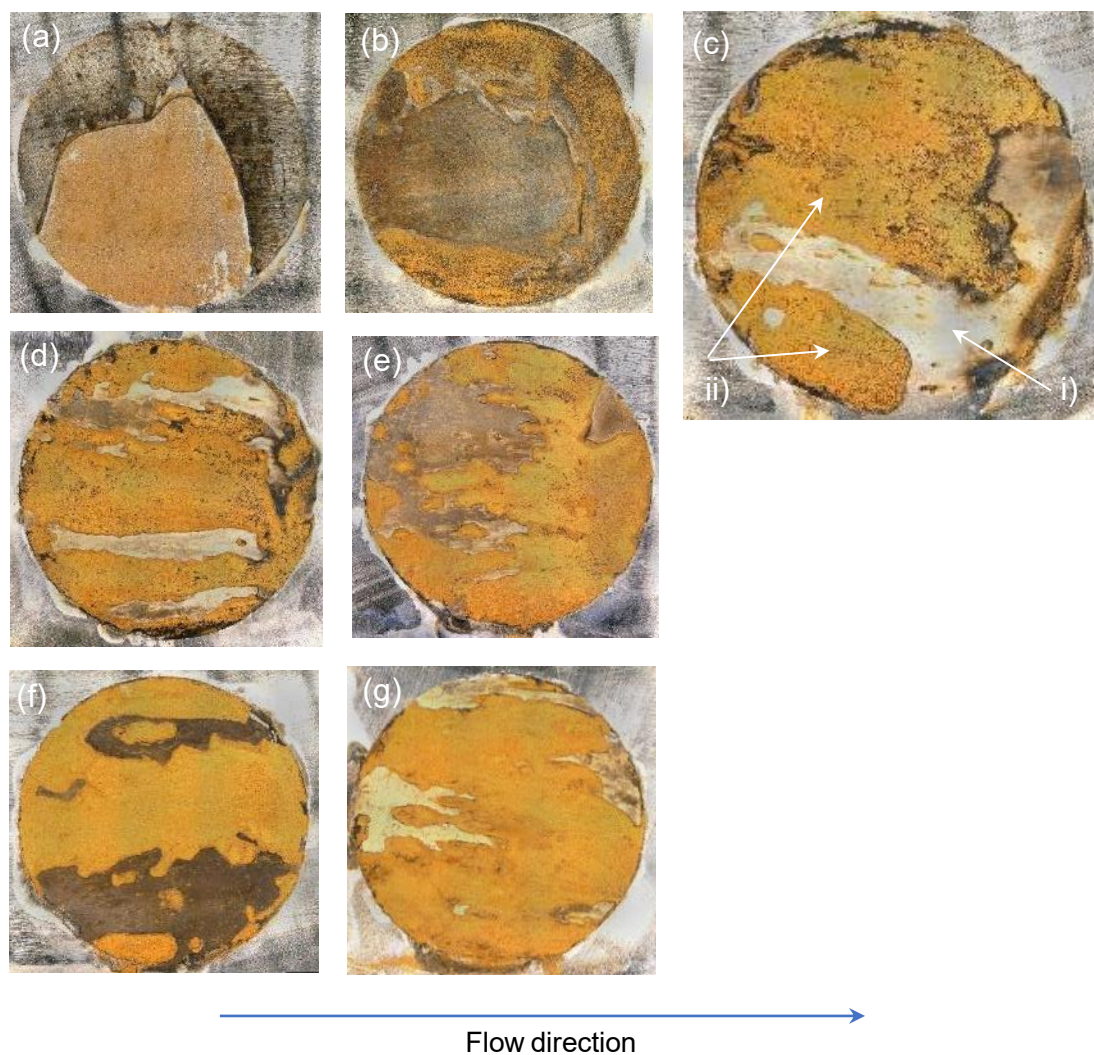
Figure 31 The evolution of the macro morphology of MC steel in NaCl solution with different flow velocity: (a) 0 rpm; (b) 50 rpm; (c) 100 rpm; (d) 200 rpm; (e) 300 rpm; (f) 400 rpm; (g) 500 rpm

Figure 32 represents that the corrosion layer becomes thicker as the flow velocity increases. The obtained data can be approximated fit into a straight line. The R-square value of the fitted curve is 0.900, which proves that the fitted line has a good correlation with the data. When the flow velocity rises from 0 rpm to 500 rpm, the thickness grows from 22 μm to 80 μm, which is nearly increased by nearly 3 times. It indicates that the flow velocity significantly promotes the growth of the rust layer in thickness. Unlike electrochemical parameters, even at a higher velocity, the thickness is still proportional to the flow velocity.
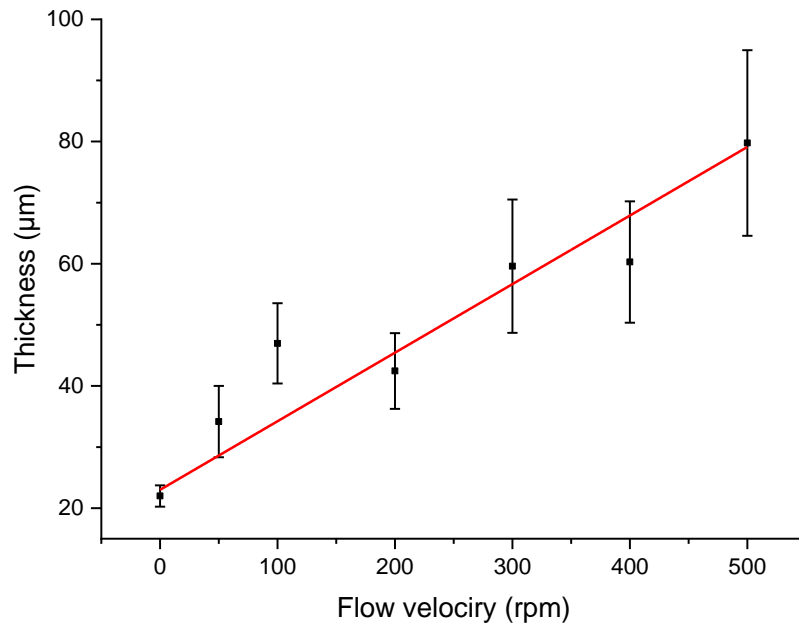
Figure 32 The thickness of the rust layer of MC steel in 3.5 wt.% NaCl solution at different flow velocities
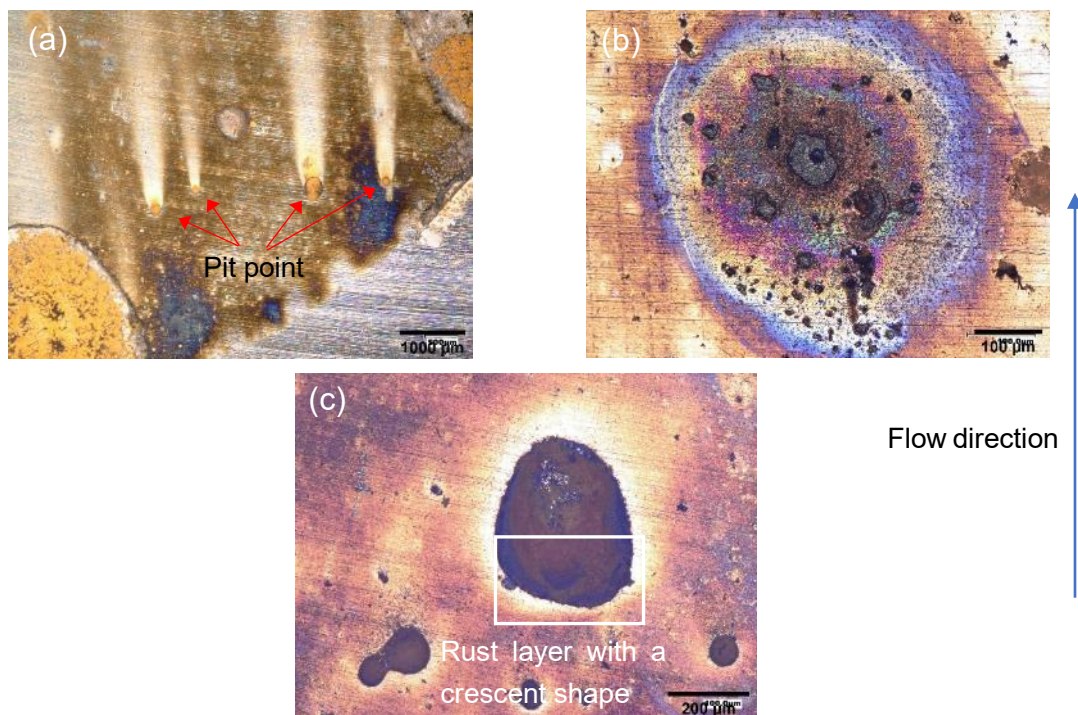
Figure 33 The morphology of low-corrosion area of the sample with (a), (b) 50 rpm; (d) 100 rpm flow velocity (water flows from bottom to top)

Some representative areas are selected to reflect the microscopic morphology of the sample surface (Figure 33). The color difference in the three figures mainly comes from the imaging difference caused by the magnification and the objective lens used.

Low-corrosion areas are dominated by meteor-shaped pits [Figure 33 (a)]. However, unlike

long-term immersion conditions, the pitting points are covered by rusts and mainly present as Figure 33 (c). The rusts accumulate at the point, which is the beginning of the water flow [the white frame in Figure 33 (d) and Figure A. 6], showing a crescent shape. The average thickness of these rusts is 57 µm. The thicker rust layer hinders the erosion by flowing water to the surface which is back to it. Therefore, a white area behind each point has a slower corrosion process than the surrounding area. Figure 33 (b) shows the morphology of the pitting matrix after the corrosion layer is removed. A relatively regular-shaped pit is in the center. It is surrounded by pitting points with different shapes to form a small corroded area. Unlike the metastable pitting point at the low-corrosion zone during long-term immersion, they develop into stable pitting under the acceleration of flowing water. It is reasonable to speculate that after a long enough time, the area of these pits will gradually expand and finally connect with the other corroded area.
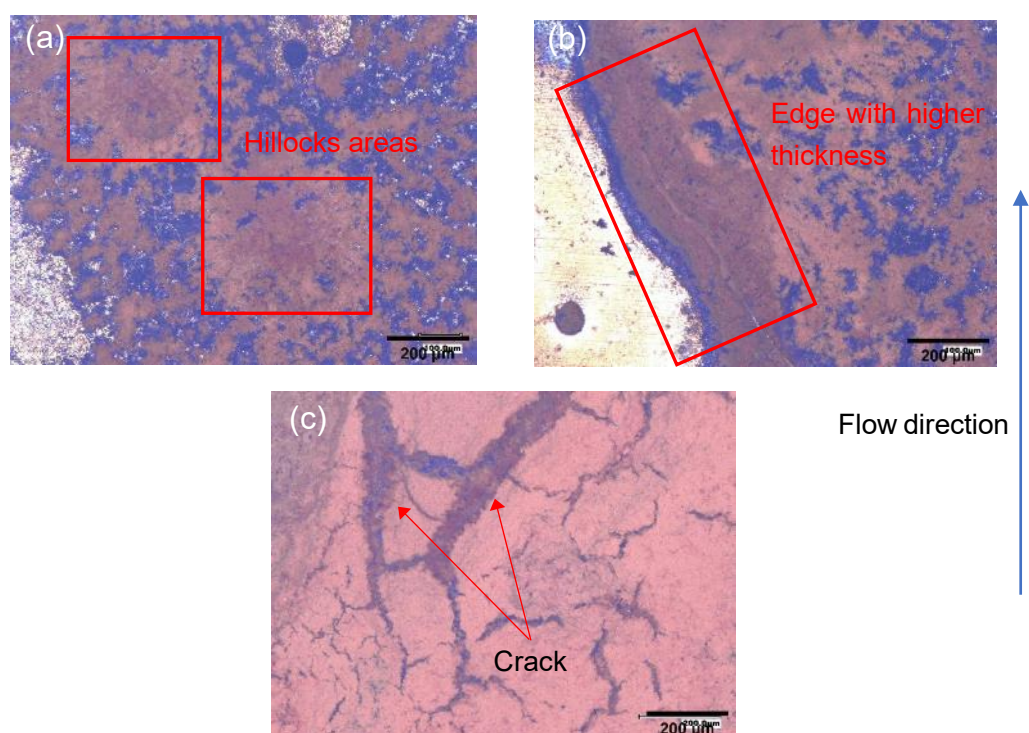

Figure 34 The morphology of rust layer of the sample with (a) 50 rpm; (b) 100 rpm; (c) 500 rpm flow velocity (water flows from bottom to top)

Figure 34 contains the microstructure of the rust layer on the sample's surface under three different conditions. The rust layer can be divided into a dark grey inner layer and an orange outer layer in all figures. With the flow velocity of 50 rpm, the morphology of the rust layer is more similar to Figure 19 (c) which immersion time is 7 days. The black-grey inner layer is continuous. The orangey-brown upper layer is flat and distributed in blocks. Meanwhile, with the presence of flowing water, some hillocks begin to form on the surface of the corrosion layer [the red frame area in Figure 34 (a) and

Figure A. 7 (a)]. These hillocks are the points with the severe corrosion process, which may be related to pitting corrosion. In the later stage of the formation process of pitting corrosion, many rusts will accumulate on the surface of the pit to form a cover. The cover hinders the

spread of substances in the pit, which leads to a local acidic environment. Such an environment will introduce an autocatalytic process. This process will cause a faster local corrosion rate to produce more rusts, resulting in thicker accumulation areas.

Starting from 100 rpm, the boundary between the low-corrosion zone and the corrosion layer becomes more and more distinct. It is mainly attributed to the higher rust layer at the edge of the rust covered area [the red frame area in Figure 34 (b) and Figure A. 7 (b)]. Taking the 100 rpm condition as an example, the average thickness of the corrosion layer is 47 ± 7 μm, and the thickness of the corrosion layer at the edge in Figure 34 (b) is about 100 μm. This thickness is much higher than the internal average value, more like a city wall. Although it restricts the internal products from spreading further outwards, the wall helps the rust layer avoid the damage of flowing water. It also explains why the accumulation of products is directional. The location close to the boundary (usually the point from which the flowing water starts) is better protected by high wall. Under the same growth conditions, these locations are less damaged. Therefore, more rusts can accumulate at this location. The thickness becomes greater.

Meanwhile, starting from 100 rpm, the morphology of the rust layer began to shape as "cotton balls", This morphology is usually attributed to the presence of goethite (α-FeOOH) [99, 112]. The shape may be due to the wall shear stress caused by the flow velocity promoting the growth of the corrosion products in a rounder shape. Its growth method is more like the accumulation of small balls. It achieves a rapid increase in thickness and produces more defects and holes in the outer layer.

As the flow velocity increases, cracks begin to be formed on the outer rust layer. At 500 rpm, cracks became more noticeable [Figure 34 (c)]. Existing detection results cannot determine whether these cracks are caused by flowing water during the immersion or by force during the cleaning and drying process before the morphology observation. However, these cracks can prove that the outermost rust layer has a loose structure. It will quickly break when it is stressed. Through the cracks, the middle layer of corrosion products accumulated in spherical shape can also be observed. Therefore, although the thickness of the rust layer increases significantly at high flow velocity, it is mainly a loosely structured outer layer. This layer is easily damaged with poor adhesion to the matrix, which does not enhance the rust layer's protective effect. It is similar to the observation of Li et al. [110].

In general, the flowing water affects the way that the rusts accumulate. From the distribution point of view, the direction of rust accumulation is parallel to water flow. The area where the flowing water starts has a greater thickness. For microscopic morphology, the corrosion products accumulate in small balls, which leads to a faster thickness growth rate and a looser outer layer structure.

5.4.2 Temperature effect

5.4.2.1 Electrochemical analysis

The changing trend of the E_{OCP} value in NaCl solution at different temperatures is depicted in Figure 35. In order to ensure that the different influences the change of E_{OCP} in

temperature, the electrochemical detection starts 10 minutes after the sample is immersed in a solution with a certain temperature.
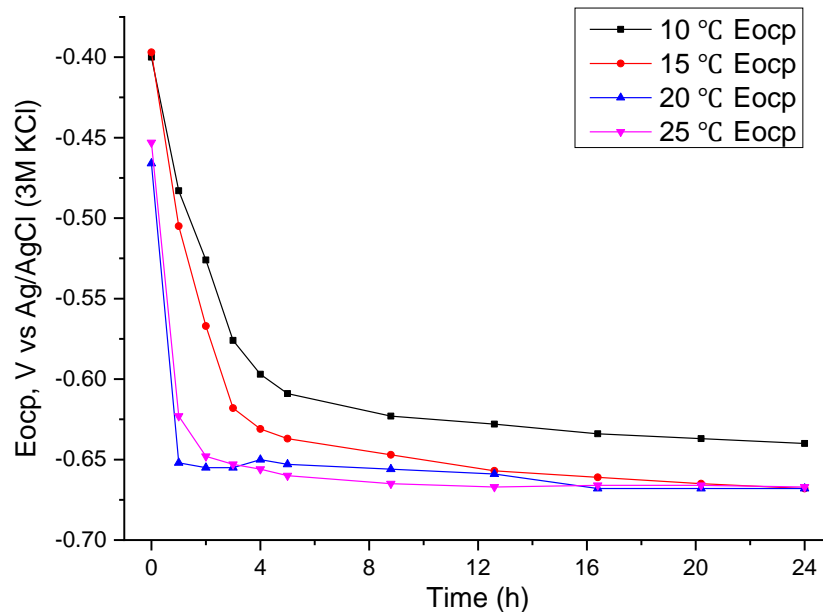

Figure 35 Evolutions of E_{OCP} of MC steel in 3.5 wt.% NaCl solution at different temperature

Similar to the corrosion process of long-term immersion and flow velocity, the potential drops rapidly at the beginning and gradually stabilize in all conditions. In addition, as the temperature increases, the time for the sample to reach equilibrium becomes shorter. When the temperature of the solution is grown from 10 °C to 25 °C, it changes from 5 hours to 1 hour for the sample to reach a relatively stable state. Theoretically, an increase in temperature will increase the energy of the system, making it easier to cross the activation energy to initiate the reaction [22, 25]. Therefore, a rapid initiation will be obtained at the higher temperature. At the same time, high temperatures can promote ion movement. On the one hand, this can promote oxygen diffusion in the solution [29]. The oxygen on the reaction surface increases, leading to an increase in the cathodic reaction rate. On the other hand, the temperature can promote the movement of ferrous ions. The ions generated by the anodic reaction will leave the reaction surface. The product concentration decreases will increase the anodic reaction rate. Therefore, when the temperature of the solution increases, both the cathodic and anodic reactions are accelerated [113]. It means that more rusts can be produced in a shorter time. Suppose the temperature changes do not have a greater impact on the damage of the rust layer. In that case, In that case, a faster formation rate and a constant rate of destruction will significantly reduce the time for the surface to reach an equilibrium state.

Meanwhile, a lower temperature always results in a higher potential during the entire detection process, which means a more inert surface. From the discussion in the previous paragraph, a lower temperature will cause the corrosion reaction hard to initiate, resulting in a more inactive surface. However, at the end of the experiment, the E_{OCP} of the samples immersed in the solution at 15, 20, and 25 °C tended to be consistent, which are -0.668 V [Ag/AgCl (3M KCl)]. This abnormal phenomenon may be due to the short immersion time

selected in the experiment. The long-term influence of temperature on the E_{OCP} has not yet been revealed during this short time.
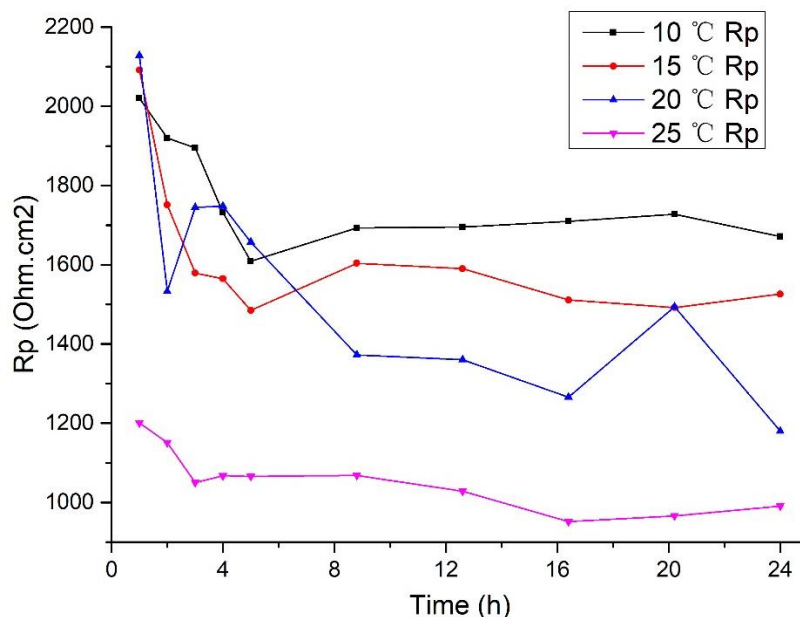
Figure 36 Time dependence of Rp for MC steel in 3.5 wt.% NaCl solution at different temperature

The evolution of Rp with time for MC steel in different solution temperatures is represented in Figure 36. Under all detection conditions, Rp first drops rapidly and then fluctuates around a lower value. The effect of temperature on Rp is clear almost from the beginning of the experiment. When the temperature rises from 10 °C to 25 °C, the initial Rp value drops from 2021 Ohm.cm^2 to 1201 Ohm.cm^2, with a 40% reduction. Plotting the final Rp value against temperature can get Figure 37. It also indicates that Rp has a clear downward trend as the temperature increases.
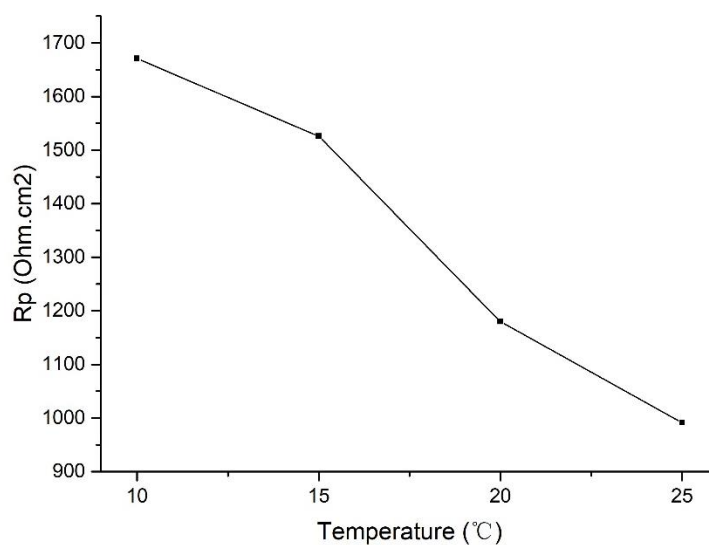
Figure 37 The evolution of finial Rp at different temperature

A schematic diagram of the corrosion rate with temperature is shown in Figure 38. These data are from the average of three repeated experiments. Under all conditions, the data's error range (standard deviation) is less than 10%.

The corrosion rate runs an almost linear upward trend with the temperature increasing. It is consistent with the changing trend of the corrosion rate inferred from the Rp curve (Figure 37). At 10 °C, the corrosion rate is 0.37 ± 0.02 mg/(cm^2*day). When the temperature rises to 25 °C, the corrosion rate goes to 0.67 ± 0.03 mg/(cm^2*day). It is increased by approximately 80%. This growth trend is approximate to the value of carbon steel in the literature [29].
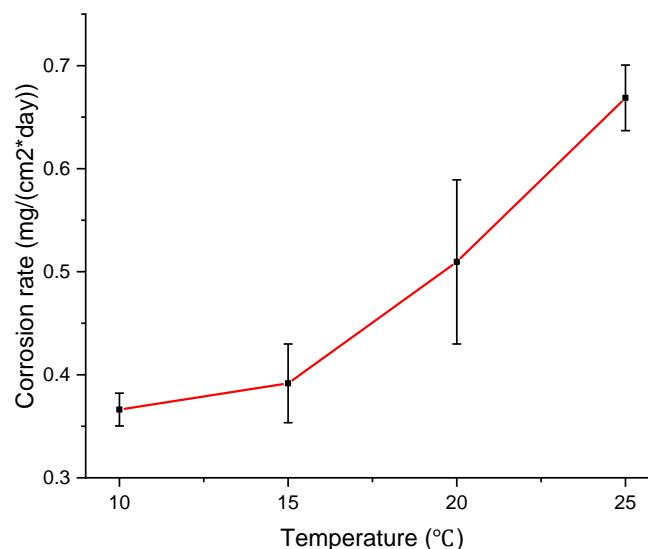

Figure 38 Corrosion rate of MC steel in 3.5 wt.% NaCl solution at different temperature

In conclusion, the samples in these experiments are in the initial stage of the corrosion process. In this stage, the higher temperature leads to the rapid initiation of the reaction by increasing the system's energy to cross the activation energy. At the same time, it promotes the movement of molecules. It increases in the corrosion rate. Under the experimental conditions, when the temperature increases by 15 ℃, the corrosion rate can nearly double.

5.4.2.2 Morphology analysis

The macroscopic corrosion morphologies of the exposed area at four different temperatures are contained in Figure 39. Only the corrosion area of the 10 ℃ sample is concentrated on the upper part of the sample. Due to the significant difference between 10 °C and room temperature (approximately 22 °C), there is a gradient of solution temperature near the liquid surface. It results in a temperature gap of approximately 0.4°C from the bottom to the top of the exposed area. Therefore, corrosion first occurs in the upper part where the higher temperature. Compared with the samples in long-term immersion experiments, there are many black dots in the rust covered area. When the temperature increases, the color of the rust layer gradually deepens, and the black spots disappear. These black spots are the accumulation areas of pitting points. Figure 40 (a)

and Figure A. 8 (a) shows their microstructure and the height difference figure.
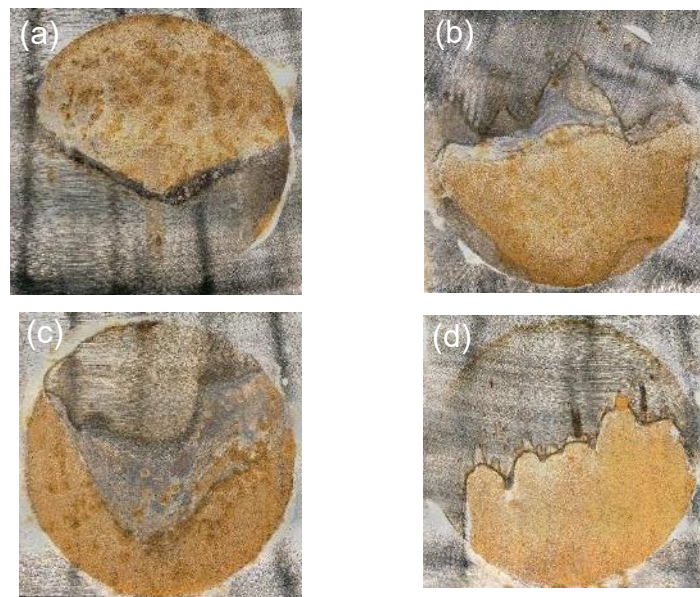
Figure 39 The evolution of the macro morphology of MC steel in NaCl solution with different temperatures: (a) 10 °C; (b) 15 °C; (c) 20 °C; (d) 25 °C
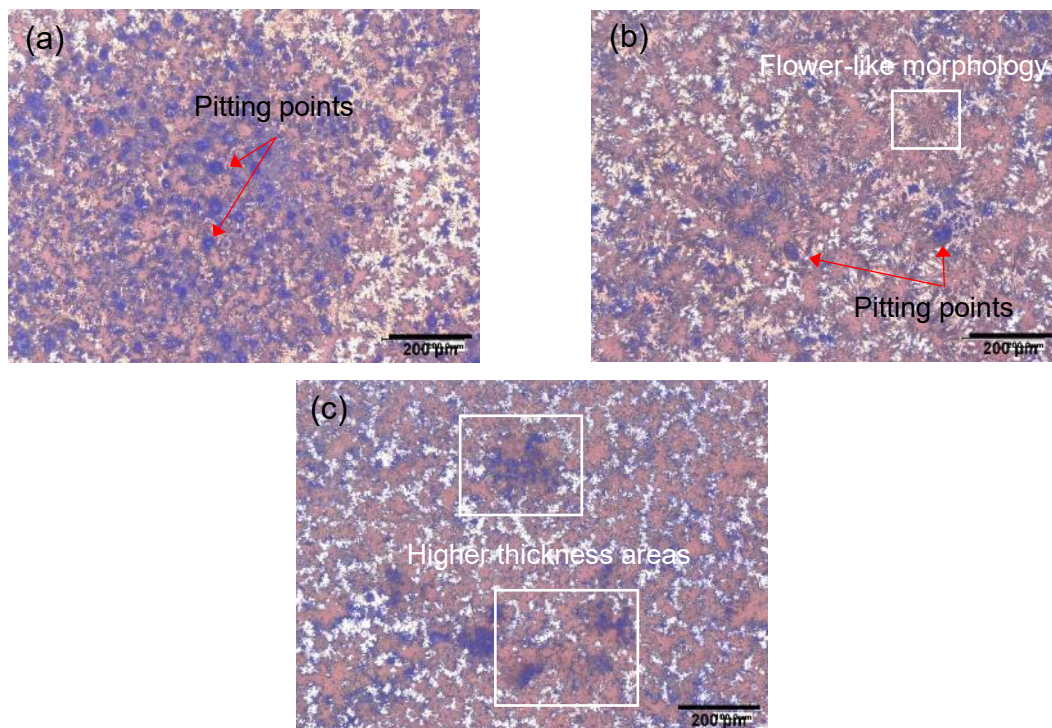

Figure 40 The morphology of rust layer of the sample at different temperatures: (a) 10 °C; (b) 15 °C; (c) 25 °C

When the solution temperature is 10 °C, due to the lower corrosion rate, fewer rusts are produced on the surface. These rusts are not enough to cover the pitting points, causing them to be exposed [as shown in Figure 40 (a) and Figure A. 8 (a)]. As the temperature

increases, more rusts are produced, which is enough to cover the pitting points. At the same time, the rust layer gradually shows a flower-like morphology [the white frame area in Figure 40 (b) and Figure A. 8 (b)], which was close to the sample immersed for one day under long-term corrosion conditions. When the temperature rises to 25°C, the pitting points are covered. The continuity of the rust layer is improved. At this temperature, the delamination of the corroded layer also becomes apparent. Meanwhile, the rust layer covering the pitting surface exhibits a relatively high thickness [the white frame area in Figure A. 8 (c)]. It shows the accumulation process of rusts on the top of the pits during the growth stage of pitting corrosion. It also echoes the speculation that the hillocks in the corrosion area are caused by pitting corrosion in the experiment of flow velocity [Figure 34 (a)].
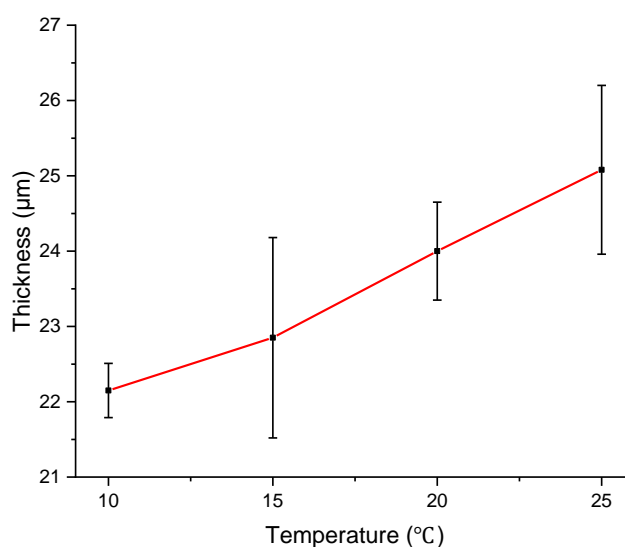

Figure 41 The thickness of the rust layer of MC steel in 3.5 wt.% NaCl solution at different temperature

Seven corrosion areas are randomly selected to measure the thickness of the rust layer on the sample surface. The average values are used to draw Figure 41. It is a trend graph of the thickness of the rust layer over temperature. The average results' errors (standard deviation) are less than 6%. As the temperature increases, the thickness of the layer increases. However, this gap is not very significant. Referring to the changing trend of rust layer thickness in long-term corrosion experiments, the rust layer is in the establishment stage for the samples at the early corrosion stage. The rusts produced by the corrosion process are used to establish a more coherent layer. The contribution to the thickness is small. A higher temperature increases the corrosion rate of the sample, resulting in more rusts to be produced. It can shorten the time required to establish the rust layer, laying the foundation for a rapid thickness growth later.

In summary, the temperature increases the corrosion rate in the early stage of corrosion mainly by increasing the system's energy and promoting the exchange of molecules near the surface. At high corrosion rates, more rusts are produced, resulting in a shorter time to form a more continuous rust layer. It may lead to the rapid growth of in thickness later.

6. Conclusion

Based on the findings in the current experiments, the following conclusions can be drawn:

- The corrosion process of MC steel in NaCl solution includes both pitting corrosion and uniform corrosion. It begins with a rapid initiation of pitting points due to the high proportion of grain boundaries in the microstructure. Some pitting points will grow horizontally due to the horizontal migration of anions (Cl^-, OH^-), which will develop into uniform corrosion to form a new plane. There are also initiation, passivation, and growth of new pitting points on this plane. Uniform corrosion and pitting corrosion are transformed into each other, which constitute the corrosion process of MC steel.

- The rust layer on the surface of the MC steel is layered, including a grey-black inner layer and an orange outer layer. After the establishment period, the thickness and compactness of the rust layer begin to increase. It brings specific protection to the matrix when it becomes dense enough to keep the corrosion rate at a relatively stable value.

- The AE signals in the accelerated corrosion process can be divided into two categories. One is related to uniform corrosion. The signals mainly concentrate on the corrosion initiation stage and have lower activity in the establishment stage. These may be related to the bubble burst caused by the continuous failure of the rust layer. The other is related to pitting corrosion. The signals have a strong signal in both the initiation and growth phases. It may be related to the evolution of hydrogen bubbles inside the pits, including bubble bursting and friction between the bubbles and the pit wall.

- Flow velocity increases the corrosion rate of MC steel, but this effect will not significantly after reaching a specific value. When the wave velocity is lower than 100 rpm, an increase in flow velocity results in the active oxygen transfer process, thus leading to an increase in corrosion rate. When the velocity is between 100-500 rpm, the controlled reaction of the corrosion transforms from a cathodic reaction to an anodic reaction. The rust layer can prevent the metal from contacting the Cl^- ions, resulting in less changes in the corrosion rate. However, in the detection range of the experiments, there is no area that the anodic reaction entirely controls the rate.

- Temperature can increase the corrosion rate in the initial stage of corrosion by increasing the system's energy and promoting the movement of Fe^{2+} and oxygen.

- Changes in flow velocity and temperature will not affect the stratification of the corrosion layer. Flow velocity can linearly increase the thickness of the corrosion layer. However, it will also bring a lot of pores and defects to the outer layer so that the protection ability of the corrosion layer no longer increases with the increase in thickness. Higher temperature leads to a rapid establishment of the rust layer, laying the foundation for rapid growth in the thickness later.

7. Recommendations

Based on the discussion and conclusions of the project, this section lists recommendations for future research work.

- Considering that the mooring system is affected by the combination of corrosion and mechanical damage such as fatigue in the marine environment, the study of a single corrosion process is of little significance to assess the remaining life of steel. This subject proves that the corrosion process of MC steel is a process of mutual transformation and coexistence of pitting corrosion and uniform corrosion. Pitting points are considered to become stress concentration points, which may initiate fatigue cracks. Therefore, fatigue tests can be introduced at different stages of pit development to investigate the characteristics of the areas prone to fatigue processes. It can also explore the influence of corrosion fatigue processes on the remaining life of steel.

- From the analysis related to the corrosion process of MC steel, it is clear that the S420MC HSLA steel selected in the experiments has a relatively severe corrosion process in the simulated seawater environment. The rust layer with protective ability grows slowly. Meanwhile, its protective ability is limited. If this steel is used in industrial structures, research on anti-corrosion measures is indispensable, such as adding surface coatings or applying the heat treatment to improve the metallographic structure.

- The active corrosion in the initial stage is attributed to the fine grains and large grain boundaries, whose junctions are prone to be the initiation points of pitting corrosion. However, the microscopic morphology observation of this process is not included in the experiment. Some advanced techniques can be introduced in subsequent experiments to study this phenomenon. For example, scanning electron microscopy can provide greater magnification for morphology observation and compositional determination. Electron backscatter diffraction techniques can be used to study the properties of grain boundaries.

- More parameters or more frequent morphology observations need to be included in analysing AE signals to distinguish the signal sources more accurately. The results of the AE part form an essential starting point for further analysis and investigations to reach a better understanding of the corrosion process in MC steel and its relation to acoustic activity.

- During the clustering of AE signals, a lower cross-correlation threshold is used. It may cause errors in signal clustering. More parameters need to be introduced to modify the accuracy of the clustering process, such as the mean and standard deviation of the signal amplitudes. It also makes the subsequent signal source determination more accurate.

- Wave simulations (flow velocity) that are closer to the actual speed and impact form need to be introduced to explore its influence on the corrosion process of MC steel.

- The effect of temperature on the corrosion of MC steel can be carried out over a more extended period. At the same time, considering the temperature changes in

the marine environment, it is possible to explore the effect of finer temperature changes in the corrosion process and corrosion fatigue process of MC steel.

- These experiments are carried out in a laboratory environment. Meanwhile, due to time limitations, the influence of microorganisms on the corrosion process is not considered. It is undeniable that microorganisms' types and growth stages have a significant influence on the corrosion process. At the same time, microorganisms and marine organisms (shellfish, etc.) tend to attach to the surface of the mooring chain and generate a biological layer. It will also affect the collection of AE signals. Therefore, the research on the influence of microorganisms is also a complex and interesting direction.

Acknowledgement

This master thesis project has been an exceptional studying experience in my lifetime. I would like to acknowledge the people who helped me with my graduation project.

First, I express sincere gratitude to my supervisors, Arjan Mol and Pooria Pahlavan, for their support and guidance on my experiments and the thesis report. I would like to thank Peyman Taheri, the defense committee member, for his valuable comments on the draft of the thesis report.

Secondly, I sincerely thank my daily supervisor Sarjoon Alkhatee for his continuous feedback and help with the project. I appreciate his advice and encouragement during this process and his persistence in this project.

Then I would also like to thank laboratory technician Agnieszka Kooijman-Banaszak for her practical tips and training. I am grateful to the members of the Corrosion team who have inspired me a lot during the experiments. At the same time, they have brought joy to my boring experimental life, especially during the COVID-19 pandemic. It keeps me from feeling lonely.

Also, I would like to thank my landlord Xiaoqing Li and her son, my baby roommate Yujie Wang. Xiaoqing has provided me with a comfortable and stable living environment. I no longer worry about my daily life during the postponed graduation period. Yujie makes my life more colorful. He taught me Dutch and shared the joy he got in preschool every day. It also gave me a better understanding of Dutch culture.

Finally, I sincerely thank my family for their understanding and support in my life and study. Their encouragement supported me to overcome various difficulties in the last six months and finally graduate successfully.

The master program at TU Delft is a precious experience for me. The friendliness, optimism and directness of the Dutch make me a wonderful experience. These advantages have also made a specific change in my personality. The two-and-a-half-year study abroad gives me a new perspective on future planning, which is an essential node in my life. It is a pleasure to have such a fantastic life experience.

Thank you all again! !
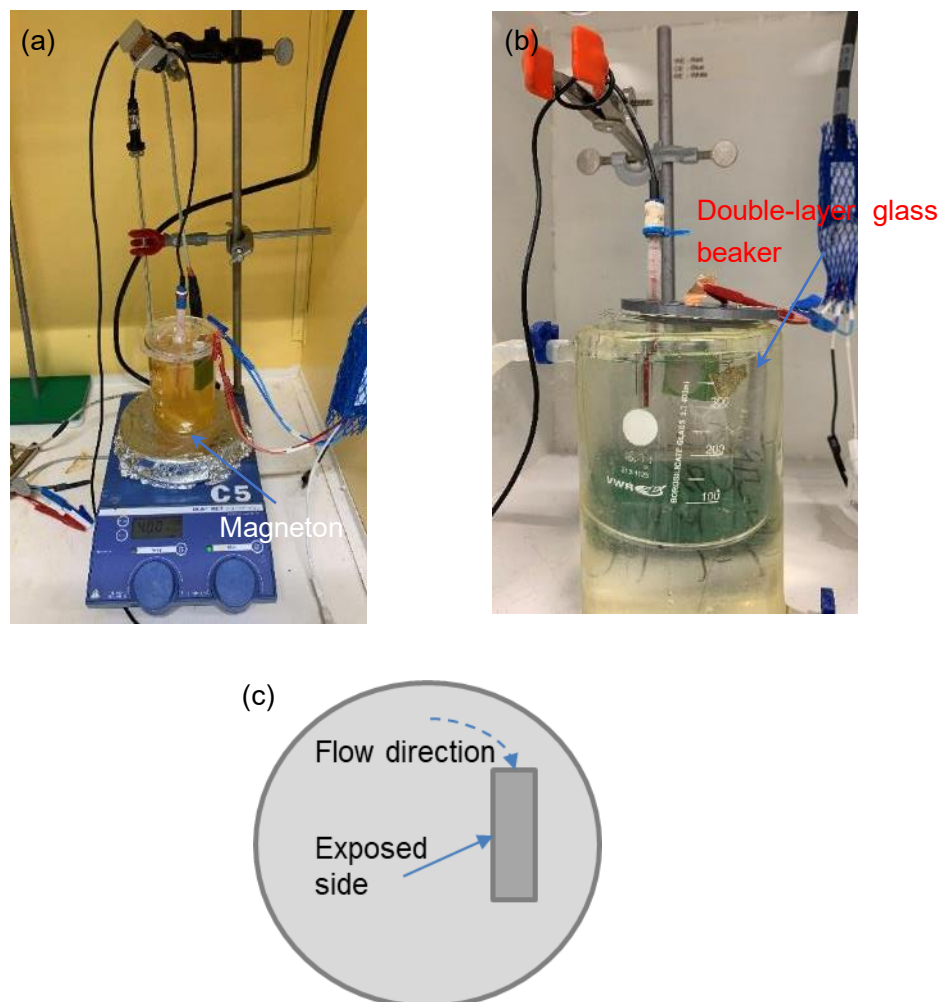
Appendix

A. 1 Setup of the experiments

Figure A. 1 Electrochemical detection setup in the experiments to study the influence of (a) flow velocity; (b) temperature; (c) Schematic diagram of sample placement in flow velocity experiments

In the experimental device related to the flow velocity [Figure A. 1 (a)], the connection method of the electrodes is consistent with the long-term immersion. However, the cover of the beaker supporting the sample is different from other experiments. The reference electrode is placed in the center. It will minimize the movement of the reference electrode in flowing water, thereby avoiding environmental errors.

A double-layer glass beaker is used in the experimental device related to the solution temperature [Figure A. 1 (b)]. This kind of beaker wall has a cavity inside that can contain liquid. Water with a specific temperature flows out from the thermostat, then comes into the cavity from the inlet at the bottom of the beaker. It flows from the bottom to the top and

back to the instrument from the outlet at the top, forming a cycle. A set of electrochemical detection device consistent with long-term immersion is put inside the double-layer beaker. The space between the two beakers is filled with distilled water. The water in the cavity further controls the temperature of the experimental solution in the beaker by adjusting the temperature of the distilled water in the double-layer beaker.
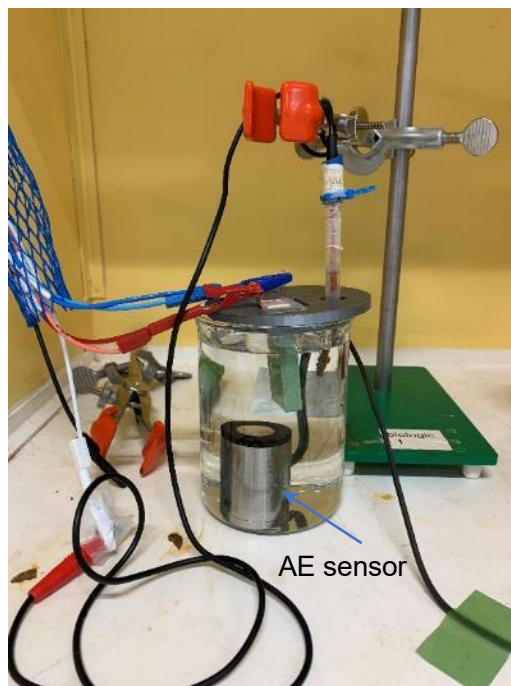

Figure A. 2 Setup in AE monitoring experiments

A. 2 Cross-correlation clustering method

This algorithm using signal cross-correlation as the clustering principle is developed by Van Steen et al. [102]. It can be used to characterize different AE signals during accelerated corrosion monitoring.

Clustering is the process of grouping a set of objects into clusters based on a virtual distance metric. In signal processing, cross-correlation can be used to measure the similarity of two waveforms as a function of the time lag applied to one of them. For continuous functions $f(t)$ and $g(t)$, the cross-correlation is defined as:

$$R_{fg}(t) = (f \blacksquare g)(t) = \int_{-\infty}^{+\infty} f(\tau)g(t+\tau)d\tau \qquad \text{Equation A. 1}$$

It is expressed as the function $g(t)$ sliding along the x-axis to calculate the product integration of each position. When the peaks (positive regions) or valleys (negative regions) are aligned, the contribution to the integration is significant. The normalized cross-correlation can be obtained by calculation:

$$\hat{R}_{fg}(t) = \frac{R_{fg}(t)}{\sqrt{R_{ff}(0)R_{gg}(0)}}$$

Equation A. 2

where

$$R_{ff}(0) = \int_{-\infty}^{+\infty} f(\tau)^2 d\tau$$

Equation A. 3

$$R_{gg}(0) = \int_{-\infty}^{+\infty} g(\tau)^2 d\tau$$

Equation A. 4

The value of $\hat{R}_{fg}(t)$ varies between -1 and 1. A value of 1 means that the two signals have the same shape, -1 means they have the same shape but opposite signs, and 0 means they are not similar.

A. 3 Height of morphology figure in color

In this section, the difference in the height of the sample's microstructure is indicated by different colors. In all the illustrations, dark blue indicates the location of the lowest point on the surface. The red color indicates the location of the highest point on the surface. When the color of a particular point is closer to dark blue, it indicates that the height difference between this point and the lowest point is slight. Conversely, the height difference is more remarkable if the color is closer to red. According to different surface conditions, the objects represented by dark blue and red are different. It will be explained in detail below each set of figures.
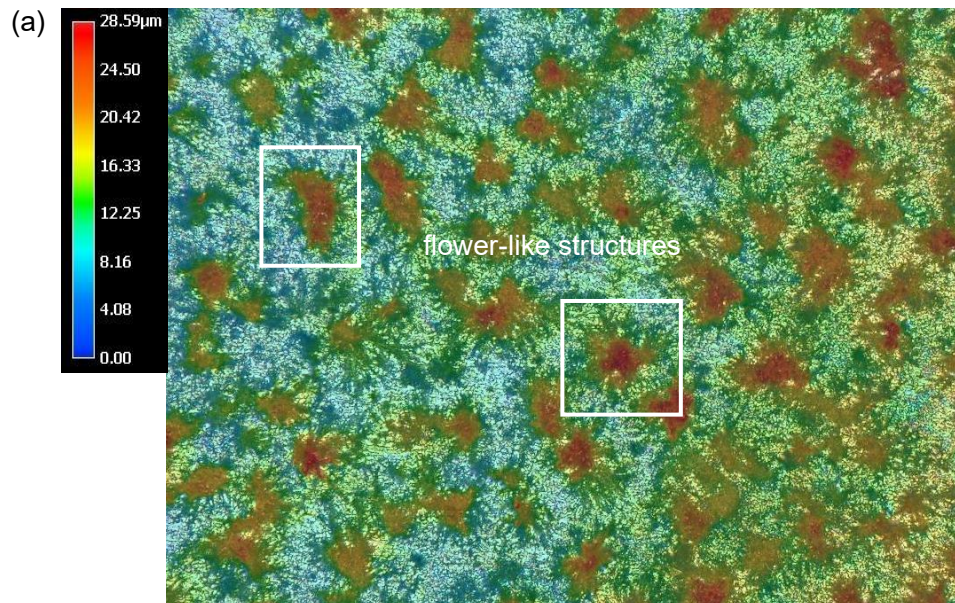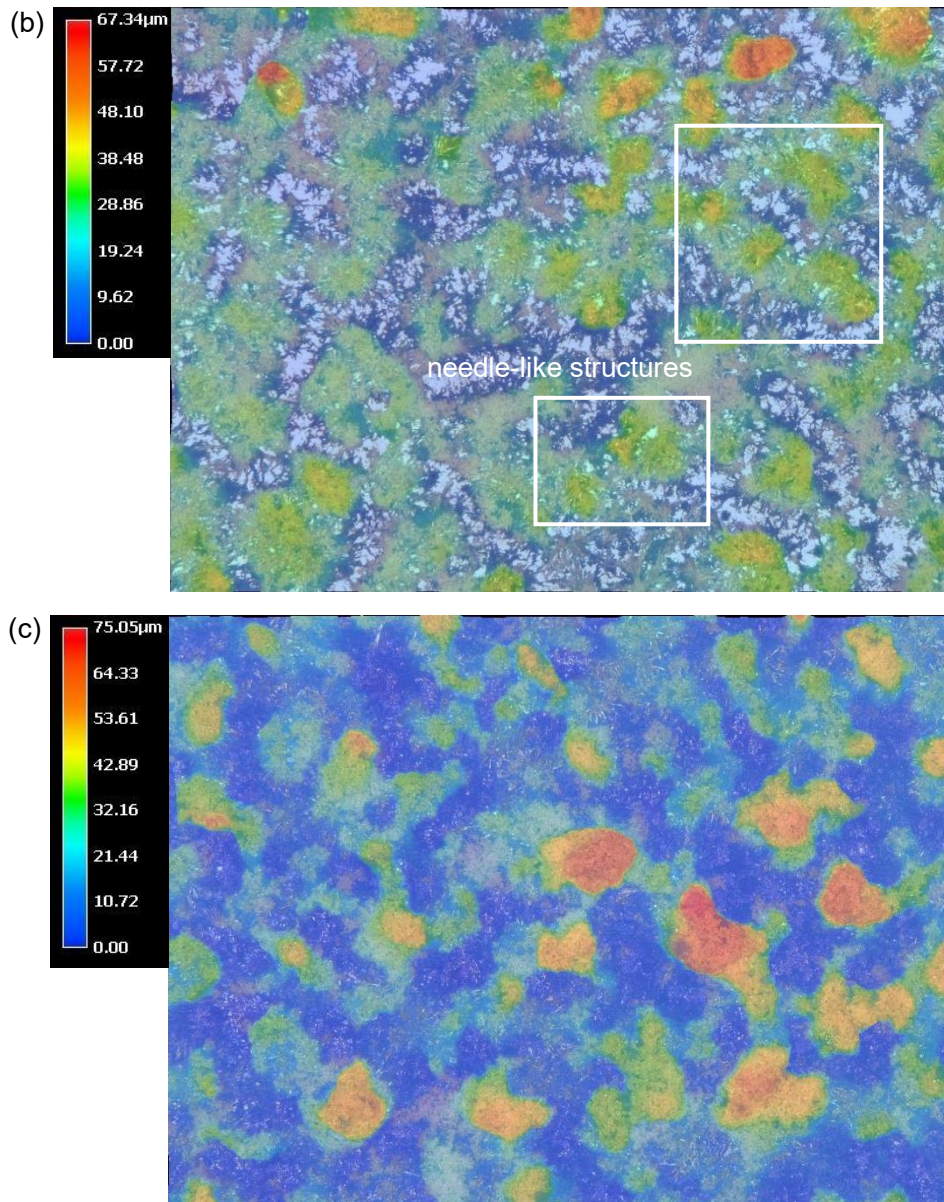
Figure A. 3 The heigh difference of morphology of rust layer immersed for (a) 1 day; (b) 4 days; (c) 7 days

Figure A. 3 shows the height difference of the rust layer on the surface of the sample in the long-term immersion experiments. In Figure A. 3 (a) and (b), dark blue represents the matrix of the sample. In figure (c), it represents the inner corrosion layer. The color difference is mainly reflected in the outer rust layer in these three figures. They have a certain thickness and are not coherently distributed. The area in the white box in the figure (a) and (b) corresponds to that in Figure 19, showing the (a) rust layer with flower-like structure and (b) area with the raised needle-like structure on top of the outer layer, respectively.
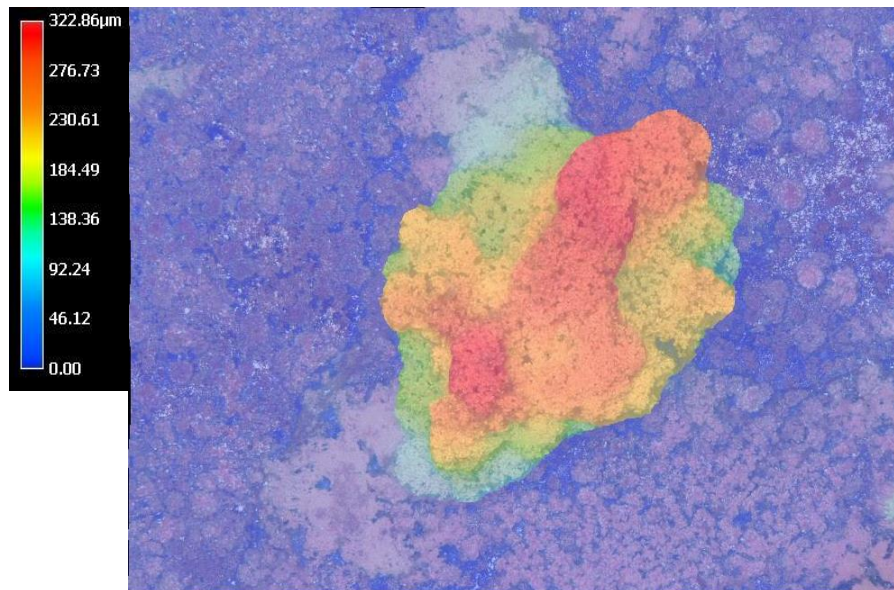
Figure A. 4 The heigh difference of microstructure of MC steel in NaCl solution without accelerating potential

In Figure A. 4, dark blue represents the sample matrix. The color change is mainly concentrated in the center bump. Different parts of it also show noticeable height differences. However, due to the large gap between the lowest and the highest point, the thinner corrosion layer exhibits the same color as the matrix. It only indicates that the thickness of the rust layer at other locations except for the central bump is less than 46 μm. They also have a certain thickness.
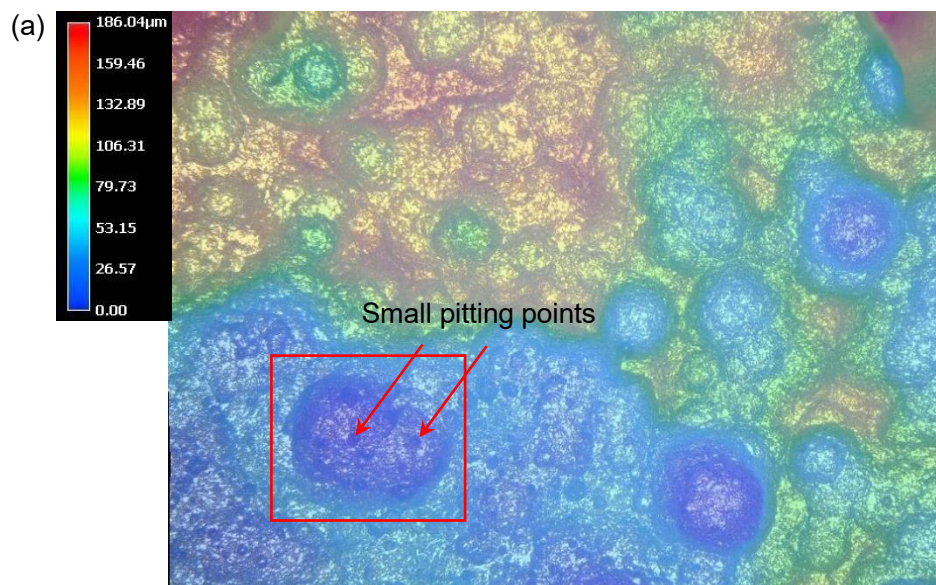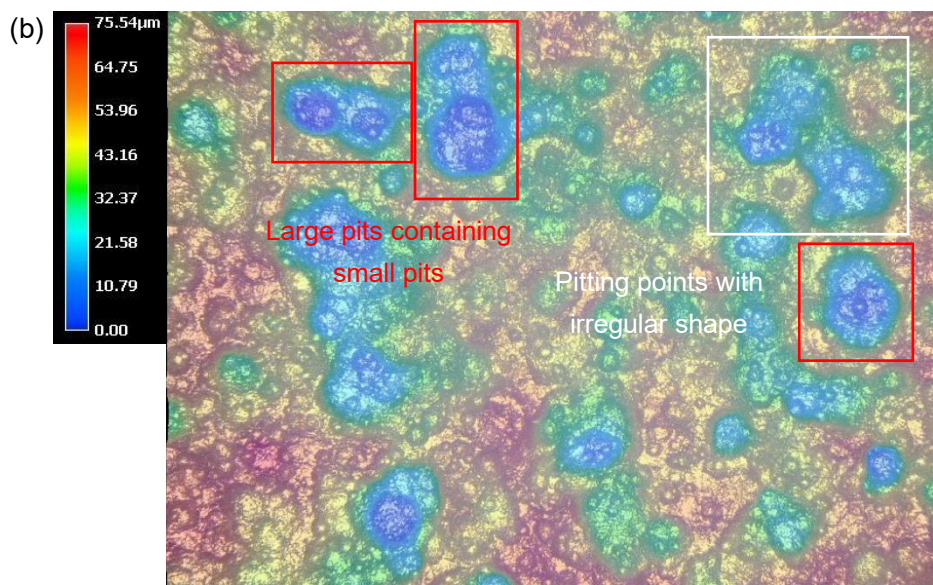
Figure A. 5 The heigh difference of microstructure of MC steel in NaCl solution (a) with accelerating potential (b) with OCP at ×200 magnification

In Figure A. 5, dark blue represents the bottom of the most severely corroded pit. Red represents the edge of the pit where the corrosion is least severe. Since the sample has been corroded for a week with potential applied, the base plane of the exposed area has been completely dissolved and does not exist in these two figures. The shape and relative depth of different corrosion areas can be clearly distinguished from these two figures. The intersection of the two colors represents the edges of different pits or planes. The red frame area in the figure represents the presence of new pitting points at the bottom of the larger pits. The area in the white frame shows the merging of several pits. They correspond to Figure 24 (c) and Figure 25 (b), respectively.
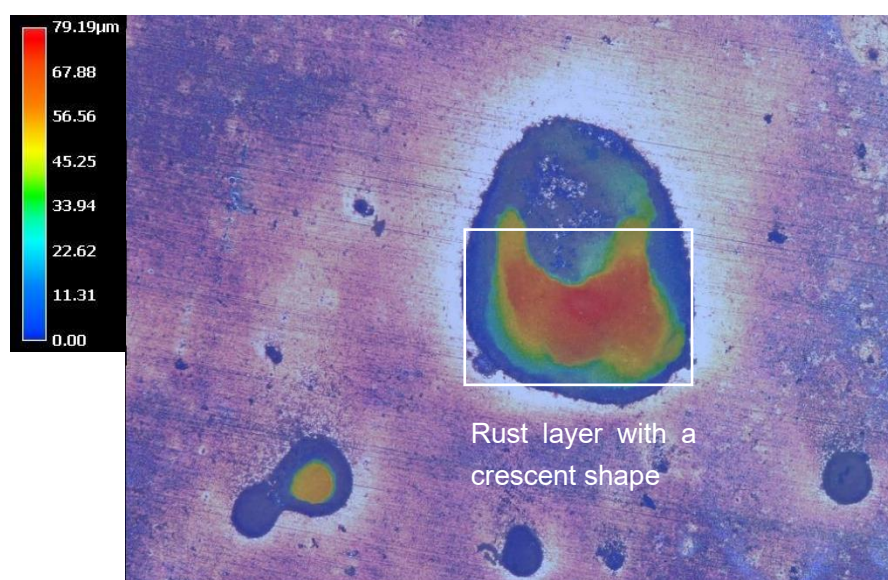
Figure A. 6 The heigh difference of microstructure of low-corrosion area of the sample with100 rpm flow velocity

In Figure A. 6, dark blue represents the sample matrix. The color change is mainly concentrated in two corroded areas. The red box shows where the rusts mainly accumulate in the larger corroded area, which corresponds to Figure 35 (c). It has a crescent shape.
In Figure A. 7 (a) and (b), dark blue represents the sample matrix. The color change mainly reflects the difference in the thickness of the rust layer. The red box shows the area where rusts accumulate abnormally, corresponding to Figure 34 (a) and (b), respectively. For Figure A. 7 (c), dark blue represents the lowest point in the rust layer. The color of the positions pointed by the red arrow is basically dark blue. The color suddenly changed to green or yellow on its two sides, indicating that the relative height has increased. Therefore, these two places are judged to be the cracks.
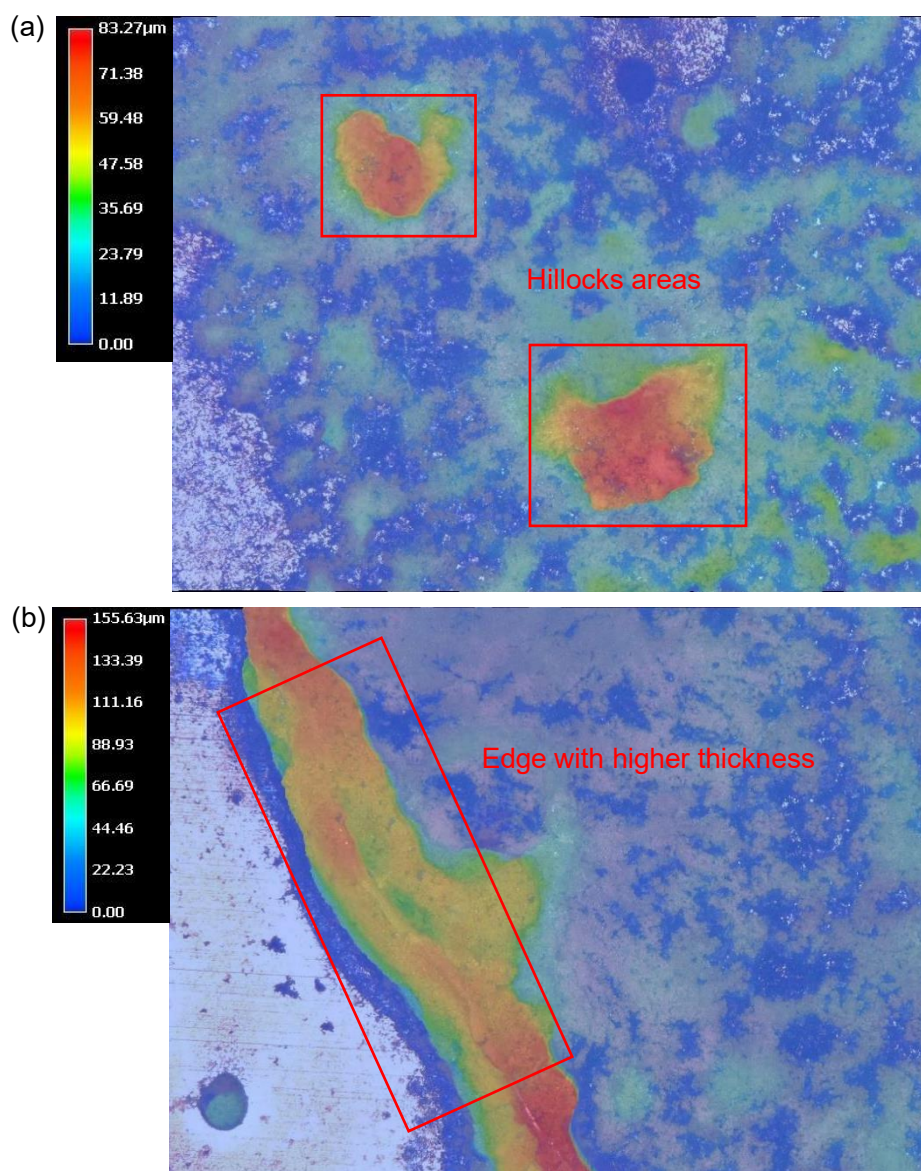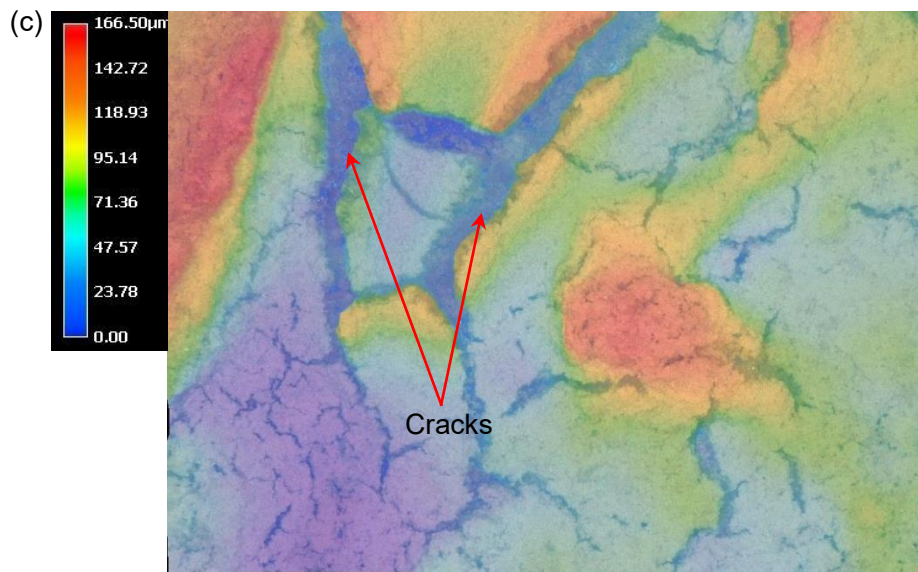
Figure A. 7 The heigh difference of the rust layer on the sample with (a) 50 rpm; (b) 100 rpm; (c) 500 rpm flow velocity
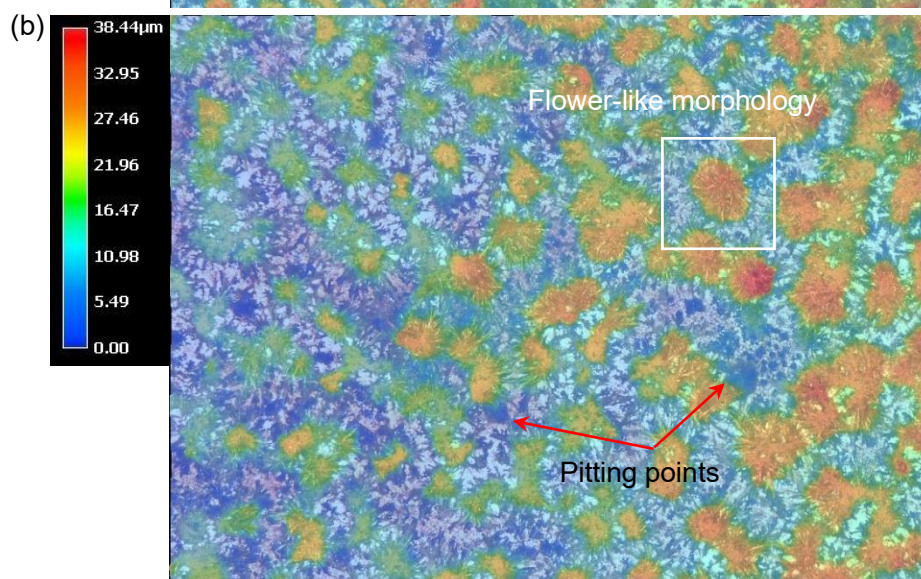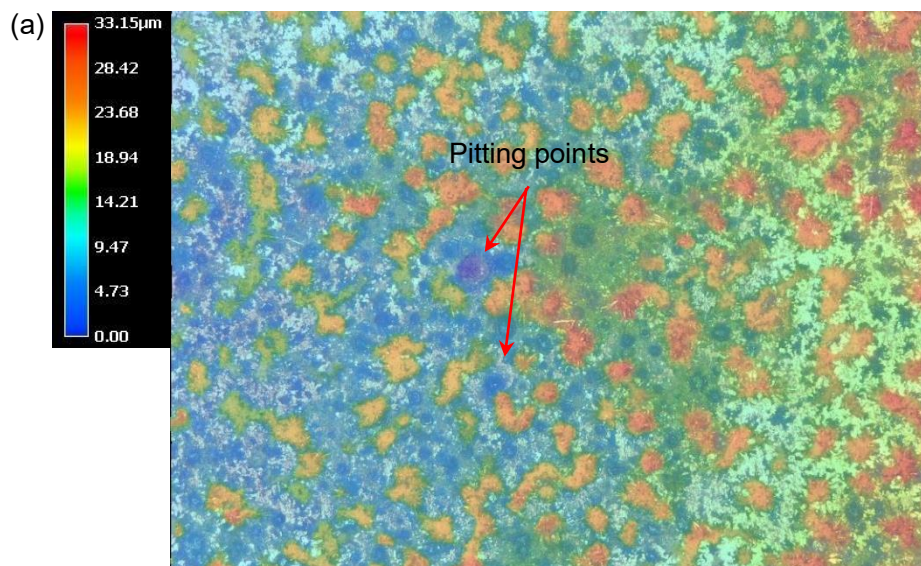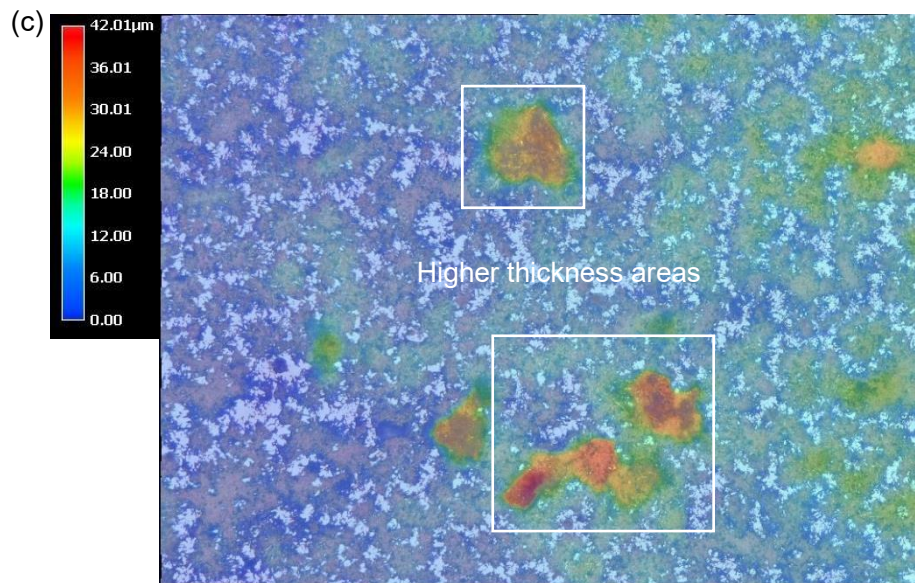
Figure A. 8 The heigh difference of the rust layer on the sample at different temperatures: (a) 10 °C; (b) 15 °C; (c) 25 °C

In Figure A. 8 (a) and (b), the dark blue represents the bottom of the pitting points, as indicated by the arrow. The color of the matrix is roughly cyan. The rusts accumulated on the surface show a change from yellow to orange. In Figure A. 8 (b), the white framed area shows a rust layer in the shape of a flower, which corresponds to Figure 40 (b). In Figure A. 8 (c), dark blue represents the sample matrix. The color change mainly reflects the difference in the thickness of the rust layer. The area in the white box shows a larger thickness, which is where rusts accumulated above the pitting points.

References

1.   Wu, X., et al., *Foundations of offshore wind turbines: A review.* Renewable and Sustainable Energy Reviews, 2019. **104**: p. 379-393.

2.   Xu, K., et al., *Design and comparative analysis of alternative mooring systems for floating wind turbines in shallow water with emphasis on ultimate limit state design.* Ocean Engineering, 2021. **219**: p. 108377.

3.   Barrera, C., R. Guanche, and I.J. Losada, *Experimental modelling of mooring systems for floating marine energy concepts.* Marine Structures, 2019. **63**: p. 153-180.

4.   Campanile, A., V. Piscopo, and A. Scamardella, *Mooring design and selection for floating offshore wind turbines on intermediate and deep water depths.* Ocean Engineering, 2018. **148**: p. 349-360.

5.   Gordon, R.B., M.G. Brown, and E.M. Allen. *Mooring integrity management: a state-of-the-art review*. in *Offshore Technology Conference*. 2014. Offshore Technology Conference.

6.   Ma, K.-t., et al. *A historical review on integrity issues of permanent mooring systems*. in *Offshore technology conference*. 2013. Offshore Technology Conference.

7.   Rivera, F.G., et al., *Acoustic emission technique to monitor crack growth in a mooring chain.* Applied Acoustics, 2018. **139**: p. 156-164.

8.   Angulo, Á., et al., *Acoustic emission monitoring of fatigue crack growth in mooring chains.* 2019. **9**(11): p. 2187.

9.   Angulo, A., et al., *Crack Initiation and Growth Acoustic Emission Analysis with Finite Element Analysis for Structural Health Monitoring of Mooring Chains.* 2017(shm).

10.   Xu, J., X. Wu, and E.-H.J.C.S. Han, *Acoustic emission during pitting corrosion of 304 stainless steel.* 2011. **53**(4): p. 1537-1546.

11.   *Hackeet, W. Mooring Chain and Assemblies*. 2020; Available from: https://www.williamhackett.co.uk/en-gb/products/chain_products/chain_assemblies/mooring_chain_and_assemblies/p-107156.

12.   AS, D.G. *Offshore mooring chain DNVGL-OS-E302*. 2015; Available from: http://www.dnvgl.com.

13.   Garcia, C., *High strength low alloyed (HSLA) steels*, in *Automotive Steels*. 2017, Elsevier. p. 145-167.

14.   Moravec, J., et al., *Heat Input Influence on the Fatigue Life of Welds from Steel S460MC.* Metals, 2020. **10**(10): p. 1288.

15.   Silvestre, E., et al., *Comparison of the hardening behaviour of different steel families: From mild and stainless steel to advanced high strength steels.* International journal of mechanical sciences, 2015. **101**: p. 10-20.

16.   Fernández, J., S. Illescas, and J. Guilemany, *Effect of microalloying elements on the austenitic grain growth in a low carbon HSLA steel.* Materials Letters, 2007. **61**(11-12): p. 2389-2392.

17.   Chen, Q. and S. Wang, *Design, Development and Application of Titanium Microalloyed Steel*, in *Titanium Microalloyed Steel: Fundamentals, Technology, and Products*. 2019,

Springer. p. 219-301.

18. Yuce, C., et al., *A case study: designing for sustainability and reliability in an automotive seat structure.* 2014. **6**(7): p. 4608-4631.

19. McCafferty, E., *Introduction to corrosion science*. 2010: Springer Science & Business Media.

20. Edwards, R. *AQUEOUS CORROSION OF STEEL*. 2013; Available from: http://corrosionengineeringsolutions.co.uk/.

21. Frankel, G. and N. Sridhar, *Understanding localized corrosion.* Materials today, 2008. **11**(10): p. 38-44.

22. Melchers, R., *Modeling of marine immersion corrosion for mild and low-alloy steels—Part 1: Phenomenological model.* Corrosion, 2003. **59**(4): p. 319-334.

23. Melchers, R.E., *Corrosion uncertainty modelling for steel structures.* Journal of Constructional Steel Research, 1999. **52**(1): p. 3-19.

24. Hayat, T., et al., *Theoretical investigation of Ree–Eyring nanofluid flow with entropy optimization and Arrhenius activation energy between two rotating disks.* Computer Methods and Programs in Biomedicine, 2019. **177**: p. 57-68.

25. Loto, R.T. and C.A. Loto, *Corrosion behaviour of S43035 ferritic stainless steel in hot sulphate/chloride solution.* Journal of Materials Research and Technology, 2018. **7**(3): p. 231-239.

26. Ijsseling, F., *General guidelines for corrosion testing of materials for marine applications: Literature review on sea water as test environment.* British Corrosion Journal, 1989. **24**(1): p. 53-78.

27. Chandler, K.A., *Marine and offshore corrosion*. Vol. 222. 1985: Elsevier.

28. GUEDES SCARES, C., et al., *Non-linear corrosion model for immersed steel plates accounting for environmental factors. Discussion.* Transactions-Society of Naval Architects and Marine Engineers, 2005. **113**: p. 306-329.

29. Cai, Y., et al., *A spatial-temporal approach for corrosion prediction in time-varying marine environment.* Journal of Loss Prevention in the Process Industries, 2020. **66**: p. 104161.

30. Zakowski, K., et al., *Influence of water salinity on corrosion risk—the case of the southern Baltic Sea coast.* Environmental monitoring and assessment, 2014. **186**(8): p. 4871-4879.

31. Frankignoulle, M., *A complete set of buffer factors for acid/base CO2 system in seawater.* Journal of Marine Systems, 1994. **5**(2): p. 111-118.

32. Guedes Soares, C., Y. Garbatov, and A. Zayed, *Effect of environmental factors on steel plate corrosion under marine immersion conditions.* Corrosion Engineering, Science and Technology, 2011. **46**(4): p. 524-541.

33. Caines, S., F. Khan, and J. Shirokoff, *Analysis of pitting corrosion on steel under insulation in marine environments.* Journal of Loss Prevention in the process Industries, 2013. **26**(6): p. 1466-1483.

34. Bhandari, J., et al., *Modelling of pitting corrosion in marine and offshore steel structures–A technical review.* Journal of Loss Prevention in the Process Industries, 2015. **37**: p. 39-62.

35. Yang, Z., et al., *Pitting initiation and propagation of x70 pipeline steel exposed to*

chloride-containing environments. Materials, 2017. **10**(9): p. 1076.

36. Ida, N., et al. *The Role of Pitting at Mns Inclusions in Intergranular Corrosion of Sensitized Type 304 Stainless Steel in NaCl Solution.* in *ECS Meeting Abstracts.* 2018. IOP Publishing.

37. Melchers, R.E., I.A. Chaves, and R. Jeffrey, *A conceptual model for the interaction between carbon content and manganese sulphide inclusions in the short-term seawater corrosion of low carbon steel.* Metals, 2016. **6**(6): p. 132.

38. Liu, C., et al., *Role of Al2O3 inclusions on the localized corrosion of Q460NH weathering steel in marine environment.* Corrosion Science, 2018. **138**: p. 96-104.

39. Liu, C., et al., *Synergistic effect of Al2O3 inclusion and pearlite on the localized corrosion evolution process of carbon steel in marine environment.* Materials, 2018. **11**(11): p. 2277.

40. Wei, W.-z., et al., *Initiation and propagation of localized corrosion induced by (Zr, Ti, Al)-O x inclusions in low-alloy steels in marine environment.* Journal of Iron and Steel Research International, 2020: p. 1-11.

41. Ramezanzadeh, M., G. Bahlakeh, and B. Ramezanzadeh, *Study of the synergistic effect of Mangifera indica leaves extract and zinc ions on the mild steel corrosion inhibition in simulated seawater: Computational and electrochemical studies.* Journal of Molecular Liquids, 2019. **292**: p. 111387.

42. Ramezanzadeh, M., et al., *Mild steel surface eco-friendly treatment by Neodymium-based nanofilm for fusion bonded epoxy coating anti-corrosion/adhesion properties enhancement in simulated seawater.* Journal of Industrial and Engineering Chemistry, 2019. **72**: p. 474-490.

43. Riazaty, P., R. Naderi, and B. Ramezanzadeh, *Synergistic corrosion inhibition effects of benzimidazole-samarium (III) molecules on the steel corrosion prevention in simulated seawater.* Journal of Molecular Liquids, 2019. **296**: p. 111801.

44. Wika, S.F., *Pitting and crevice corrosion of stainless steel under offshore conditions.* 2012, Institutt for materialteknologi.

45. Ma, F.-Y.J.P.c., *Corrosive effects of chlorides on metals.* 2012. **294**: p. 139-78.

46. Akpanyung, K. and R. Loto. *Pitting corrosion evaluation: a review.* in *Journal of Physics: Conference Series.* 2019. IOP Publishing.

47. Fujii, T., et al., *Crystallographic Evaluation of Susceptibility to Intergranular Corrosion in Austenitic Stainless Steel with Various Degrees of Sensitization.* 2020. **13**(3): p. 613.

48. Guo, Y.-b., et al., *Effect of microstructure variation on the corrosion behavior of high-strength low-alloy steel in 3.5 wt% NaCl solution.* International Journal of Minerals, Metallurgy, and Materials, 2015. **22**(6): p. 604-612.

49. Pedeferri, P., P.J.C.S. Pedeferri, and Engineering, *Intergranular and Selective Corrosion.* 2018: p. 297-311.

50. Hu, S., E.-H. Han, and X. Liu, *Atomic-scale evidence for the intergranular corrosion mechanism induced by co-segregation of low-chromium ferritic stainless steel.* Corrosion Science, 2021. **189**: p. 109588.

51. Wang, P.-j., et al., *Influence of grain refinement on the corrosion behavior of metallic materials: A review.* 2021. **28**(7): p. 1112-1126.

52. Liu, Z.Y., X.G. Li, and Y.F. Cheng, *In-situ characterization of the electrochemistry of*

grain and grain boundary of an X70 steel in a near-neutral pH solution. Electrochemistry Communications, 2010. **12**(7): p. 936-938.

53. Kim, H. and W.J.C.S. Kim, *Enhanced corrosion resistance of ultrafine-grained AZ61 alloy containing very fine particles of Mg17Al12 phase.* 2013. **75**: p. 228-238.

54. Huo, W., et al., *Simultaneously enhanced strength and corrosion resistance of Mg–3Al–1Zn alloy sheets with nano-grained surface layer produced by sliding friction treatment.* 2017. **720**: p. 324-331.

55. Pu, Z., et al., *Grain refined and basal textured surface produced by burnishing for improved corrosion performance of AZ31B Mg alloy.* 2012. **57**: p. 192-201.

56. Liu, L., et al., *Electrochemical corrosion behavior of nanocrystalline materials—a review.* 2010. **26**(1): p. 1-14.

57. Kim, J.-K., et al., *Corrosion monitoring of reinforced steel embedded in cement mortar under wet-and-dry cycles by electrochemical impedance spectroscopy.* Sensors, 2020. **20**(1): p. 199.

58. Popov, B.N., *Chapter 5 - Basics of Corrosion Measurements*, in *Corrosion Engineering*, B.N. Popov, Editor. 2015, Elsevier: Amsterdam. p. 181-237.

59. Yoo, S.R., et al., *Open Circuit Potential Changes upon Protonation/Deprotonation of ω-Functionalized Alkanethiols on Au: Determination of Surface pK _1_/_2 in Aqueous and Non-Aqueous System.* Bulletin of the Korean Chemical Society, 2016. **37**(9): p. 1537-1540.

60. Wang, R., et al., *Electrochemical corrosion performance of Cr and Al alloy steels using a J55 carbon steel as base alloy.* Corrosion science, 2014. **85**: p. 270-279.

61. Venkatesan, P., N. Palaniswamy, and K. Rajagopal, *Corrosion performance of coated reinforcing bars embedded in concrete and exposed to natural marine environment.* Progress in Organic Coatings, 2006. **56**(1): p. 8-12.

62. Wang, Y., et al., *Effect of Bacillus subtilis on corrosion behavior of 10MnNiCrCu steel in marine environment.* Scientific reports, 2020. **10**(1): p. 1-9.

63. Cheng, S., et al., *Microbially influenced corrosion of stainless steel by marine bacterium Vibrio natriegens:(I) Corrosion behavior.* Materials Science and Engineering: C, 2009. **29**(3): p. 751-755.

64. de Messano, L.V., et al., *The effect of biofouling on localized corrosion of the stainless steels N08904 and UNS S32760.* International Biodeterioration & Biodegradation, 2009. **63**(5): p. 607-614.

65. Enos, D.G. and L. Scribner, *The Potentiodynamic Polarization Scan–Technical Report 33.* Solartron Instruments, 1997.

66. McCluney, S., et al., *Comparing electrochemical impedance spectroscopy methods for estimating the degree of delamination of organic coatings on steel.* 1992. **139**(6): p. 1556.

67. Shahid, K.A., et al., *Assessment of corroded reinforced concrete beams: Cyclic load test and acoustic emission techniques.* Construction and Building Materials, 2020. **233**: p. 117291.

68. Noorsuhada, M., *An overview on fatigue damage assessment of reinforced concrete structures with the aid of acoustic emission technique.* Construction and Building Materials, 2016. **112**: p. 424-439.

69.   Kawasaki, Y., T. Fukuyama, and T. Okamoto, *Acoustic emission method and electrochemical noise technique for evaluation of rebar corrosion in reinforced concrete*, in *Acoustic Emission and Related Non-Destructive Evaluation Techniques in the Fracture Mechanics of Concrete*. 2021, Elsevier. p. 65-79.

70.   Skal'Kyi, V., et al., *Acoustic-emission diagnostics of corrosion defects in materials (a survey). Part. 1. Detection of electrochemical corrosion and corrosion fatigue.* Materials Science, 2017. **53**(3): p. 295-305.

71.   Wu, K. and J.-W. Byeon, *Morphological estimation of pitting corrosion on vertically positioned 304 stainless steel using acoustic-emission duration parameter.* Corrosion Science, 2019. **148**: p. 331-337.

72.   Wu, Y., et al., *Acoustic emission behaviour during the evolution of a single pit on stainless steels.* Corrosion Science, 2021. **183**: p. 109308.

73.   Fregonese, M., et al., *Initiation and propagation steps in pitting corrosion of austenitic stainless steels: monitoring by acoustic emission.* Corrosion science, 2001. **43**(4): p. 627-641.

74.   Shiwa, M., et al., *In-situ observation and acoustic emission analysis for corrosion pitting of mgcl2 droplet in sus304 stainless steel.* 2012: p. M2011399.

75.   Jirarungsatian, C. and A. Prateepasen, *Pitting and uniform corrosion source recognition using acoustic emission parameters.* Corrosion Science, 2010. **52**(1): p. 187-197.

76.   Xu, J., X. Wu, and E.-H.J.C.s. Han, *Acoustic emission during the electrochemical corrosion of 304 stainless steel in H2SO4 solutions.* 2011. **53**(1): p. 448-457.

77.   Jaubert, L., et al., *On the opportunity to use non-intrusive acoustic emission recordings for monitoring uniform corrosion of carbon steel and austenitic stainless steel in acid and neutral solutions.* 2005. **47**(8): p. 465-471.

78.   Jomdecha, C., A. Prateepasen, and P. Kaewtrakulpong, *Study on source location using an acoustic emission system for various corrosion types.* NDT & E International, 2007. **40**(8): p. 584-593.

79.   Fregonese, M., et al., *Monitoring pitting corrosion of AISI 316L austenitic stainless steel by acoustic emission technique: choice of representative acoustic parameters.* 2001. **36**(3): p. 557-563.

80.   Prateepasen, A., C. Jirarungsatean, and P. Tuengsook. *Identification of AE source in corrosion process*. in *Key Engineering Materials*. 2006. Trans Tech Publ.

81.   Tang, J., et al., *In-situ monitoring and analysis of the pitting corrosion of carbon steel by acoustic emission.* 2019. **9**(4): p. 706.

82.   Kim, H.-Y., et al., *Evaluation of pitting corrosion mechanism of AZ31 magnesium alloy by monitoring acoustic emission.* 2017. **58**(1): p. 123-126.

83.   Kietov, V., M. Mandel, and L. Krüger, *Combination of electrochemical noise and acoustic emission for analysis of the pitting corrosion behavior of an austenitic stainless cast steel.* Advanced Engineering Materials, 2019. **21**(5): p. 1800682.

84.   Perez, N., *Kinetics of activation polarization*, in *Electrochemistry and corrosion science*. 2016, Springer. p. 101-150.

85.   McCafferty, E., *Kinetics of corrosion*, in *Introduction to Corrosion Science*. 2010, Springer. p. 119-175.

86.   Simmons, E.J.C., *Use of the Pearson bridge in corrosion inhibitor evaluation.* 1955. **11**(6): p. 25-30.

87.   Greene, N. and G.J.C. Saltzman, *Effect of plastic deformation on the corrosion of iron and steel.* 1964. **20**(9): p. 293t-298t.

88.   Salhi, A., et al., *Keto-enol heterocycles as new compounds of corrosion inhibitors for carbon steel in 1M HCl: Weight loss, electrochemical and quantum chemical investigation.* Journal of Molecular Liquids, 2017. **248**: p. 340-349.

89.   Streiner, D.L.J.T.C.j.o.p., *Maintaining standards: differences between the standard deviation and standard error, and when to use each.* 1996. **41**(8): p. 498-502.

90.   Zong, Y. and C.-M. Liu, *Microstructure, Mechanical Properties, and Corrosion Behavior of Ultra-Low Carbon Bainite Steel with Different Niobium Content.* Materials, 2021. **14**(2): p. 311.

91.   Rajakaruna, R. and I. Ariyarathna, *Functionalized metal-based nanoelectrocatalysts for water splitting*, in *Handbook of Functionalized Nanomaterials for Industrial Applications*. 2020, Elsevier. p. 83-109.

92.   Wang, K., et al., *Effects of welding heat input on microstructure and electrochemical behavior of flux-cored arc-welded Q690 HSLA steel.* Advances in Materials Science and Engineering, 2018. **2018**.

93.   Liu, W., et al., *Corrosion behavior of the steel used as a huge storage tank in seawater.* Journal of Solid State Electrochemistry, 2010. **14**(6): p. 965-973.

94.   Noureddine, M. and O. Allaoui, *Effect of tempering on mechanical proprieties and corrosion behavior of X70 HSLA steel weldments.* The International Journal of Advanced Manufacturing Technology, 2020. **106**(7): p. 2689-2701.

95.   Zhang, H., et al., *Investigation on stress corrosion cracking behavior of welded high strength low alloy steel in seawater containing various dissolved oxygen concentrations.* International Journal of Electrochemical Science, 2013. **8**: p. 1262-1273.

96.   Mardare, L. and L. Benea. *Marine corrosion behavior of EH 36 steel in the Black Sea*. in *IOP Conference Series: Materials Science and Engineering*. 2019. IOP Publishing.

97.   Diaz, I., et al., *Atmospheric corrosion of Ni-advanced weathering steels in marine atmospheres of moderate salinity.* Corrosion Science, 2013. **76**: p. 348-360.

98.   Cano, H., et al., *Characterization of corrosion products formed on Ni 2.4 wt%–Cu 0.5 wt%–Cr 0.5 wt% weathering steel exposed in marine atmospheres.* Corrosion Science, 2014. **87**: p. 438-451.

99.   De la Fuente, D., et al., *Long-term atmospheric corrosion of mild steel.* Corrosion Science, 2011. **53**(2): p. 604-617.

100.   Refait, P., et al., *Electrochemical formation and transformation of corrosion products on carbon steel under cathodic protection in seawater.* Corrosion Science, 2013. **71**: p. 32-36.

101.   Wang, Y., X. Zuo, and J. Li, *Corrosion resistance of the welded joint of submarine pipeline steel with ferrite plus bainite dual-phase microstructure.* steel research international, 2015. **86**(11): p. 1260-1270.

102.   Van Steen, C., et al., *Localisation and characterisation of corrosion damage in reinforced concrete by means of acoustic emission and X-ray computed tomography.* Construction and Building Materials, 2019. **197**: p. 21-29.

103. Yang, Y., et al., *New understanding of the effect of hydrostatic pressure on the corrosion of Ni–Cr–Mo–V high strength steel.* Corrosion Science, 2013. **73**: p. 250-261.

104. Wang, Y., G. Cheng, and Y. Li, *Observation of the pitting corrosion and uniform corrosion for X80 steel in 3.5 wt.% NaCl solutions using in-situ and 3-D measuring microscope.* Corrosion Science, 2016. **111**: p. 508-517.

105. Jiang, S., et al., *Influence of chromium on the flow-accelerated corrosion behavior of low alloy steels in 3.5% NaCl solution.* Corrosion Science, 2017. **123**: p. 217-227.

106. Zheng, Z.B. and Y.G. Zheng, *Erosion-enhanced corrosion of stainless steel and carbon steel measured electrochemically under liquid and slurry impingement.* Corrosion Science, 2016. **102**: p. 259-268.

107. Li, L.L., Z.B. Wang, and Y.G. Zheng, *Interaction between pitting corrosion and critical flow velocity for erosion-corrosion of 304 stainless steel under jet slurry impingement.* Corrosion Science, 2019. **158**: p. 108084.

108. Choe, S.-B. and S.-J. Lee, *Effect of flow rate on electrochemical characteristics of marine material under seawater environment.* Ocean Engineering, 2017. **141**: p. 18-24.

109. Melchers, R., *Mathematical modeling of the effect of water velocity on the marine immersion corrosion of mild steel coupons.* Corrosion, 2004. **60**(5): p. 471-478.

110. Li, Z., et al., *The influence of critical flow velocity on corrosion of stainless steel.* 2017. **17**(6): p. 1234-1240.

111. Wharton, J.A. and R.J.K. Wood, *Influence of flow conditions on the corrosion of AISI 304L stainless steel.* Wear, 2004. **256**(5): p. 525-536.

112. Cook, D.C., *Spectroscopic identification of protective and non-protective corrosion coatings on steel structures in marine environments.* Corrosion Science, 2005. **47**(10): p. 2550-2570.

113. Yan, Q., et al., *Effect of temperature on corrosion behavior of E690 steel in 3.5 wt.% NaCl solution.* 2021. **8**(1): p. 016528.